RHEOLOGICAL PROPERTIES, EMPLACEMENT VELOCITIES,

AND GRAIN SIZE ANALYSIS OF THE 1986 PYROCLASTIC FLOWS

AT MT. ST. AUGUSTINE, ALASKA

by

Anthony James Limke

RECOMMENDED:

James E. Begét, Chairman, Advisory Committee

Jürgen Kienle

David M. Hopkins

Samuel E. Swanson, Head, Department of Geology and Geophysics

APPROVED:

Paul B. Reichardt, Dean, College of Natural Sciences

Luis Proenza, Dean of the Graduate School

8/1/91

Date

# RHEOLOGICAL PROPERTIES, EMPLACEMENT VELOCITIES, AND GRAIN SIZE ANALYSIS OF THE 1986 PYROCLASTIC FLOWS AT MT. ST. AUGUSTINE, ALASKA

A
THESIS

Presented to the Faculty of the University of Alaska
in Partial Fulfillment of the Requirements
for the Degree of

MASTER OF SCIENCE

by
Anthony James Limke, B.S.

Fairbanks, Alaska
September 1991

## ABSTRACT

Pyroclastic block and ash flow units from the 1986 eruptions of Mt. St. Augustine exhibit fine-grained basal ash and lapilli layers beneath poorly sorted, massive layers of blocks, lapilli, and ash. Morphological features of the block and ash flow units include levees, channels, and lobate termini. These observations are consistent with Bingham rheology characterized by viscous flow and plastic strength. Block and ash flow yield strength, calculated from field data, was found to decrease significantly with increasing distance from the source. This phenomenon is related to the significantly decreasing mean grain size determined from a granulometric study of the deposits. The field-derived rheological parameters were incorporated into three simple mathematical models which estimate flow velocity. Results of the modeling exercises are shown to compare favorably with a well-constrained data set of pumice flow velocities from Mt. St. Helens.

## TABLE OF CONTENTS

## LIST OF FIGURES

## LIST OF TABLES

## ACKNOWLEDGEMENTS

I gratefully acknowledge the efforts and guidance of my graduate advisory committee: Dr. J. E. Begét for his inspiration, assistance, and enthusiasm for this research; Dr. J. Kienle for his lively discussions and depth of experience at Mt. St. Augustine; and Dr. D. M. Hopkins for his steadfast support and thorough review of the thesis.

Heartfelt thanks go to J. E. Lindstrom, L. G. Kodosky, M. R. Brockman, S. J. Lutsch, and E. M. Dupuis-Nouillé for the unforgettable experiences that only close friends can provide.

Special thanks to N. V. Fitton for critical readings and exemplary typesetting assistance.

This thesis is dedicated to my parents, Dr. Louis H. and Genevieve T. Limke, without whose unflagging love, understanding, and patience this task would have been impossible.

## CHAPTER 1:

## INTRODUCTION

The 1986 eruptions at Mt. St. Augustine generated numerous small pyroclastic flows which deposited primarily on the north side of the island volcano. Field studies implemented in 1986 and 1987 were designed to collect data for the characterization of active pyroclastic flow rheological, kinematic, and sedimentological properties. Rheological analyses employed in this work were originally developed for liquid-mediated debris flows. Analogous fluid-like behavior is assumed for the application of these analyses to pyroclastic flow deposition. Simple computer models incorporating field-derived rheological properties were run in an attempt to retrodict the emplacement velocities of the studied pyroclastic flows. Sedimentological characterization of widely-dispersed individual pyroclastic flow deposits was carried out via grain-size analyses encompassing the complete range of particle sizes observed in the field.

Pyroclastic flows are hot mixtures of volcanic gases, ingested air, ash, lapilli, and blocks of pumice and/or juvenile lithic material. They are produced in several ways, including: 1) the collapse of a vertically ejected eruption column (Smith 1960; Sparks et al. 1978); 2) low-level "boiling over" or fountaining of ejecta from the vent rim (Moore and Nelson 1969; Nairn and Self 1978); 3) magmatically pressurized lateral ejection (Sheridan 1980); and 4) the collapse of a growing lava dome (Davies et al. 1978; Rose 1973). Pyroclastic flows are extremely mobile: they travel at high velocities for long distances and therefore have great destructive potential.

The detailed mechanics of pyroclastic flow emplacement are poorly understood for several reasons. Pyroclastic flows are very dangerous to approach, and few close observations

have been made of their behavior. In addition, the flow processes are very complex. Pyroclastic flows may be considered to be the most general case of grain flow wherein collisions between particles having a wide size distribution are responsible for momentum transfer in the flow. Such collisions act to resist the motion of the bulk material when the flow is moving at high velocities, and at low velocities, the collisions act to transmit momentum forward throughout the finite length of the moving flow. Pyroclastic flows are partially fluidized by air ingestion at the flow head, magmatic gases exsolved by juvenile material, and collisions between clasts. Hence, the flows are able to maintain motion even on low slopes, and as the volume of flow is increased (with a proportional increase in momentum), its mobility and runout distance also become greater (Hsü 1975, 1978).

### 1.1 Relevant Previous Studies.

Numerous theories and models exist for explaining the mechanisms of flowing granular solids. Bagnold (1954) demonstrated the presence of a dispersive pressure, which keeps the individual grains aloft, acting normally from the bed of rapidly shearing cohesionless solids. Lowe (1976) derived expressions for the steady uniform gravity flow of cohesionless solids maintained in a dispersed state by Bagnoldian dispersive pressure. The interstitial fluid in such grain flows is the same as the ambient fluid through which the flow is moving. The above experimental studies employed single-diameter spheres, and may be considered applicable only as a first approximation to the behavior of poorly sorted pyroclastic material. Erismann (1979) proposed a self-lubrication model to explain the "more or less undisturbed sequential order" observed in the moving components of many large landslides. His equations suggest that the energy loss is minimal except for frictional effects at the gliding base of flow. Cannon and Savage (1988) developed a model based on the principle of conservation of momentum which can account for the changing mass of a debris flow over the distance it travels.

By applying principles of rheology, fluid mechanics, and open-channel hydraulics to their studies of debris flows, Johnson (1970, 1984) and Johnson and Rodine (1984) derived expressions for estimating yield strength, Bingham viscosity, and mean velocity of debris flows from deposit morphometry. Johnson's analyses have seen wide use in studies of rockfall avalanches (Eppler et al. 1987), volcanogenic debris avalanches and mudflows (Fink et al. 1981; Voight et al. 1983), debris flows (Gallino and Pierson 1985; Jones et al. 1984), and pyroclastic flows (Davies et al. 1978; Wilson and Head 1981; Freundt and Schmincke 1986; Limke and Begét 1986). These studies are testimony to the fluid-like behavior of active sediment gravity flows.

Pyroclastic flows behave similarly to other types of high-concentration sediment gravity flows such as water-mediated mudflows and debris flows; cold, dry rockfall avalanches; and volcanogenic debris avalanches. All of these types of flows can be extremely destructive and mobile, and their deposits often display well developed levee-channel-terminal lobe morphology. Sediment gravity flows are driven by gravitational and inertial energy, and they are slowed by the effects of internal and basal friction. The balance between potential energy, kinetic energy and frictional energy loss is determined by the position of an energy line connecting the physical source and terminus of the deposit (Hsü 1975, 1978). Albert Heim first used this energy-balance approach in his study of the Elm, Switzerland rockfall avalanche of 1881. Energy lines have recently been applied in studies of pyroclastic flow deposits by Sheridan (1979), Malin and Sheridan (1982), Hoblitt (1986), and Begét and Limke (1988). Equations of motion, from elementary physics for a mass sliding down an inclined plane, have been used to estimate mean velocities and duration of movement by Heim (described in Hsü 1978), McSaveney (1978), and Ui et al. (1986), and were also used in this study.

Walker (1971) and Sparks (1976) have plotted median grain diameter versus standard deviation of diameter (after Inman 1952) for 1600 samples of pyroclastic fall and flow deposits, and they observed distinct but slightly overlapping fields for each. Their data are for ignimbrites, which contain a greater concentration of pumice clasts than do Merapi-type (MacDonald 1972) block and ash flows. Grain size studies of very coarse clastic deposits face the problem of representative sampling. Kellerhals and Bray (1971) devised a taped-grid method which samples only the coarsest fraction of poorly sorted fluvial deposits; the fine fraction is sampled for sieve analysis. The resulting weight percent and numerical data are then combined using the technique of Sahu (1964), producing a grain size distribution covering the entire range of sizes found within the deposit. One can interpret from the size distribution the transportation of the particles and/or the hydrodynamics of flow processes (see references in Fisher and Schmincke 1984). Rodine and Johnson (1976) have shown that mud-mediated debris flows can have clast concentrations as high as 95% by volume without significant particle interlocking and consequent flow freezing. Extremely poor sorting provides high debris density which reduces the apparent internal friction of the mixture.

### 1.2 Location Description.

Mt. St. Augustine has formed a small (12 km diameter) stratovolcanic island 285 km southwest of Anchorage in south-central Alaska (fig. 1.1). As part of the Aleutian volcanic arc, its position lies along the strike of a deep active seismic zone marking the site of convergence of the Pacific and North American crustal plates (Kienle and Swanson 1985). Mt. St. Augustine is the most active volcano in the eastern Aleutian arc. Detailed studies of the geologic history are found in Johnston (1978), Kienle and Forbes (1976), and Kienle and Swanson (1985).

Access to Augustine Island is by float plane from Homer, Alaska, 90 air km to the east (fig. 1.1). Kachemak Air (B. DeCrefft, proprietor) provides good service at reasonable cost

with a choice of aircraft: de Havilland Otter and Beaver, and Cessna 185. Landings are made in the West Augustine lagoon near the University of Alaska Fairbanks Geophysical Institute (UAFGI) base camp hut. Access to the pyroclastic fan on the north side of the island is easiest from another UAFGI hut located at Burr Point; it is possible to hike from West Augustine along the beach at low tide.

### 1.3 1986 Eruption.

The eruptive style of Mt. St. Augustine has been consistent throughout the volcano's historic activity: precursor seismicity is followed by explosive ash and pumice ejection, followed by dome-building activity. The general chemical similarity between prehistoric and modern eruptive products indicates that magma composition has remained relatively constant, with $SiO_2$ contents averaging 60%. Details of Mt. St. Augustine's petrologic evolution and petrology of recent eruptive products are found in Daley (1986), Harris et al. (1987), and Harris (1991).

The following chronology of the 1986 eruption of Mt. St. Augustine is summarized from excellent accounts in Kienle et al. (1986) and Swanson and Kienle (1988).

1. Precursor seisimicity is first detected in July, 1985.
2. Main eruptive period begins on the morning of March 27, 1986 and lasts until April 8, 1986.
    a. Part of the 1976 lava dome is explosively removed, and eruption column heights reached 12,000 m.
    b. Numerous pyroclastic flows generated by column collapse are directed through a breach in the north side of the summit crater. Some are large enough to enter the sea to the east and west of Burr Point, 6 km away.

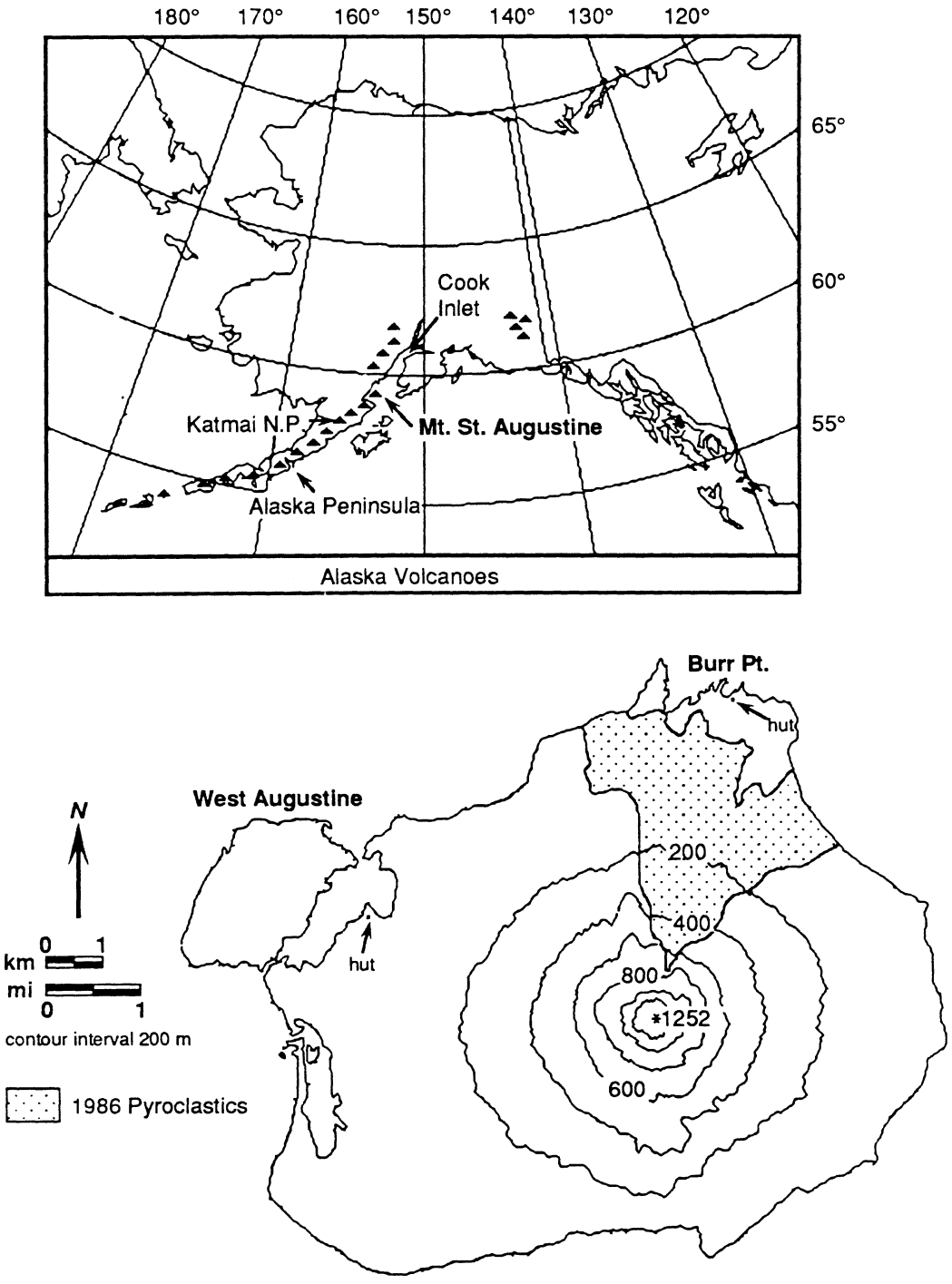


**Fig. 1.1** Location of study area. Pyroclastic deposits observed in this study are all located within the patterned area. Some pumice flows resulting from column collapse are also located outside this area, principally on the east and south flanks of the volcano.

3. Second eruptive period, from April 23 until April 28, 1986.
    a. A short, blocky lava flow is extruded from the base of the 1976 dome remnant, and a new dome grows in the crater.
    b. Numerous block and ash flows resulting from dome collapse are emplaced on the pyroclastic fan; most are of insufficient volume to reach the sea.
4. Third eruptive period, from August 19 to 31, 1986. Renewed dome growth produces ash columns to 3000 m, and generates smaller scale block and ash flows by dome collapse.

The distribution of the volcanogenic deposits from the 1986 eruption activity is shown in fig. 1.2. This map includes deposits emplaced as late as August, 1987 only.

### 1.4 1986 Deposits.

The Plinian phase of the main eruptive period (March 27–April 8) generated over one hundred pyroclastic flows originating as pumice flows and as block and ash flows from the collapse of older dome material (Miller et al. 1987). Deposits on the west side of Burr Point are matrix-supported and pumiceous, but with a relatively high proportion of lithic blocks and sand-sized lithic fragments. The character of these deposits suggests that they may have resulted from stoping of older lithic dome material from the new vent by explosive jetting of juvenile pumice. Another explanation for these deposits is that they resulted from the turbulent mixing of pumice and ash from the vent with contemporaneous collapse of older dome material; each of these flows would have followed generally the same path down to the apex of the pyroclastic fan. The surface of these deposits is smooth and devoid of distinct channels and levees, although low ($< 0.5$ m) longitudinal ridges, which parallel flow direction, can be discerned in the field and on airphotos.

Clast-supported pumice flow deposits, devoid of lithic fragments, are exposed on the east side of Burr Point and are partially reworked and buried on the west side of the pyroclastic fan (fig. 1.2). Pumice blocks are well rounded, and the matrix consists of

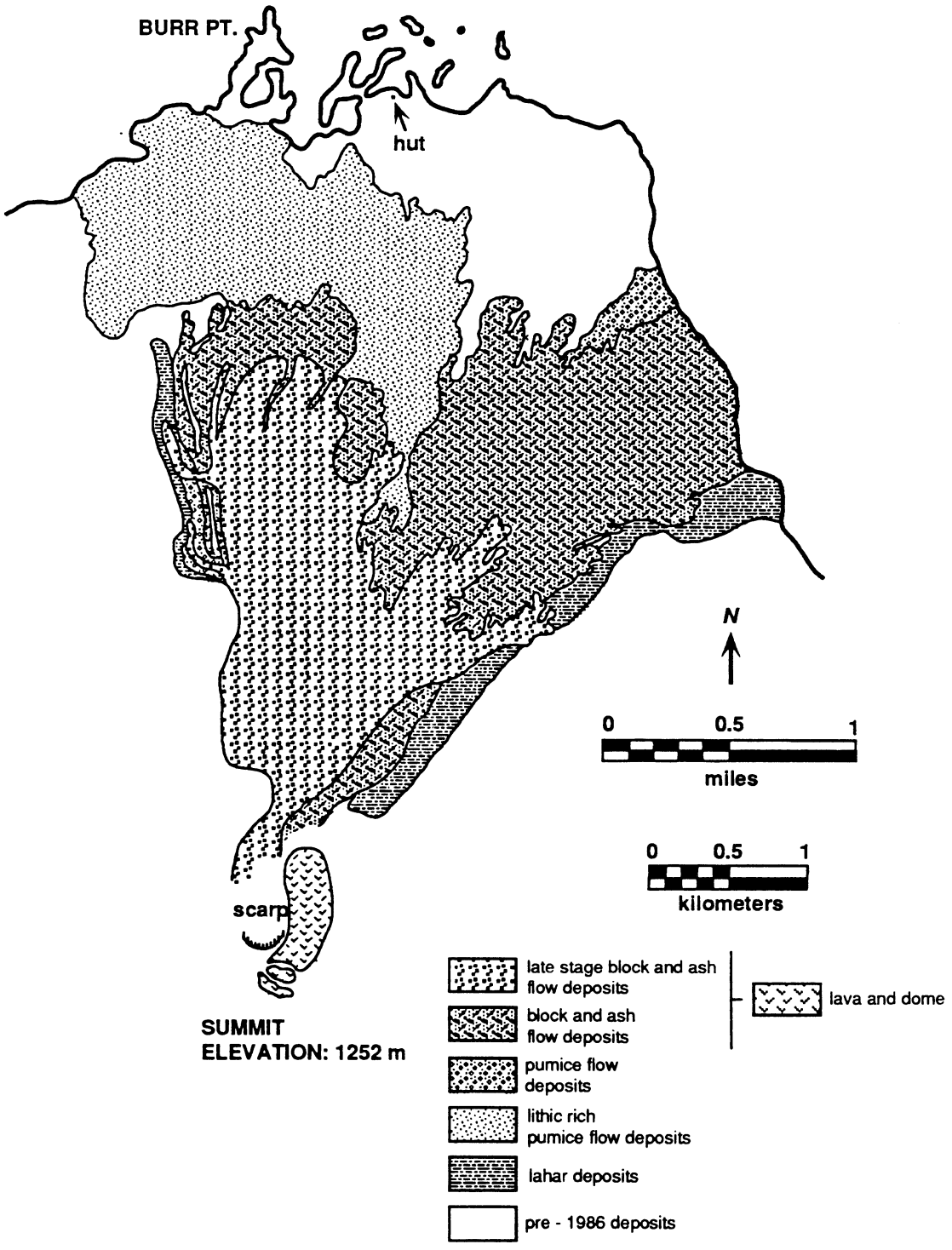


**Fig. 1.2** Surficial geology of pyroclastic fan as of August, 1987.

pulverized pumice, ash, and lapilli. Distinct channels and levees are evident; the levees are generally less than 1 m thick, and they rise less than 0.7 m above the channel surface.

During the second eruptive period (April 23–28), extrusion of the new dome and lava flow generated many block and ash flows. These deposits buried much of the pyroclastic fan, and some flows were voluminous enough to reach the sea on the east side of Burr Point (fig. 1.2). Vertical sections through the lithic block and ash flow deposits have been exposed by wave action at the beach and by stream erosion on the west side of the fan. Measured sections are presented in fig. 1.3a and b; the modeling scheme is after Sparks et al. (1973).

In section B1, the exposed flow unit is underlain by a 1-cm thick continuous layer of reddish-buff fine ash, interpreted to result from pre-emplacement airfall ash deposition. In the lower flow unit in section S2, this airfall ash is 5 cm thick. Above the airfall ash in the lower flow unit in section S2 is a 2-cm thick layer of fines-depleted sand-sized grey ash. This ash is interpreted to be a layer 1 deposit, reflecting the transit of a ground surge ahead of the advancing pyroclastic flow. Overlying the fine ash is a 6–10-cm thick layer of coarse ash, depleted in fines and devoid of clasts larger than lapilli, corresponding to layer 2a; this layer of ash is considered to represent the sheared base of the block and ash flow.

The bulk of the flow deposit is layer 2b, which is interpreted to represent the material that passively rode as a plug above the basal shear zone. Layer 2b consists of a 1.5–3.0-m thick unsorted, weakly reversely graded bed of blocks, lapilli, and coarse and fine ash. No sedimentary structures were observed in layer 2b, which, when combined with the lack of sorting, suggests that little or no internal shearing or turbulent flow occurred during emplacement. Although the massive character of layer 2b could be attributed to thorough chaotic mixing, the presence of uniform and undisturbed layers 1 and 2a seems to preclude this possibility.

Overlying the block and ash flow deposits in some areas are ash cloud deposits (layer 3 of Sparks et al. 1973). These deposits are between 5 and 20 cm thick and consist of bedded

coarse ash depleted in fines. Most often they are preserved on topographic highs such as older debris avalanche hummocks on the lower reaches of the pyroclastic fan.

On the surface, the block and ash flow units display well-developed levees, channels, and terminal lobes. The levees tend to be clast supported and much coarser grained than the matrix supported channel and terminal lobe deposits. Levee thicknesses range between 0.5 and 3 m, depending on the size of the flow unit and the proximity to the source. Very large levees ($> 3$ m) are most likely constructed from multiple flow events.

An important morphological feature of pyroclastic flow deposits, and of other types of sediment gravity flow deposits, is *superelevation.* In places where the channel/levee deposit is curved (in map view), the levee on the outside of the curve is always thicker than the levee on the inside; the outer levee is higher, i.e., superelevated, with respect to the inner. The difference in levee heights records the tilt of the flow surface due to centripetal forces as it moved along a curved path. From this tilt, one can estimate mean flow velocity of the material at that location (Johnson and Rodine 1984). Flow velocity can also be estimated at topographic barriers, such as debris avalanche hummocks, onto which the overriding ash cloud has decoupled from the basal underflow, run up, and deposited. A simple relationship exists between the elevation gained by the ash cloud deposit and its velocity of emplacement (Streeter and Wylie 1985); this relationship was used in the calculation of the pyroclastic flow velocity at several locations at Mt. St. Augustine.

Other deposits related to the 1986 eruptions are lahars and late-stage block and ash flow deposits associated with the third eruptive period. Lahar deposits are exposed on the margins of the pyroclastic fan and as an apron on the upper slopes of the entire volcano. Following the third eruptive period in 1986, late-stage block and ash flow deposits were emplaced over much of the pyroclastic fan (fig. 1.2). These deposits were first observed during August 1987. Distinct flow units having channel-levee-terminal lobe morphology are evident in these late deposits, and vertical sections through them show the same structure

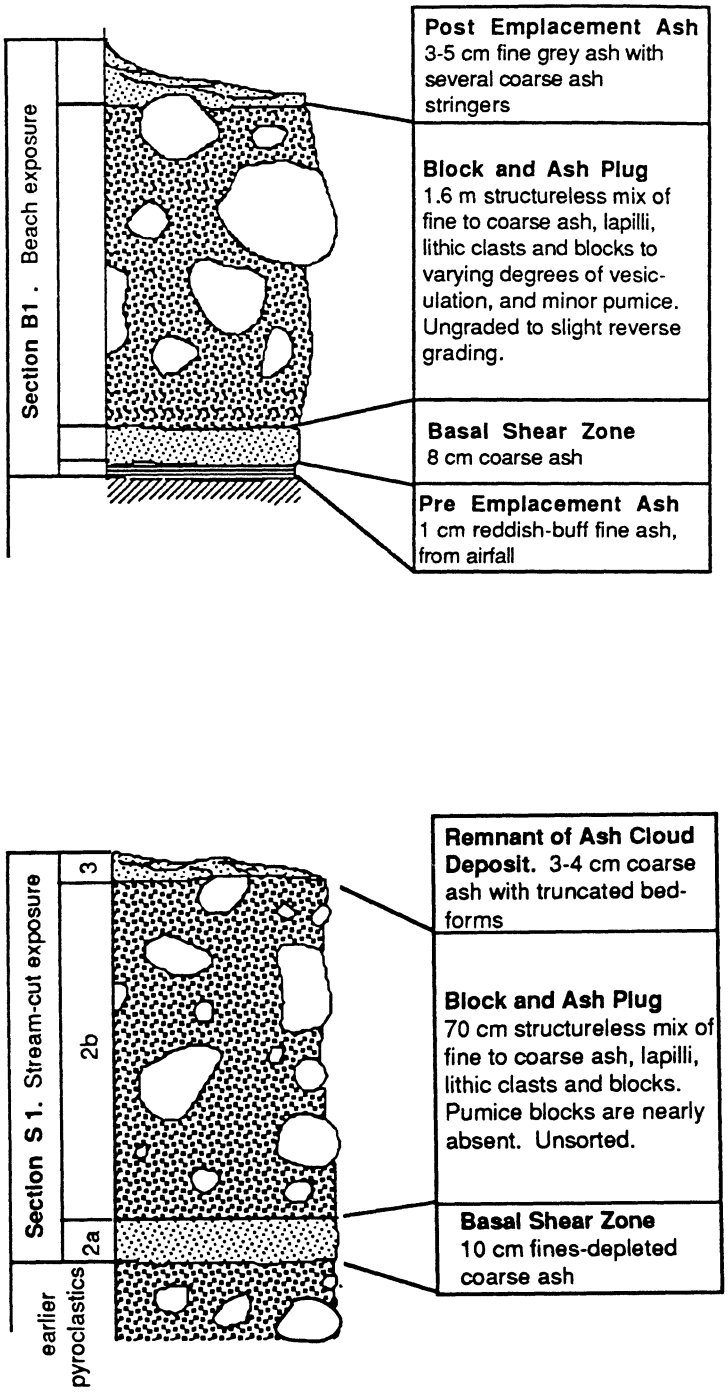


**Fig. 1.3a** Vertical sections through pyroclastic flow deposits. Section B1 is exposed at the beach east of Burr Point. Section S1 is exposed in a stream gully eroded into the pyroclastic fan following the 1986 eruption.

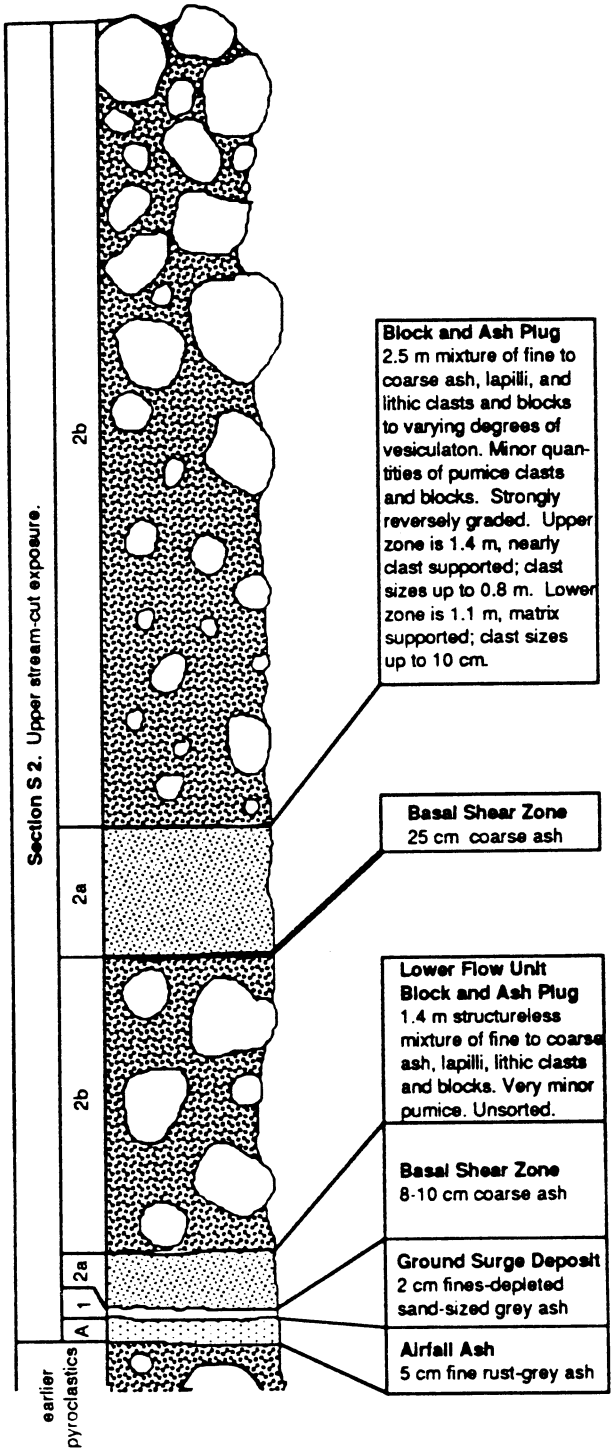


**Fig. 1.3b** Vertical section through two successive block and ash flow deposits.

within flow units as do the earlier deposits. A 3–5 m scarp was observed in 1987 at the 900-m elevation on the lower northern flank of the 1986 dome and may possibly be the origin of these late-stage deposits.

### 1.5 Field Methods.

Field data were collected by the author during two visits to the volcano: the first was from June 27 to July 17, 1986, and the second was from August 23 to September 2, 1987. Station locations for the two field seasons are shown in figs. 1.4 and 1.5.

Morphometric data for the individual flow units include channel widths and estimates of flow depths, heights of lateral levees, slope of channel/levee deposits in direction of flow, and the angles of superelevation. Distances were measured with a Leitz 100-m fiberglass-cored surveying chain with a precision of 2 mm. Angles were measured with a tripod-mounted Abney level with inclinometer and stadia, sighted on $\frac{3}{4}$-inch diameter galvanized steel rods which were pounded into the deposit to a constant height of 1 m. Fig. 1.6 shows the measuring techniques in use. Precision of the inclinometer is 10 minutes of a degree. For large levees, heights were obtained trigonometrically from angles of inclination sighted to the levee crests from outside the flow deposit. Smaller levee heights ($\approx$ 1 m or less) were measured using the chain held vertically. Angle of superelevation was determined with the inclinometer by sighting from the crest of the inner levee to the crest of the outer levee. Note that the levee thicknesses used for determination of rheological properties were obtained from straight reaches of the flow deposit. This practice avoids the possibility of measuring superelevation-induced thickness. At each station, grain size measurements were taken and samples were collected for sieve analysis; the details of these processes will be provided in Chapter 4. Maps of lithologic contacts, station locations, and flow units outlines were completed using airphotos shot on September 9, 1986.

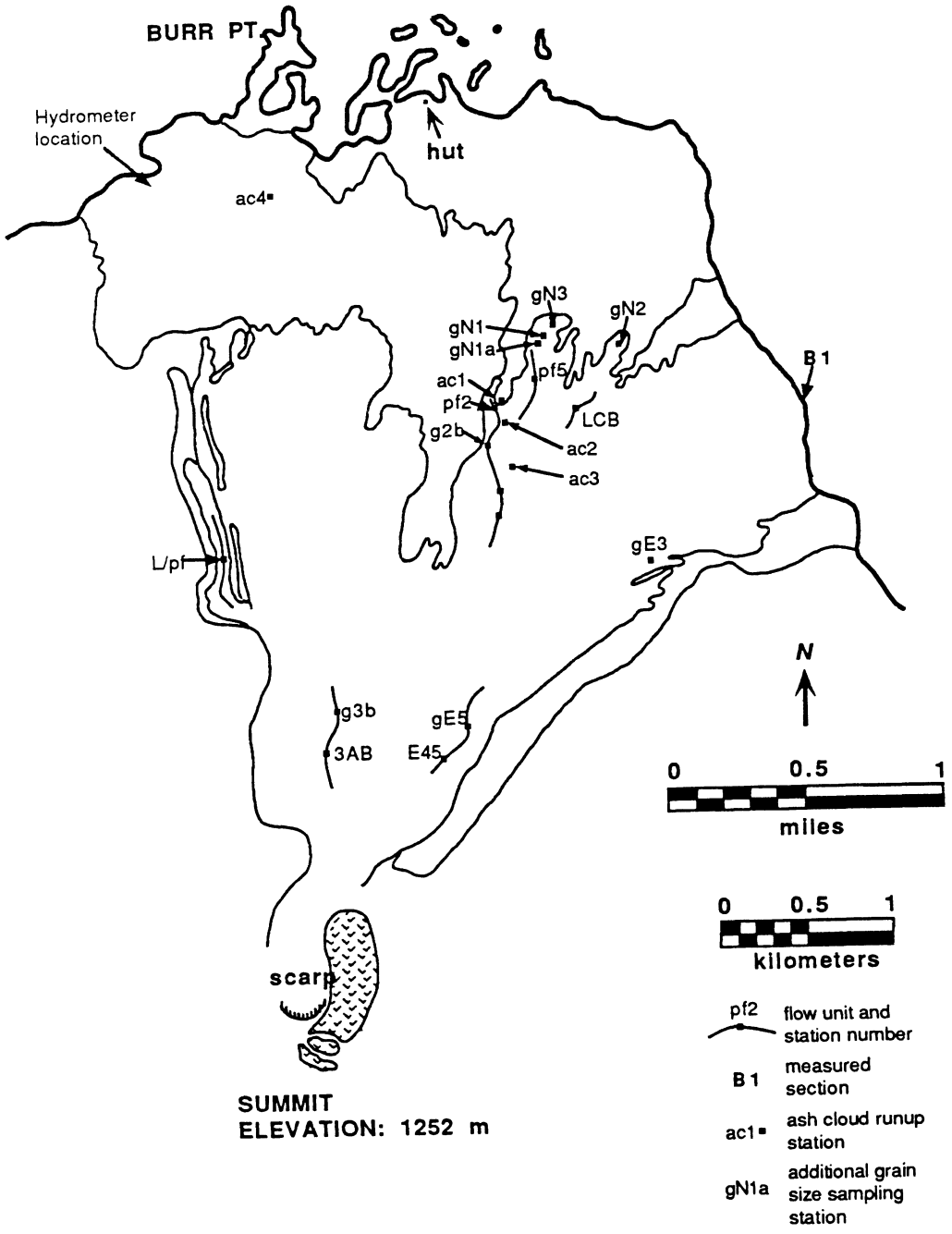


**Fig. 1.4** 1986 Field season stations map. Grain size sampling was performed at all indicated stations.

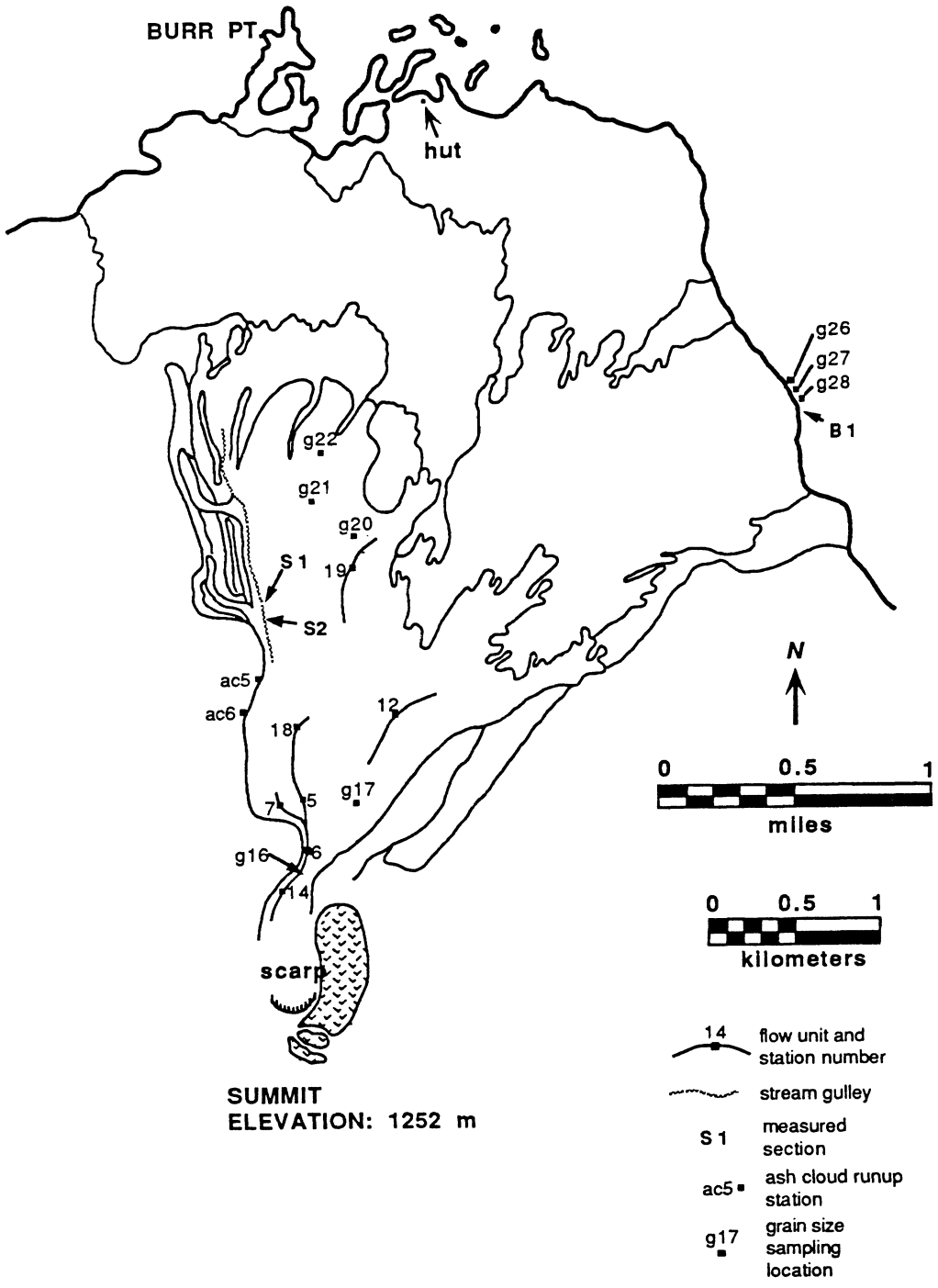


**Fig. 1.5** 1987 Field season stations map. Grain size sampling was performed only at station numbers preceded by "g."

### 1.6 Purpose and Scope of Research.

Kinetic, rheologic, and sedimentologic data were collected on recently active pyroclastic flows at Mt. St. Augustine to provide realistic constraints on the behavior of small pyroclastic flows. These data were then used to develop computer models for the behavior of pyroclastic flows, based upon the calculated effective rheological properties of density, yield strength, and viscosity. Complex and numerically intractable grain-to-grain interactions and variable flow mechanisms were not considered in the computer modeling. The 1986 eruptions at Mt. St. Augustine provided a unique opportunity to study the very fresh pyroclastic deposits whose morphologies reflect rheological conditions at the time of emplacement.

Three one-dimensional kinematic models were developed which retrodict emplacement velocities of some of the 1986 pyroclastic flows. The simplifying assumptions required for their use are given in Chapter 3. The results of these models are compared with observed flow velocities and reconstructed velocities estimated from superelevation of the levee deposits and from elevation gain of flows crossing topographic barriers. The goal of these modeling studies is to develop simple yet physically rigorous methods for reconstructing or predicting pyroclastic flow behavior. The applicability of these models is not limited to the 1986 pyroclastic flows at Mt. St. Augustine: if the controlling rheological and physical parameters can be determined from field data, these models can be used to analyze or predict the behavior of pyroclastic flows at other volcanoes.

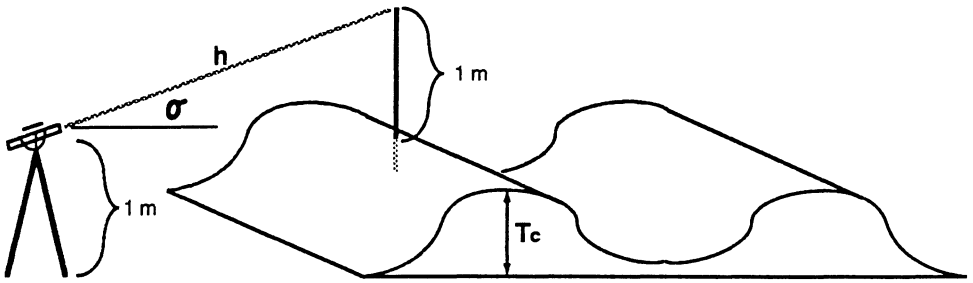


$T_c = \sin\sigma(h)$

**Fig. 1.6** Technique of measuring levee thicknesses.

## CHAPTER 2:

## RHEOLOGICAL PROPERTIES OF PYROCLASTIC FLOWS

### 2.1 Background.

Rheology is that branch of physics which describes the strain behavior of various materials in response to applied stress. Stress is defined as a force per unit area; it is a tensor quantity and does not have a specific direction assigned to it. Force is a vector quantity having both direction and magnitude.

There are three types of stress: tension or compression, hydrostatic pressure, and shear.

Tension or compression results when a body is acted upon by equal and opposite forces perpendicular to its cross-sectional area. Tensile or compressive strain is the ratio of the increase or decrease in length of the body (parallel to the force vector) to the original length.

Hydrostatic pressure is a force exerted by fluid on a surface; the fluid's force on a surface oriented in any direction is normal to the surface. The strain resulting from hydrostatic pressure is volumetric strain—i.e., the ratio of the decrease in volume of the body to the original volume.

Shear stress results when a tangential force (gravitional force for natural flows) is distributed over the surface of a body or material. In fig. 2.1, a prism of any real material is being deformed in shear by the force $F_{\|}$ applied to area $A$ of its top surface. Shear stress $\tau = F_{\|}/A$. The strain is defined as the ratio of the displacement $U$ to the height $H$, or

$$\frac{U}{H} = \tan\phi,$$

where $\phi$ is the angle formed due to the prism's displacement. In practice, $U$ is generally much smaller than $H$, so $U/H \approx \phi$. The magnitude of the displacement $U$ is dependent

on $\tau$, height of the prism $H$, and a material-dependent constant $\xi$ called the shear modulus or modulus of rigidity (Reiner 1960). If we define "rigid" materials as those having a high modulus of rigidity, it follows that

$$\phi = \frac{U}{H} = \frac{\tau}{\xi}$$

and

$$\tau = \xi\phi. \tag{2.1}$$

Equation (2.1) is the rheological equation of an elastic solid.

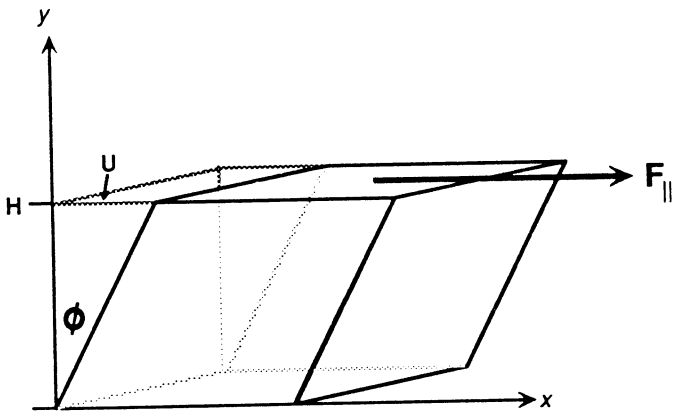


**Fig. 2.1** Simple shear of a prism.

In the classical rheological parlance, substances are modeled as either elastic solids, plastic solids, or viscous liquids (gases being liquids of extremely low viscosity); all real materials possess all rheological properties to varying degrees (Reiner 1960). A perfectly elastic body will respond to an applied stress according to equation (2.1), and when the stress is relaxed, the body will return to its original state with no permanent deformation (fig. 2.2a). All strain in elastic materials is completely recovered when the stress is relaxed.

A perfectly plastic material will behave elastically until a threshold stress is reached, at which point the material yields or experiences permanent deformation and begins to flow. When the applied shear stress exceeds the threshold or yield stress, flow is accelerated indefinitely, or until the material is exhausted. The rheological properties of a flowing plastic can be described so that

$$\tau = K \tag{2.2}$$

where $K$ is the yield stress. When shear stress drops below the yield value $K$, flow deformation stops, and the material relaxes according to (2.1), recovering part of the total deformation (fig. 2.2b).

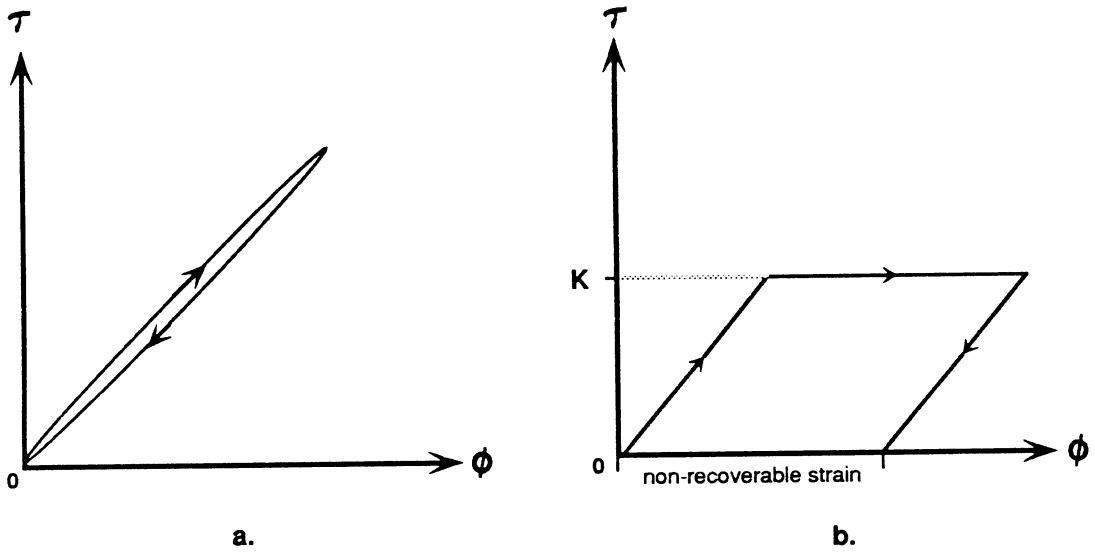


**Fig. 2.2** Stress-strain diagrams for elastic and plastic bodies. a. Perfectly elastic material returns to its unstrained state when $\tau$ is released. No hysteresis is implied by the appearance of the stress-strain looping path. b. Perfectly plastic material deforms indefinitely at $\tau = K$. For $\tau < K$, behavior is that of a perfect elastic.

Plastic materials behave elastically at stress levels below the yield value. Elastic materials subjected to increasing stress will rupture when the breaking stress is reached. Plastic yielding and brittle rupture define the upper limit of a material's *strength*: when the applied stress exceeds the strength, failure occurs (Reiner 1960).

For viscous liquids, a fluid is defined as a substance that deforms continuously when subjected to a shear stress, no matter how small that stress may be. The internal friction of a fluid is called viscosity, and it offers resistance to shear deformation. In fig. 2.3 a fluid is placed between two parallel plates separated by a small thickness $t$. Force $F$ applied to the upper plate having area $A$ causes the plate to move with a steady, non-zero velocity $U'$. Motion of the upper plate imparts a stress $\tau$ on the fluid, and the fluid is displaced from *abcd* to *ab'c'd*. Velocity $u$ varies from zero at the fixed lower plate to $U'$ at the moving plate.

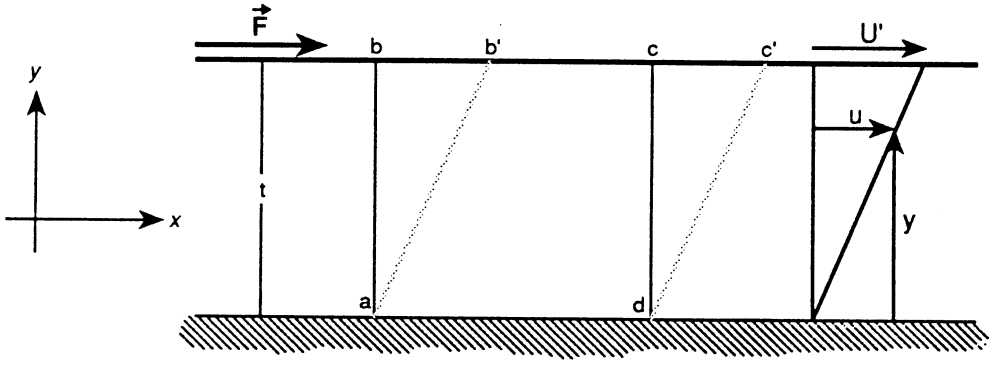


**Fig. 2.3** Fluid deformation resulting from a shear stress. Force $F$ on upper plate of area $A$ imparts a shear stress $\tau$ on the upper boundary of the fluid.

$\tau$ is related to $U'$ and $t$ by a fluid-dependent proportionality factor, called viscosity $\eta$, by

$$\tau = \eta \frac{U'}{t}.$$

$U'/t$ is the rate of angular deformation of the fluid, and is analogous to the displacement gradient in elastic materials. The most general form of this rate is $du/dy$, expressing the velocity change divided by the distance over which the change occurs. The rheological equation of a fluid then becomes

$$\tau = \eta \frac{du}{dy} \tag{2.3}$$

which is Newton's Law of Viscosity (Streeter and Wylie 1985). Fluids behaving according to equation (2.3) are termed Newtonian fluids.

Viscosity must be understood in terms of momentum transfer. For liquids, molecules are bound by cohesion such that when one layer moves relative to an adjacent layer, the cohesion transfers momentum from one side to the other. This transfer of energy sets up an apparent shear stress that resists the relative motion and tends to equalize the velocities of adjacent layers. For dry sediment flows, momentum transfer occurs through the myriad collisions between the particles.

The rheological behavior of all real materials can be described by one or a combination of these fundamental relationships:

$$\tau = \xi\phi \tag{2.1}$$

$$\tau = K \tag{2.2}$$

$$\tau = \eta \frac{du}{dy} \tag{2.3}$$

Geological materials possess rheological properties which lie along the continuum of elastic, plastic, and viscous behavior. A cube of unweathered granite and a blade of muscovite behave elastically up to their breaking strengths. Rhyolitic lava and glacial ice behave as

imperfect plastics. All water-mediated sediment gravity flows exhibit viscous flow behavior. For debris flows, the purely viscous relationship (2.3) is only a first approximation because their deposits do not spread infinitely on a flat plane. The fact that the deposits have a thickness greater than one mean grain size suggests that the material possessed an apparent cohesiveness or strength which, when no longer overcome by shear stress, caused the flow to "freeze." A better approximation to debris-flow rheology incorporates plastic strength with viscous flow.

The *Bingham* model accounts for strength and viscosity by combining the relationships (2.2) and (2.3). The equation of the ideal Bingham material is

$$\tau = K + \eta_b \frac{du}{dy} \tag{2.4}$$

where $\eta_b$ is the coefficient of Bingham viscosity. The Bingham model states that the minimum stress needed to initiate flow is the yield strength $K$, and that at stress levels greater than $K$, the steady-state velocity distribution will be proportional to the viscosity coefficient $\eta_b$. The Bingham model accounts for two important observations on debris flows: 1) they flow at perceptible rates; and 2) their deposit morphology reflects flow velocity (Johnson and Rodine 1984).

Pyroclastic flows at Mt. St. Augustine are herein modeled as Bingham substances because their deposit morphology suggests the presence of material strength. Several recent studies of pyroclastic flow dynamics (Limke and Begét 1986 and 1989; Begét and Limke 1988; Freundt and Schmincke 1986; Wilson and Head 1981; Sheridan 1979; Davies et al. 1978) have shown that pyroclastics have some mechanical strength and illustrate the applicability of the Bingham approach in characterizing pyroclastic flows. Other recent work on rockfall avalanche mechanics (Eppler et al. 1987; Jones et al. 1984; Voight et al. 1983; McSaveney 1978) suggests the general applicability of this approach to studies of sediment gravity flows.

The parameters necessary to apply the models can be obtained directly from geological field data. More complex rheological models (Savage 1979; McTigue 1982; Valentine and Wohletz 1989; see also references in Chen 1987) may account for grain-to-grain interactions more explicitly than the Bingham approach, but these require the use of parameters which can only be arbitrarily estimated. The use of equation (2.4) requires only a knowledge of pyroclastic flow density, yield strength, and effective Bingham viscosity.

## 2.2 Density.

Before developing the yield-strength analysis, a near-direct means of determining pyroclastic flow density (Begét and Limke 1989) will be presented.

During the 1986 field season, an aluminum fishing float was found partially submerged in the surface of the lithic-rich pumice flow deposit near the north shore of Burr Point (see fig. 1.5). It is assumed that during emplacement of the pumice flow, the float was overtopped and then rose buoyantly through the partially fluidized flow due to an effective density contrast. Heat convected by the flow discolored the surface of the float where it was in contact with the sediment after the flow had come to rest. While it can be argued that the float was washed up by a storm tide onto the pumice flow after emplacement, it is unlikely that there would have been enough heat at the surface of the deposit to char and discolor the float after a large volume of seawater had been in contact with the deposit.

The degree of floatation indicated by the thermally oxidized and stained zone was essentially identical to that suggested by the position of the float in the deposit when collected. In that the degree of submergence of the float during flow emplacement is recorded by the discolored area, the float behaved as an effective hydrometer, and the density of the fluid (i.e., the pyroclastic flow) on which the float was found can be calculated.

The weight of a hydrometer is supported by a buoyant force which is equal to the weight of the carrying fluid displaced by the hydrometer (Streeter and Wylie 1985). The buoyant force $F_B$ is given by

$$F_B = \gamma V_{abc} \tag{2.5}$$

where $V_{abc}$ is the volume of the fluid displaced by the hydrometer (fig. 2.4), and the unit weight of the fluid is $\gamma = \rho g$, where $g$ is gravitational acceleration and $\rho$ is the fluid density.

The spherical fishing float acting as a hydrometer has a mass of 5.4 kg, corresponding to a force $F_B$ of 52.9 N. The volume of the float is calculated from

$$V_f = \frac{4}{3}\pi r^3$$

where radius $r = 0.25$ m (fig. 2.4). The submerged volume of the hydrometer is estimated by the Archimedean method, and is $3.99 \times 10^{-3}$ m$^3$, or 6% of the sphere volume. Solving (2.5) for $\gamma$, pyroclastic flow density is calculated to be 1360 kg/m$^3$. This value is thought to comprise a close upper limit for the actual density of the pumice flow as it was emplaced.

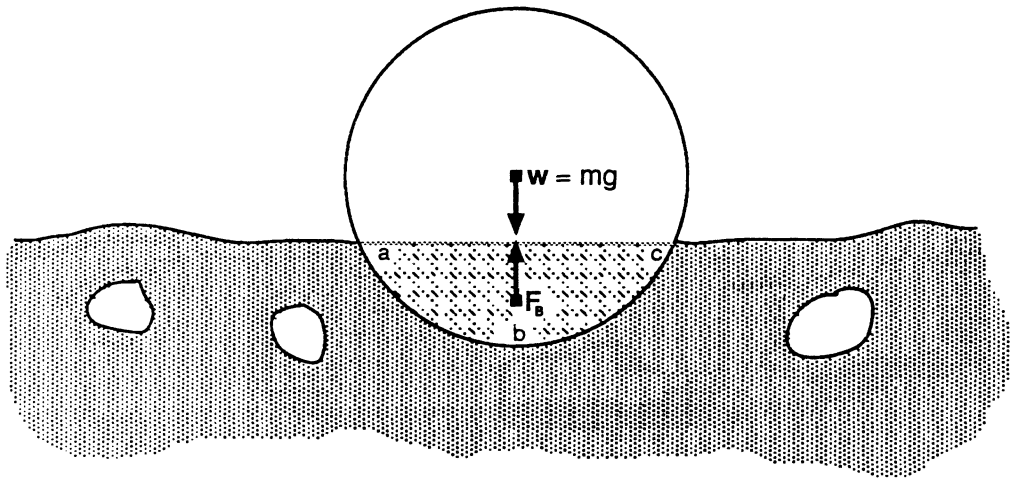


**Fig. 2.4** Forces acting on a hydrometer floating in a pyroclastic flow. (Diagram is highly schematic.)

The lithic block and ash flow deposits at Mt. St. Augustine contain very little pumice; assuming the same degree of fluidization, the densities of the moving block and ash flows were probably somewhat greater than 1360 kg/m$^3$. Sampling slightly compacted deposits of lithic pyroclastic flows (Chapter 4) showed an average matrix bulk density of 1730 kg/m$^3$. The precision of this value is probably reduced by the following effects, listed in order of decreasing importance: (1) samples were obtained from flow units several weeks after deposition, when flows had cooled and deflated (see figs. 1.5 and 1.6); (2) large clasts were present in the flow but were not sampled. In general, the density samples consisted of particles less than or equal to 2 mm in diameter. By sampling the compacted deposit, density is overestimated, and by sampling only the fine fraction of the deposit, density is underestimated. The magnitudes of these mutually offsetting effects are unknown; for the purposes of all subsequent rheological and kinematic modeling of the block and ash flows in this study, the average measured value of density employed is 1730 kg/m$^3$.

### 2.3 Yield Strength.

When the shear stress at the base of a moving Bingham flow falls below the yield strength of the material, the flow stops and freezes; the thickness of the resulting deposit records this critical rheological condition. At the instant of flow cessation, the driving force $F_{x+}$ becomes numerically equal to the resisting force $F_{x-}$, or

$$\sum F_x = 0. \tag{2.6}$$

Fig. 2.5 shows an element of a Bingham flow on a slope $\theta$,; the element has thickness $y$, length $dx$, and width $dz$. The element's weight is $w = \gamma\, y\, dx\, dz$; the driving force is the

downslope component of the element's weight, or

$$F_{x+} = \gamma\, y\, dx\, dz \sin\theta.$$

The resisting force comes from the product of shear stress and the surface area at the base of the element:

$$F_{x-} = \tau\, dx\, dz.$$

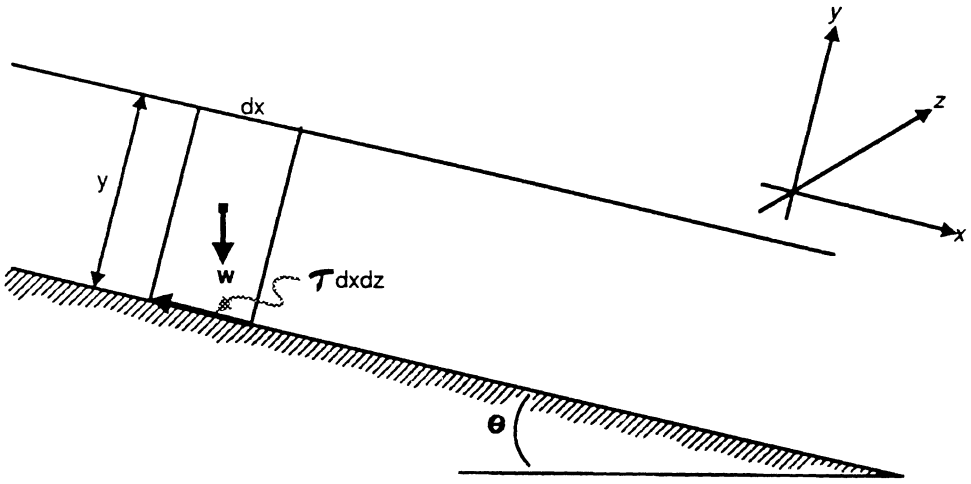


**Fig. 2.5** Forces acting on an element of Bingham material.

Balancing the forces as in equation (2.6),

$$\gamma\, y\, dx\, dz \sin\theta - \tau\, dx\, dz = 0$$

$$\tau = \gamma\, y \sin\theta. \tag{2.7}$$

The yield strength $K$ is equivalent to the shear stress at the base of the flow when movement stops, and at this instant, $y$ is called the critical thickness $T_c$:

$$K = \gamma\, T_c \sin\theta. \tag{2.8}$$

The critical thickness $T_c$ of pyroclastic flows is recorded in the height of the deposits' lateral levees (Limke and Begét 1986). The lateral levees consist of flow material whose

velocity has decreased to zero during flow emplacement. Observed debris flows (Johnson 1970, 1984) and physical models of mudflows (Hsü 1978, Johnson 1984) were found to have a cross-sectional shape mimicking an inverted, flattened semi-ellipse. Assuming that the cross-sectional shape of a block and ash flow is roughly semi-elliptical, it is suggested that the levees form where the flow thickness is less than or equal to the material-dependent $T_c$ at the margins of the flow. Calculated yield strengths of the 1986 Mt. St. Augustine pyroclastic flows are plotted in fig. 2.6 as a function of distance from the vent, and station locations are shown in figs. 1.4 and 1.5.

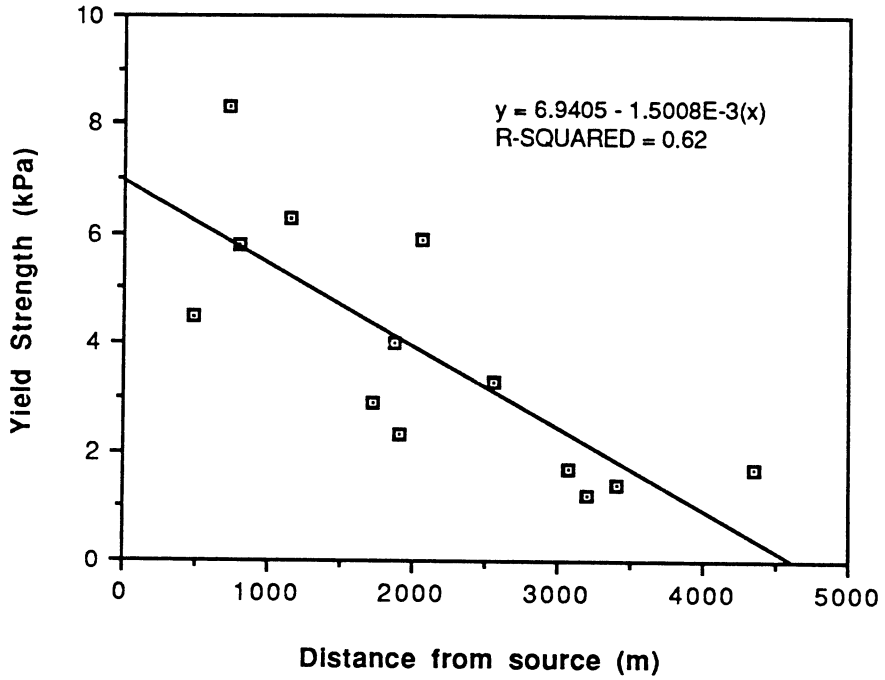


**Fig. 2.6** Yield strength distribution for the 1986 block and ash flows.

## 2.4 Viscosity.

At shear stress levels greater than the yield strength, Bingham materials flow as viscous fluids. Apparent Bingham viscosity $\eta_b$ is obtained by integrating equation (2.4) with respect

to flow depth $y$. $K$, $T_c$, and $v$ must also be known for the particular reach. Rearranging equation (2.4) gives

$$\int \eta_b \, dv = \int (\tau - K) \, dy. \tag{2.9}$$

$\tau$ is given in equation (2.7), so (2.9) becomes

$$\eta_b \int dv = \int (\gamma \, y \sin\theta - K) \, dy. \tag{2.10}$$

Integrating,

$$\eta_b v = \left[ \frac{y^2 \gamma \sin\theta}{2} - Ky \right] + C. \tag{2.11}$$

The constant of integration $C$ is determined from the boundary conditions of flow. The flow freezes when the depth equals the critical thickness, or $v = 0$ when $y = T_c$. Solving for $C$,

$$C = -\frac{{T_c}^2 \gamma \sin\theta}{2} + KT_c.$$

Equation (2.11) in usable form then becomes

$$\eta_b = \frac{1}{v} \left[ \frac{\gamma}{2} \sin\theta \, (y^2 - {T_c}^2) - K(y - T_c) \right]. \tag{2.12}$$

Equation (2.12) was evaluated with respect to field data for the 1986 pyroclastic flows at Mt. St. Augustine. For instance, values of flow velocity $v$ in equation (2.12) were reconstructed from flow morphology. Johnson and Rodine (1984) estimate mean velocity of debris flows through a curved reach of channel from

$$\overline{v} = (r \, g \tan\beta)^{0.5} \tag{2.13}$$

where $r$ is the radius of channel curvature and $\beta$ is the tilt of the flow surface recorded by the superelevation of the deposits (fig 2.7). A complete geometrical derivation of equation (2.13) is provided in Appendix A.

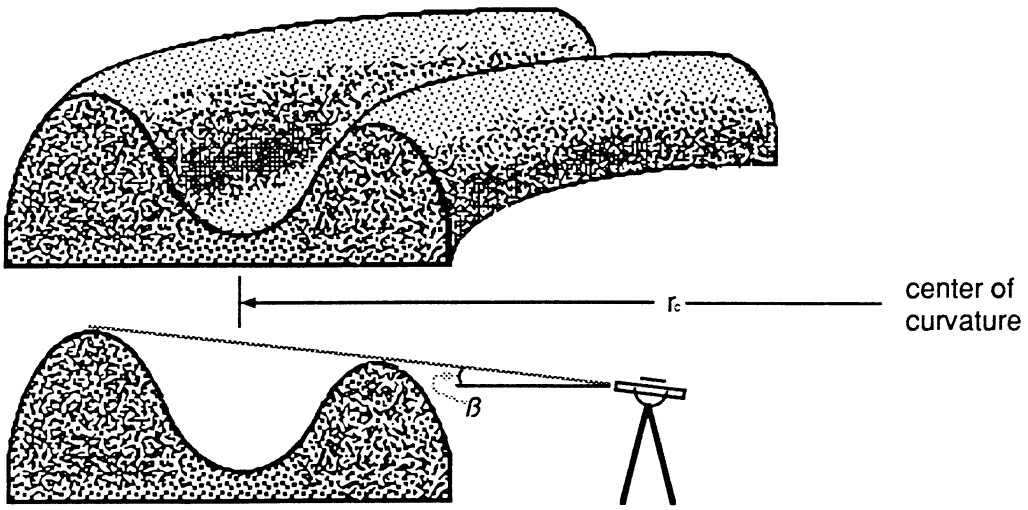


**Fig. 2.7** Superelevated marginal levee deposits at curved reaches of channel. Data required for velocity estimation are angle $\beta$ and radius of curvature $r_c$.

Values for flow depth $y$ in equation (2.12) are reconstructed from the centerline depth of the flow-unit channels. The flow units studied in this report fall into two categories: those deposited within previously constructed channels, found on the upper reaches of the pyroclastic fan; and those deposited onto relatively flat surfaces found on the lower reaches. During pyroclastic flow emplacement, the "stage" or absolute elevation of the top surface of the moving flow must be at least as high as the elevation of the levee crests. The flow depth $y$ therefore is a construct made up of the thickness of the levees, and either any additional channel depth exceeding $T_c$ (for flow units in the first category) or, for flow units in the second category, the height of the crest of the semi-elliptical cross section above $T_c$. (This height is arbitrarily set to be $0.5\,T_c$, in lieu of direct observational data.) Calculated Bingham viscosities are plotted in fig. 2.8 as a function of distance from the vent.

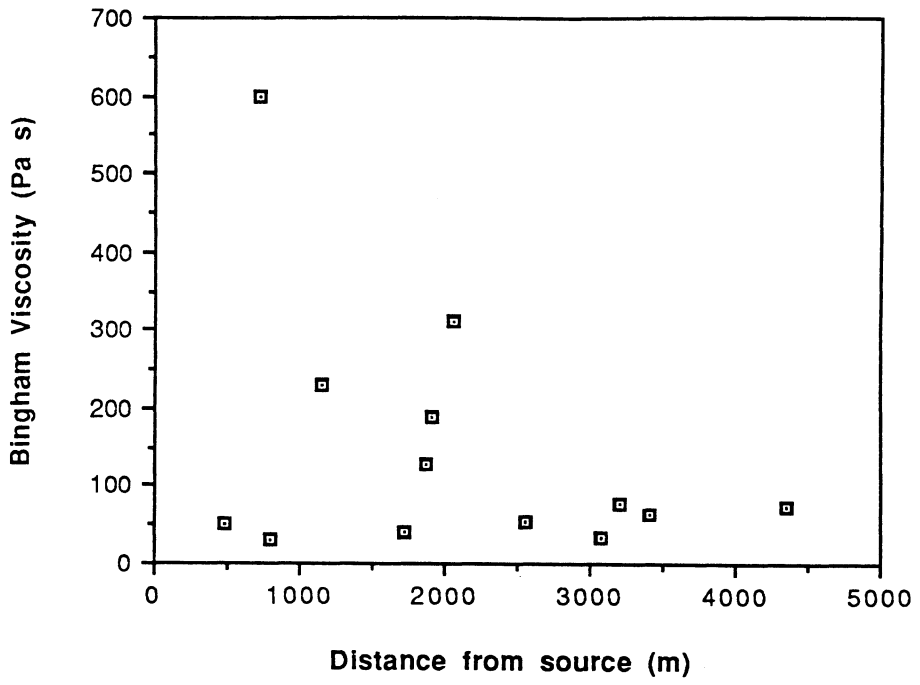


**Fig. 2.8** Bingham viscosity distribution for the 1986 block and ash flows.

## 2.5 Pyroclastic Flow Rheology.

Four rheological parameters, including unit weight $\gamma$, critical thickness $T_c$, yield strength $K$, and Bingham viscosity $\eta_b$ were determined at representative stations for the Mt. St. Augustine pyroclastic flows. The morphometric data collected at each station and the calculated rheological properties are summarized in Table 2.1.

Sources of error in the yield strength calculations are:

1. The constant value of unit weight $\gamma$ is 17,200 N/m$^3$; the assumption of incompressible flow is required because of lack of data to the contrary. However, because pyroclastic flows are inhomogeneous and partly fluidized by ingested air and magmatic gases, localized density variations are a certainty.
2. Instrument imprecision results in a maximum of 5% error in the measurements of critical thickness $T_c$ and slope $\theta$.

**Table 2.1. Rheological Summary of Mt. St. Augustine Flow Deposits.**

| Station number | Distance from source (m) | $\gamma$ ($\times 10^4$ N/m$^3$) | $T_c$ (m) | $\theta$ (°) | $K$ ($\times 10^3$ Pa) | $y$ (m) | $\overline{v}$ (m/s) | $\eta_b$ ($\times 10^1$ Pa s) |
|---|---|---|---|---|---|---|---|---|
| 14 | 480 | 1.72 | 1.5 | 10.0 | 4.5 | 2.5 | 29 | 5.2 |
| 6 | 730 | 1.72 | 2.0 | 14.0 | 8.3 | 5.0 | 31 | 60 |
| 5 | 790 | 1.72 | 1.4 | 14.0 | 5.8 | 2.0 | 25 | 3.0 |
| 7 | 1140 | 1.72 | 1.5 | 14.2 | 6.3 | 3.0 | 21 | 23 |
| 18 | 1720 | 1.72 | 0.8 | 12.0 | 2.9 | 1.5 | 22 | 4.0 |
| 12 | 1870 | 1.72 | 1.5 | 9.0 | 4.0 | 2.5 | 11 | 13 |
| 3AB | 1900 | 1.71 | 1.3 | 6.0 | 2.3 | 2.6 | 8.1 | 19 |
| E45 | 2050 | 1.71 | 2.0 | 10.0 | 5.9 | 4.0 | 19 | 31 |
| 19 | 2560 | 1.72 | 1.0 | 11.0 | 3.3 | 1.8 | 19 | 5.5 |
| pf5 | 3070 | 1.71 | 1.3 | 4.5 | 1.7 | 2.0* | 11 | 3.3 |
| L/pf | 3200 | 1.33† | 0.8 | 6.7 | 1.2 | 1.6 | 6.7 | 7.9 |
| pf2 | 3400 | 1.71 | 0.7 | 6.8 | 1.4 | 1.5 | 10 | 6.4 |
| LCB | 4360 | 1.71 | 1.7 | 3.3 | 1.7 | 2.6* | 7.7 | 7.6 |

* simulated value: $y = (1.5T_c)$.
†pumiceous pyroclastic flow: $\rho = 1360$ kg/m$^3$.

Referring to fig. 2.6, there is an apparent trend for the yield strength of pyroclastic flows at Mt. St. Augustine to decrease with increasing distance from the source. Polynomial regressions of degrees 1, 2, and 3 were performed to describe this trend mathematically. The level of significance, $\alpha$, is hereby established to be 0.10 for all statistical testing in this thesis. Choosing $\alpha = 0.10$ means that there is a 10% probability that the decisions/statements/conclusions resulting from tests will be incorrect, and that there is a 90% probability that they will be correct (Davis 1986). An F-test performed to test the fit of higher order polynomials to the plotted data indicates that the first-order regression equation,

$$K = 6.94 \times 10^3 + 1.50x \tag{2.14}$$

where $x$ is distance from source, is the most significant, and that higher order polynomials do not significantly improve the fit to the plotted points.

These data are highly suggestive of some time-dependent and/or distance-dependent process operating during pyroclastic flow emplacement whereby yield strength decreases.

The effects of this process are adequately described by equation (2.14). Speculation as to what this process is will be offered in Chapter 4.

Calculations of Bingham viscosity (Table 2.1, fig. 2.8) are subject to the same sources of error as are those for yield strength, plus others. Additional error arises as follows:

1. Flow depth $y$ must be estimated from the levee thickness plus any additional channel depth, because direct measurements of $y$ during emplacement are lacking. For flow units deposited on relatively flat surfaces (pf5 and pfBD), $y$ is set at a simulated value equal to $1.5\,T_c$.
2. Velocities reconstructed from superelevation are imprecise due to:
   a. error involved in determining the radius of curvature of the flow deposit ($\approx$ 10%);
   b. maximum 10% error in the measurement of angle of superelevation $\beta$.

   The maximum error in $v$ due to the combined effects of a. and b. is $\approx$ 15 %.

No systematic trend in Bingham viscosity vs. distance is apparent in fig. 2.8. F-tests of up to third-order polynomial regressions result in no significance at $\alpha = 0.10$.

For flow units 6 and pfE4, the high calculated $\eta_b$'s result from relatively greater channel depths than for the other flow units. Equation (2.12) is very sensitive to flow depth because this term is squared; small changes in $y$ result in large changes in $\eta_b$. Both of these stations are near the apex of the pyroclastic fan and probably served as distributary channels for a number of individual block and ash flows. It is hypothesized that some of these pyroclastic flows developed shear stresses at their bases great enough to erode and downcut the channel through which they flowed. In this way, the channel would be deepened by a flow that was not as deep. The present-day extreme depth of the channel could therefore be an artifact of earlier levee deposition followed by channel downcutting.

Table 2.2 provides rheological data for a number of different sediment gravity flow deposits throughout the world. The results for the Mt. St. Augustine pyroclastic flows fall within the ranges of the other reported values for pyroclastic flows, and suggest that the

1986 pyroclastic flows were characterized by viscosities ten to a thousand times less than high mobility volcanic debris avalanches and non-volcanic rockfalls.

**Table 2.2. Selected Published Rheological Data.**

| Type of deposit | Yield Strength ($\times 10^3$ Pa) | Bingham Viscosity (Pa s) | Location | Date | Reference |
|---|---|---|---|---|---|
| ignimbrite | 0.5 | 350 | Katmai, AK | 1912 | Begét & Limke (1988) |
| block and ash pf | 1.7-8.3 | 33-600 | Mt. St. Augustine, AK | 1986 | Limke & Begét (1989) |
| debris flow | 1.8-2.3 | 130 | Wrightwood, CA | 1969 | Johnson & Rodine (1984) |
| debris avalanche | 2-20 | $7\times10^4$ | Mt. St. Helens, WA | 1980 | Voight et al. (1983) |
| pumice flow | 0.4-18 | $30\text{-}2\times10^3$ | Mt. St. Helens, WA | 1980 | Wilson & Head (1981) |
| rockfall avalanche | 6-10 | — | Lassen Peak, CA | 300ybp | Eppler et al. (1987) |
| rockfall avalanche | 2 | $10^6$-$10^7$ | Sherman Glacier, AK | 1964 | McSaveney (1978) |
| ignimbrite | 0.2-1 | 0.5-5 | Laacher See, BRD | 11kybp | Freundt & Schmincke (1986) |
| mudflow | 0.4-1.1 | 20-320 | Mt. St. Helens, WA | 1980 | Fink et al. (1981) |

## 2.6 Flow Regimes.

Equation (2.12) is valid only for laminar viscous flow. Turbulent flow is accompanied by an apparent turbulent viscosity or eddy viscosity not accounted for in equation (2.12). Several dimensionless parameters have been developed to assess the flow regime of moving fluids. The Reynolds number **Re** is the ratio of the inertial energy to the viscosity of the fluid:

$$\mathbf{Re} = \frac{vy\rho}{\eta_n} \tag{2.15}$$

where $y$ is a characteristic length and $\eta_n$ is the coefficient of Newtonian viscosity defined as

$$\eta_n = \frac{1}{v}\left[\frac{\gamma}{2}y^2\sin\theta\right]. \tag{2.16}$$

The derivation of equation (2.16) from the rheological equation of a Newtonian fluid (2.3) is analogous to the derivation of equation (2.12).

The Reynolds number **Re** was developed for water flowing through pipes having diameter $y$. The transition from laminar to turbulent flow occurs around $\mathbf{Re} = 2000$ for pipe flow.

Bingham materials have different rheological properties than Newtonian fluids and therefore turbulence criteria must also be different. Middleton and Southard (1984) use the Bingham number **Bi**, given by

$$\mathbf{Bi} = \frac{Ky}{v\,\eta_b} \tag{2.17a}$$

to calibrate **Re** for Bingham materials when $K$ and $\eta_b$ are known. The critical Reynolds number for the onset of turbulent flow in Bingham materials is

$$\mathbf{Re}_c = 1000\,\mathbf{Bi}, \tag{2.17b}$$

and was determined through experimentation with Bingham plastics flowing through pipes.

A more appropriate parameter for flow-regime determination of fluids in open channels is the Froude number **Fr**, given by

$$\mathbf{Fr} = \frac{v^2}{gy}. \tag{2.17}$$

The Froude number is the ratio of the fluid velocity to the velocity of an oscillatory wave propagating through that fluid (Henderson 1966). Flow of water is said to be tranquil or subcritical when $\mathbf{Fr} < 1$, critical when $\mathbf{Fr} = 1$, and rapid or supercritical when $\mathbf{Fr} > 1$. For Bingham materials, the critical **Fr** is different because of their substantially different rheological properties. Valentine and Fisher (1986) have developed a modified Froude number $\mathbf{Fr}_m$ which is applicable to materials with assumed Bingham behavior:

$$\mathbf{Fr}_m = \frac{v^2}{y\,g(1-\frac{a}{y})\sin\theta}, \tag{2.18}$$

where $a = (y - T_c)$. The critical value of $\mathbf{Fr}_m$ is 1000.

Table 2.3 summarizes flow regime evaluations for the pyroclastic flow deposits studied at Mt. St. Augustine. Without exception, these deposits suggest that emplacement occurred under subcritical flow conditions. Of course, the criteria employed in Table 2.3 are subject to the same error sources as the rheological parameters from which they are calculated, but

it is unlikely that the results in Table 2.3 could be substantially changed. These results are consistent with the finding of Begét and Limke (1988) that some pyroclastic flows are characterized by subcritical flow during transport and emplacement. This indicates that the highly turbulent gas clouds which have been observed rising above propagating pyroclastic flows (Hoblitt 1986; Kienle et al. 1986), obscuring field observations of the underlying flows, are not representative of the body of the much denser pyroclastic flow which is hidden beneath the clouds.

Kienle's observations of an approaching pyroclastic flow front at close range (J. Kienle, personal communication, 1986) included the presence of four sustained counterrotating convection cells whose rotational axes were parallel to flow direction. This phenomenon may be considered as the pyroclastic analogue to secondary currents operating in rivers and other open channels. Counterrotating secondary currents are required because of the mean velocity distribution through the flow depth (Henderson 1966).

For the observed flow at Mt. St. Augustine, the observed secondary currents were observed only at the flow front where there was no effective backpressure inhibiting particle circulations/translations. Behind the flow front, there must exist an effective backpressure whereby the secondary currents are damped to some extent. The presence of minor, sustained secondary currents in the main body of the flow is not in itself indicative of a supercritical flow regime. In rivers, secondary currents exist under subcritical flow regimes. Supercritical flow regimes in pyroclastic flows with assumed Bingham rheology are ascertained via the modified Froude number, $\mathbf{Fr}_m$.

**Table 2.3. Flow Regime Assessment Parameters.**

| Station number | Distance from source (m) | Bi | $Re_c$ | $\eta_n$ | Re | $Fr_m$ |
|---|---|---|---|---|---|---|
| 14 | 480 | 7.5 | 7500 | 320 | 400 | 329 |
| 6 | 730 | 2.2 | 2200 | 1678 | 162 | 202 |
| 5 | 790 | 15 | 15000 | 330 | 270 | 188 |
| 7 | 1140 | 3.9 | 3900 | 904 | 122 | 122 |
| 18 | 1720 | 4.9 | 4900 | 183 | 317 | 297 |
| 12 | 1870 | 6.9 | 6900 | 764 | 63 | 53 |
| 3AB | 1900 | 3.9 | 3900 | 745 | 49 | 49 |
| E45 | 2050 | 4.0 | 4000 | 1250 | 106 | 106 |
| 19 | 2560 | 5.7 | 5700 | 280 | 214 | 193 |
| pf5 | 3070 | 9.3 | 9300 | 244 | 158 | 48 |
| L/pf | 3200 | 3.6 | 3600 | 296 | 49.3 | 49 |
| pf2 | 3400 | 3.3 | 3300 | 228 | 115 | 123 |
| LCB | 4360 | 7.6 | 7600 | 432 | 81 | 62 |

## CHAPTER 3:

## KINEMATIC MODELING OF PYROCLASTIC FLOWS

### 3.1 Energy Balance Considerations for Flowing Sediment.

Consider one case of a mass of geologic material resting unstably at some elevation above its surroundings. This material contains potential energy by virtue of its weight and elevation above an established datum. If motion is triggered, the material can begin to move downslope in response to gravity. Incipient motion is accompanied by disintegration and/or internal deformation of the originally coherent mass, and continued motion may result in a rapid increase in velocity. Potential energy decreases during flow as the material loses elevation, and as the material accelerates potential energy is converted into kinetic energy. The flow's kinetic energy, in turn, is dissipated by frictional energy losses. Eventually, the rate of potential energy conversion will no longer exceed the rate of frictional energy loss, and the material begins to decelerate. When the flow's kinetic energy is totally dissipated by frictional forces, the flow stops.

The above scenario is valid for *all* types of sediment gravity flows. The energy transformations do not change; only the mechanisms of motion and frictional dissipation distinguish the various types of geologic flows. A. Heim and E. Müller-Bernet (quoted in Hsü 1978) described these transformations from the fluid mechanical point of view in Heim's study of the 1881 rockfall-avalanche in Elm, Switzerland. As a means of comparison for different-sized rockfall avalanche deposits, Heim postulated the concept of the *Fahrböschung*, or the average slope of the avalanche's travel path. A more precise definition of fahrböschung is "the angle of the line (as measured from the horizontal) connecting the uppermost point from

which the rock mass broke away and the terminus of the [avalanche] deposit" (Hsü 1978). The fahrböschung is the angle of an "energy line" or the gradient of fluid potential for the flowing material, and it is analogous to the hydraulic grade line for pipe flow. The relationship between the fahrböschung and the energy transfers occurring in sediment gravity flows is illustrated in fig. 3.1.

The figure shows the path of the flow as curve $\overline{APQT}$, and the fahrböschung $\epsilon$, and energy line as $\overline{AOT}$. At point $A$, the material's energy consists only of stored potential energy represented by $H$. When motion begins, the conversion of potential to kinetic energy is rapid, owing to the steepness of fall, and frictional energy dissipation is relatively minor. When the flow reaches point $P$, the original potential energy has been reduced by the amount $\overline{NP}$ and converted into kinetic energy $\overline{OP}$ and cumulative frictional work $\overline{NO}$. Also, the slope of the flow path is greater than $\epsilon$, resulting in kinetic energy increase and flow acceleration. At point $Q$, the path slope equals $\epsilon$, acceleration goes to zero, the change in kinetic energy goes to zero, and all potential energy loss is converted into frictional work. Between points $Q$ and $T$, the path slope is less than $\epsilon$, and the flow decelerates. All potential energy loss and part of the accumulated kinetic energy is being converted into frictional work, until at point $T$ the cumulative frictional work becomes equal to the original potential energy $H$.

The total energy (potential + kinetic) available for the continued motion of a sediment gravity flow is provided by the orientation of the energy line. For the purposes of kinematic modeling, a more useful feature of the fahrböshung is that it serves to estimate the coefficient of friction for the moving flow. To do this, Coulomb's law of sliding friction is employed.

Fig. 3.2 shows a block having weight $w$ at rest on a slope of angle $\theta$. The forces acting on the block are: the normal force $N$ which is equal and opposite to the component of $w$ perpendicular to the surface; the driving force $F_{\parallel +}$ which is the downslope component of $w$; and the braking force $F_{\parallel -}$ which is proportional to the normal force $N$ by the coefficient of

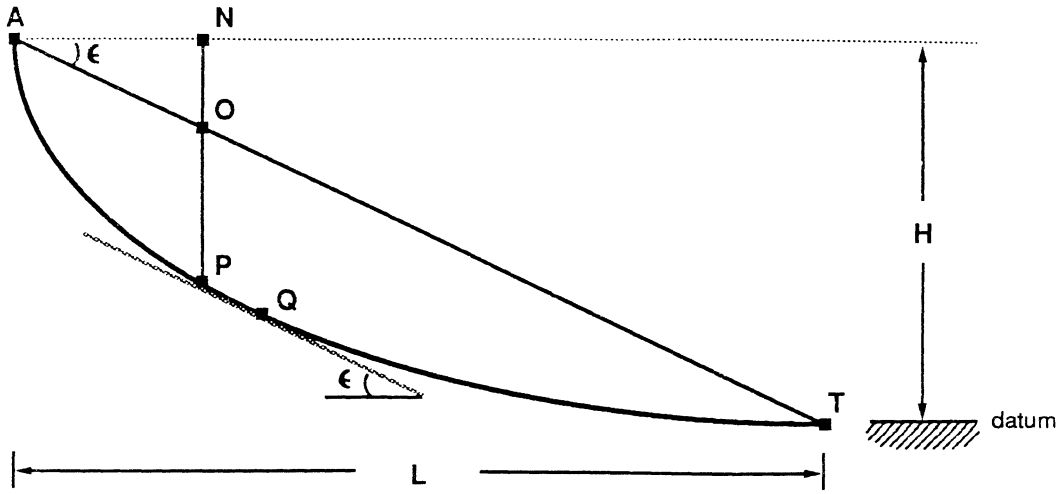


**Fig. 3.1** Relationship between the fahrböschung and energy transformations for sediment gravity flows.

sliding friction $\mu_s$. The block does not move in the $y$ direction, so the perpendicular forces are balanced:

$$\sum F_y = w\cos\theta - N = 0$$

$$w\cos\theta = N. \tag{3.1}$$

Motion with constant velocity in the $x$ direction begins when the parallel forces are balanced:

$$\sum F_x = w\sin\theta - \mu_s N = 0$$

$$w\sin\theta = \mu_s N. \tag{3.2}$$

Dividing (3.2) by (3.1) gives

$$\mu_s = \frac{\sin\theta}{\cos\theta} = \tan\theta \tag{3.3}$$

which is Coulomb's law of sliding friction. The value of $\mu_s$ determined for many rock materials by experimentation is about 0.6 (Hsü 1978), and is dependent only on the nature of the frictional contact between different sliding surfaces. Equation (3.3) is strictly valid only for material that slides.

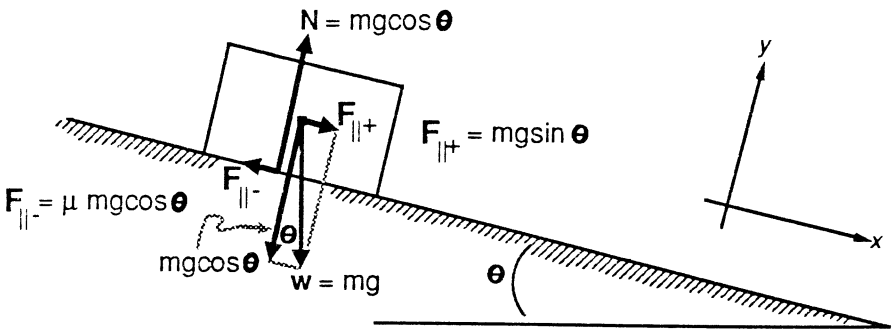


**Fig. 3.2** Forces acting on a block illustrating Coulomb's law of sliding friction.

The fahrböshung angle $\epsilon$ for sediment gravity flow deposits is analogous to the angle $\theta$ of Coulomb's law, and likewise a coefficient of friction $\mu_s$ can be estimated for the moving flows by

$$\mu_s = \frac{H}{L} = \tan \epsilon. \tag{3.4}$$

The coefficient of friction $\mu_s$ for a flow is assumed to include energy losses from several sources. While friction at the base of flow probably constitutes the major energy sink, some energy is probably consumed by particle collisions within the flow body and shear between the clasts in the flow. The friction coefficient $\mu_s$ derived from the calculation of a fahrböschung for a large flow is assumed to average such energy losses over the length of the flow.

For some large rockfall avalanche deposits, the fahrböschung should be drawn such that it connects the centers of gravity of the pre-fall material and the resulting deposit. At Elm, the fahrböschung connecting the source scarp and the deposit terminus is 16° ($\mu_s = 0.3$), and the "centers of gravity" line is 23° ($\mu_s = 0.4$). Both of these frictional coefficients

are significantly lower than the theoretical Coulomb value of 0.6. Heim (Hsü 1978) first attempted to explain the unusually low friction coefficient by attributing the discrepancy to lubrication by mud, and later Shreve (1968) proposed lubrication of large rockfalls by an air cushion beneath the flow.

From a study of many rockfall avalanche deposits, Heim discovered an inverse relationship between the frictional coefficient and the volume of flow deposits. This relationship is also evident for the observed pyroclastic flow deposits at Mt. St. Augustine. Heim envisioned a volume-dependent reduction in frictional resistance for large flows, and he compared this mechanism to the property of thixotropy. Heim emphasized that rockfall avalanches flow rather than slide, and that flowage occurs by interparticle collisions in which momentum is efficiently transferred from the rear to the front of the flow by the rebounding particles. The larger the flow, the more efficient this process is. In this light, the fahrböschung is interpreted only as an average rate of energy dissipation rather than as a coefficient of sliding friction. In fig. 3.1, the displacement from $A$ to $T$ represents the transmission of momentum from the uppermost particle in the pre-failure mass to the foremost particle resting at the deposit terminus. It does not necessarily represent the translation of the particles themselves.

### 3.2 Numerical Modeling Structure and Model 1.

All of the numerical models presented in this chapter predict the change in momentum of a pyroclastic flow that results from the difference between the driving force and the braking force acting on it. In each model the driving force is the downslope component of the flow's unit weight. The distinction between the three models lies in their choice of braking mechanisms. The models are one-dimensional and algebraic. The velocity of the modeled sediment package reflects the momentum transfer occurring in the flow. The momentum transfer is modeled from the source of the pyroclastic flows (i.e., the summit dome) to the

terminus of the deposit. It should be emphasized that the positions of the flow's center of mass are *not* modeled by this approach, and that the only particle translations that *are* modeled are for the clasts now at rest at the deposit terminus.

The basic modeling control uses the development of Coulomb's law of sliding friction, but for non-equilibrium conditions. The difference between two opposing forces on a body results in a momentum change of that body:

$$\frac{d(mv)}{dt} = mg\sin\theta - mg\,\mu\cos\theta. \tag{3.5}$$

The mass of the moving pyroclastic flow is constantly decreasing through deposition during emplacement. The mass flux is undoubtably a complex nonlinear function which need not be considered in this flow model. Dividing through by mass $m$ gives

$$a = \frac{dv}{dt} = g\,(\sin\theta - \mu\cos\theta) \tag{3.6}$$

where $a$ is the acceleration of the body. Equation (**3.6**) is the controlling equation for Model 1. In keeping with Heim's interpretation of the fahrböschung in which

$$\mu = \frac{H}{L} = \tan\epsilon, \tag{3.7}$$

$\mu$ is the coefficient of total friction, including internal and basal friction, and it represents the average rate of energy dissipation during pyroclastic flow runout. It is *not* a coefficient of sliding friction per se, because shear occurs within the pyroclastic material during the flow. If sliding is a component of the total friction (e.g., for conditions under which the flow is erosive), then it is implicitly accounted for in $\mu$.

The model structure supporting the controlling equation is the same for all three models. Input data are the $(x,y)$ coordinates of the topographic profile traversed by the particular flow unit and the required frictional resistance parameter(s). Each $(x,y)$ pair is a

calculation point for the model (fig. 3.3). The slope in radians of the topographic segment between the calculation points is determined trigonometrically.

Next, the model-controlling equation calculates the acceleration of the body at point $(x_{i+1}, y_{i+1})$. The acceleration at this point is a function of the slope of the topographic segment and the frictional resistance parameters. The calculation of velocity $v_{i+1}$ is from the equations of motion in a straight line from elementary physics (Sears et al. 1982), derived here: acceleration $a$ is the first derivative with respect to time of velocity $v$:

$$a = \frac{dv}{dt}.$$

Integrating with respect to time gives $v$:

$$v = at + C.$$

At $t = 0$, $v$ is the initial velocity $v_0$, so

$$v = \frac{dx}{dt} = v_0 + at. \tag{3.7}$$

Next, equation (3.7) is integrated with respect to time to find $x$,

$$x = v_0 t + \frac{1}{2}at^2 + C'.$$

At $t = 0$, $x$ is the initial position $x_0$, so

$$x = x_0 + v_0 t + \frac{1}{2}at^2. \tag{3.8}$$

What is required for the modeling purposes is an expression for velocity without time as a variable, because time is unknown for the Mt. St. Augustine pyroclastic flows. Rearranging

equation (3.7) gives

$$t = (\frac{v - v_0}{a}) \tag{3.9}$$

which is then substituted into equation (3.8) resulting in

$$x = x_0 + v_0 \left(\frac{v - v_0}{a}\right) + \frac{1}{2}a \left(\frac{v - v_0}{a}\right)^2.$$

Simplifying and solving for $v$ gives

$$v = \left[{v_0}^2 - 2a(x - x_0)\right]^{0.5}. \tag{3.10}$$

The velocity at each calculation point is a function of the initial velocity entering the slope segment and the acceleration calculated for it.

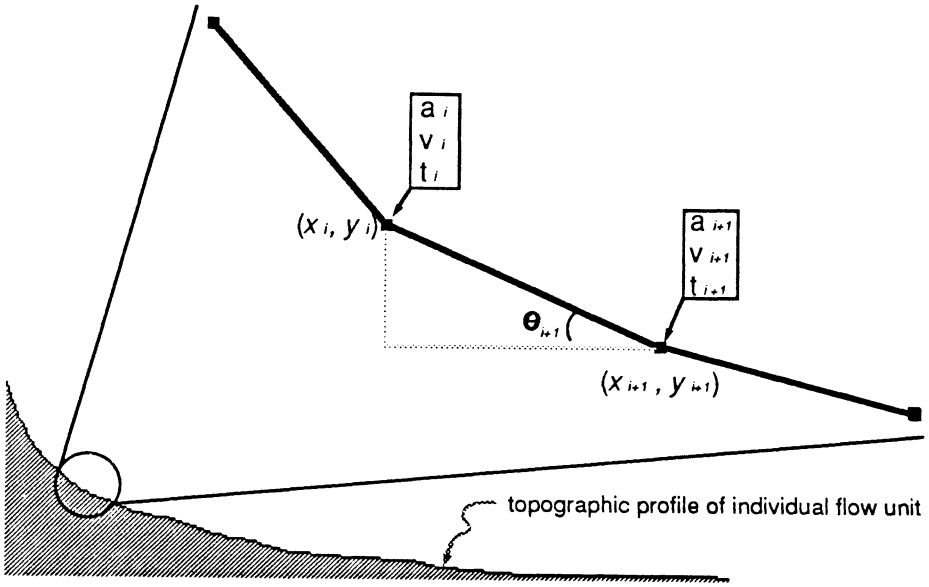


**Fig. 3.3** Flow unit profile showing model calculation points.

FORTRAN IV code for Model 1 is listed in Appendix B. To test the performance of Model 1, it was run for the July 22, 1980 flows at Mt. St. Helens, WA (Hoblitt 1986). The velocities of the flow head for this event were determined from a series of timed photographs as the pumice flow traversed the 5.7-km distance from the amphitheater to the pumice plain. The eruption column reached 300–500 m above the amphitheater vent, corresponding to a total elevation head of 2200–2400 m. Total vertical drop for the deposit is 1100–1300 m, so the frictional coefficient $\mu$ is between 0.19 and 0.23 based solely on the position of the fahrböschung (Hoblitt 1986).

The output for the Model 1 simulation of the July 22 event is shown in fig. 3.4. The frictional coefficient in use is 0.1879 which corresponds to the elevation of the amphitheater floor. To account for the energy imparted to the material falling from 300 m and subsequent momentum loss due to a radical change in direction, a conservative initial velocity of 10 m/s was input to this run. As seen in fig. 3.4, Model 1 consistently overpredicts pyroclastic flow velocity for this event. However, the general behavior of the flow is reproduced. In particular, the model flow accelerates where the slope is steeper than the fahrböschung and decelerates where it is shallower, just as the actual flow was observed to do. The modeled velocities were significantly greater than those observed in 1980, particularly in the flow reach between 3 and 5 km from the vent.

### 3.3 Model 2.

In order to more precisely specify the source of friction within pyroclastic flows, Model 2 incorporates a velocity-proportional fluid resistance term in its controlling equation. As in Model 1, the momentum change is determined by the magnitude of the driving and braking

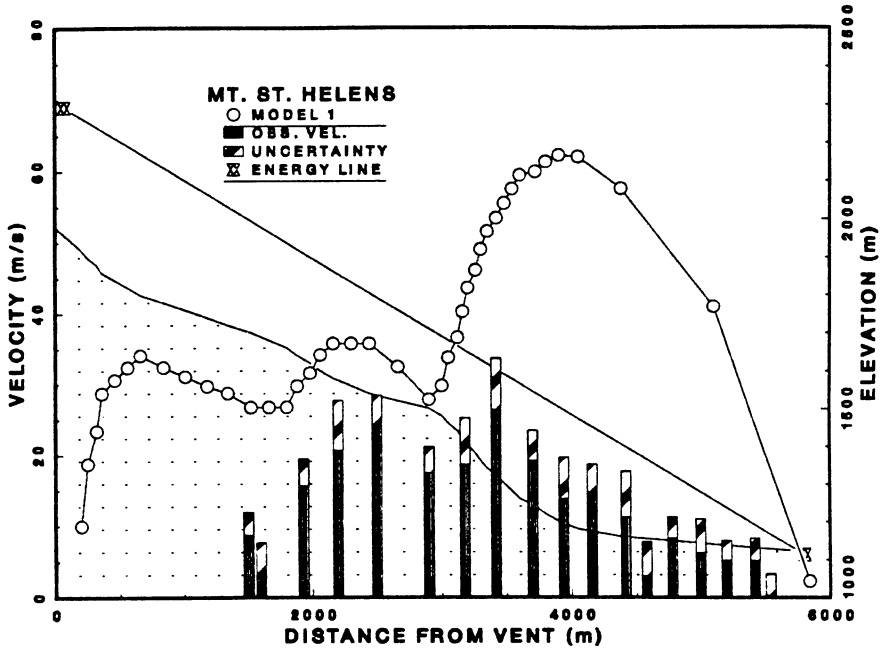


**Fig. 3.4** Comparison of Model 1 output with field data of pyroclastic flow velocity. The pumiceous pyroclastic flow of July 22, 1980 at Mt. St. Helens was closely observed by Hoblitt (1986). The fahrböschung $\epsilon$ drawn here is 12°, which connects the mean of the eruption column height estimates of Hoblitt with the terminus of the pumice deposit. Observed velocities were obtained from a series of timed photographs of the flow head; striped bars represent uncertainty in the estimates. Note how the flow decelerates as the slope of the topographic profile (in background) is less than $\epsilon$, a fact confirmed by Model 1.

forces:

$$\frac{d(mv)}{dt} = mg\sin\theta - Rv_0, \tag{3.11}$$

where $R$ is a fluid resistance term in units of kg/s and $v_0$ is initial velocity for each calculation point (i.e., if in fig. 3.3 the model is currently calculating for point position $i+1$, the initial velocity will be $v_i$). Dividing equation (3.11) through by $m$ gives the controlling equation for Model 2,

$$a = g\sin\theta - R'v_0, \tag{3.12}$$

where $R'$ is merely another form of the fluid resistance term having units of $s^{-1}$. It may be

easier to visualize $R'$ as a kind of "kinetic energy flux" term in which frictional resistance is implicit. The true nature of energy dissipation described by $R'$ is unknown without experimentation and complex numerical analysis. However, an effective form of $R'$ can be obtained through dimensional analysis and calibration with a known data set.

The dimensional analysis begins with a general understanding of the fluid flow situation. Field data at Mt. St. Augustine and elsewhere indicate that pyroclastic flows are characterized by Bingham rheology and have discrete yield strength and Bingham viscosity. These properties offer resistance to continued motion, and by this resistance, kinetic energy is dissipated. It is assumed that a functional relationship therefore exists between the physical quantities yield strength $K$, Bingham viscosity $\eta_b$, flow velocity $v$, and "kinetic energy flux" $R'$. These four quantities can be arranged into a single dimensionless parameter by using the Buckingham $\Pi$ theorem (Streeter and Wylie 1985). This theorem proves that in a problem involving $n$ physical quantities in which there are $m$ fundamental dimensions, $(n - m)$ independent parameters (the so-called $\Pi$ parameters) can be formed. For the problem at hand, there are four physical quantities ($K$, $\eta_b$, $v$, $R'$) and three fundamental dimensions (mass $M$, length $L$, and time $T$), so one $\Pi$ parameter can be formed. The complete procedure for determining $\Pi$ using the Buckingham $\Pi$ theorem is given in Appendix C.

The dimensional analysis in Appendix C yields the dimensionless functional relationship

$$\Pi = \frac{\eta_b R' v^0}{K} = \frac{\eta_b R'}{K}, \tag{3.13}$$

which can be solved for $R'$, giving the useful result

$$R' = C\frac{K}{\eta_b}. \tag{3.14}$$

$C$ is a constant that can only be evaluated through experimentation. Substituting equa-

tion (3.14) into equation (**3.12**) yields

$$a = g \sin\theta - C\frac{K}{\eta_b} v_0. \tag{3.15}$$

The "experiment" by which $C$ is evaluated was run on July 22, 1980 at Mt. St. Helens. From the pyroclastic flow velocities reported for this event in Hoblitt (1986), equation (3.10) is solved for $a$, and equation (3.15) is then solved for $C$. The rheological parameters used in equation (3.15) are taken from Wilson and Head (1981). They report yield strengths for the July 22 pumice flow between 400 and 1100 Pa, calculated using equation (2.8). For the observed pumice flow unit at Mt. St. Augustine, L/pf, $K$ is 1200 Pa, so their upper value of 1100 Pa is selected as representative. The authors determined apparent viscosity for the pumice flow deposit using a penetrometer, and report values between 30 and $2 \times 10^3$ Pa s. The value of 79 Pa s calculated for unit L/pf at Mt. St. Augustine is within their range and is selected as representative.

The protocol for calculating $C$ was encoded and run for the section of runout bounded by Hoblitt's field locations (between 1520 and 5540 m from the vent). For each increment of slope (see fig. 3.3) within this section, the observed velocity is the input and $C$ is the calculated result. The mean value of $C$ is 1.44; standard deviation from the mean is 0.68, indicating a large amount of scatter in the results.

With Model 2 calibrated and encoded (FORTRAN IV code is listed in Appendix D), its performance is tested using the Mt. St. Helens data set. The controlling parameters are specified above, and output is plotted in fig. 3.5.

In general, Model 2 reproduces the observed velocities for the July 22, 1980 pumice flow at Mt. St. Helens more accurately than does Model 1. Between 2000 and 3000 m from the vent, Model 2 tends to underestimate flow velocity, and at the pumice flow terminus, a non-zero velocity is predicted. At both of these locations, topographic slope is low, but flow is sustained because of the decreasing magnitude of the braking force (the second term in

equation (3.15)). As the initial velocity $v_0$ at each calculation point becomes lower, so does the braking force, and as $v_0$ becomes higher, flow resistance is proportionally increased. Model 2 is thus analogous to Newton's law of viscosity (equation (2.3)), in that frictional resistance is proportional to deformation rate. The assumption of non-Newtonian (i.e., Bingham) rheology is implicitly accounted for by the use of $K$ in the energy flux term, but the model is insensitive to the yield criterion as evidenced by the non-zero velocity at the flow terminus.

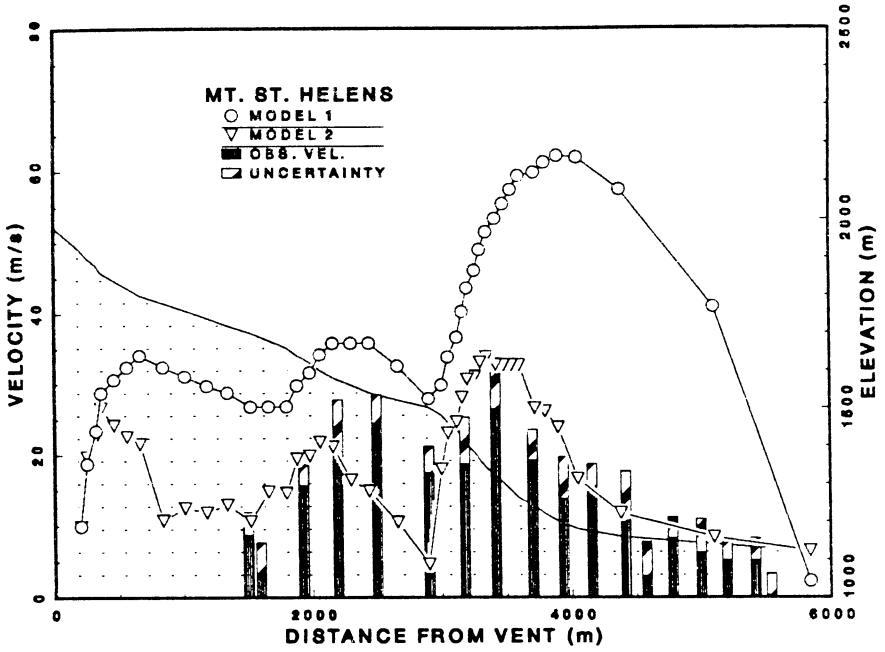


**Fig. 3.5** Comparison of Model 2 results with Model 1 and the observed data at Mt. St. Helens. The fit of Model 2 to Hoblitt's (1986) observed velocities is an improvement over Model 1.

### 3.4 Model 3.

Whereas Model 2 is an attempt to identify the specific source of friction in a pyroclastic flow through the use of hypothetically-constructed resistance term ($R'$), Model 3 defines

the resistance term specifically using the expression of Bingham viscosity, equation (2.12). The development begins with the controlling equation of Model 1, equation (**3.6**), repeated here:

$$a = g(\sin\theta - \mu\cos\theta). \tag{**3.6**}$$

Equation (**3.6**) is also the form of the controlling equation for Model 3; the difference is that $\mu$ will be redefined as the coefficient of *Bingham* friction, $\mu_B$. An expression for $\mu_B$ can be obtained by combining the acceleration equation (**3.6**) with the Bingham viscosity equation (2.12), repeated here:

$$\eta_b = \frac{1}{v}\left[\frac{\gamma}{2}\sin\theta(y^2 - {T_c}^2) - K(y - T_c)\right]. \tag{2.12}$$

The first step is to solve equation (**3.6**) for $\sin\theta$:

$$\sin\theta = \frac{a}{g} + \mu_B\cos\theta. \tag{3.16}$$

Note the presence of $\mu_B$ in equation (3.16). Next, (3.16) is substituted into equation (2.12) for $\sin\theta$, resulting in:

$$\eta_b = \frac{1}{v}\left[\frac{\gamma}{2}(\frac{a}{g} + \mu_B\cos\theta(y^2 - {T_c}^2) - K(y - T_c)\right]. \tag{3.17}$$

Solving for $\mu_B$ gives

$$\mu_B = \frac{1}{\cos\theta}\left[\frac{2}{\gamma(y^2 - {T_c}^2)}[\eta_b v_0 + K(y - T_c)] - \frac{a_0}{g}\right] \tag{3.18}$$

which is used in

$$a = g(\sin\theta - \mu_B\cos\theta). \tag{**3.19**}$$

Equation (**3.19**) is the controlling equation for Model 3. The subscripts 0 for $a$ and $v$ in equation (3.18) indicate that these values were calculated at the previous point.

For the July 22, 1980 pumice flow at Mt. St. Helens, Model 3 is able to reproduce Hoblitt's observed velocities exactly when small flow-depth changes are used as input (fig. 3.6). The rheological parameters used for this run are identical to those used for Model 2 with the addition that $T_c$ is 0.8 m (Wilson and Head 1981). The simulated depths plotted in the figure were arrived at by trial in order to duplicate the observed velocities. Up to the point where the flow reaches the pumice plain (at a distance of 4000 m from the vent), flow depths had to be modulated by only about 1 m. The sensitivity of Model 3 to slight changes in flow depth relates to the role that flow weight (i.e., the weight of material having depth $y$) plays as the driving force. Changes in flow thickness are physically reasonable, as an inverse correlation probably exists between flow depth and topographic slope. Some thickening of flows may occur when they decelerate, while acceleration probably results in attenuation and thinning. Testing the first-order regression of depth on topographic slope for the Mt. St. Augustine flow deposits reveals a significant relationship at $\alpha = 0.10$, but with poor correlation ($R^2 = 0.16$).

The extreme depths used for flow on the pumice plain (at distances greater than 4000 m from the vent) suggest that strict Bingham behavior may not accurately model flow mechanisms on this shallow slope. Another likely possibility is that the pumice flow itself was non-uniform, and that additional momentum was supplied to the flow (and therefore the flow head seen by the observer) by a subsequent pulse of pyroclastic material which was discharged some time after the initial pumice-fountaining event. This pulsed influx of mass would have initiated a wave propagating down the length of the moving flow, which, upon reaching the flow head, would have caused it to accelerate. The sudden acceleration of the pumice flow at a distance of about 4700 m observed by Hoblitt may be a result of just such a wave arriving at the flow head and boosting its momentum.

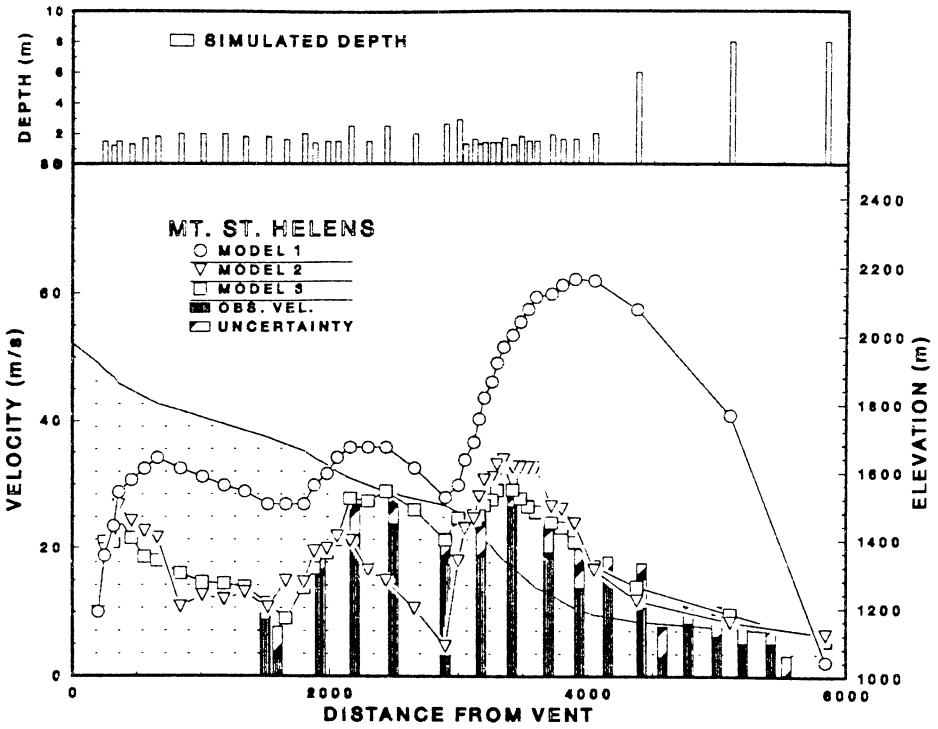


**Fig. 3.6** Comparison of Model 3 results with Models 1 and 2 and observed velocities at Mt. St. Helens. Depths plotted on upper graph enable Model 3 to reproduce the observed velocities exactly. Extreme depths used at the last three calculation points are needed because of probable non-uniformity of flow of the pumice flow at this location.

The two-dimensional nature of Model 3 requires an extra input parameter in order to reproduce the velocity of a pyroclastic flow. The depth $y$ of the moving flow must be known at each calculation point. In lieu of observational data for flow depths at Mt. St. Augustine, simulated flow depths were used. For each flow unit, simulated flow depths are entered interactively into the program (see Appendix E), and they are constrained by existing field data for channel depths vs. vent distance where available (see Table 2.1). This represents a simplification, as it is likely that transient changes in yield strength, density, viscosity, critical thickness, or other factors may play a role in controlling flow velocities.

### 3.5 Results of Modeling the 1986 Pyroclastic Flows at Mt. St. Augustine.

The three models developed to retrodict the kinematics of the 1986 pyroclastic flows at Mt. St. Augustine are based on the balance between potential and kinetic energies and internal frictional work. The pyroclastic flow is modeled as a discrete sediment package subject to acceleration or deceleration in response to changes in the relative magnitudes of the opposing forces of frictional energy dissipation and gravity.

The frictional mechanisms differ principally in the three models. In Model 1, momentum is dissipated by way of a coefficient of average energy loss defined from the fahrböschung of the deposit. In Model 2, momentum is dissipated according to a velocity-proportional fluid resistance force; the resistance parameter is a hypothetical construct incorporating the apparent yield strength and Bingham viscosity calculated for each flow unit. In Model 3, the coefficient of average energy loss of Model 1 is redefined as a coefficient of Bingham friction developed from the expression of Bingham viscosity. A knowledge of the physical and rheological properties of the flows is required for the use of Model 3. The three models were tested using the observational data from the July 22, 1980 pumiceous pyroclastic flow at Mt. St. Helens. The general results are that Model 1 consistently overpredicted the observed flow velocities, Model 2 predicted values much closer to those observed, and Model 3 reproduced the observed velocities exactly when the proper simulated flow depths were used as input.

At Mt. St. Augustine, ten lithic block and ash flow units and one pumiceous flow unit were modeled by the above methods to estimate their velocities of emplacement. The model output is compared to: (1) reconstructions of flow velocities based on the superelevation of levee deposits, (2) reconstructions based on the runup of ash cloud deposits, and (3) an observed velocity of 40 m/s at a distance of 1500 m from the vent (J. Kienle, personal communication 1986) (fig. 3.7).

During the third eruptive period of 1986, a UAFGI field party observed several small-scale lithic block and ash flows at close range (Kienle 1986). The observed velocity was calculated by timing the transit of the flow head between two reference boulders adjacent to the flow and dividing by the paced distance between them. The flow deposit for which this observation was made is not one of the modeled flow units in this study; however, its value of 40 m/s is included as a reference velocity for all modeled flow units exceeding 1500 m in runout.

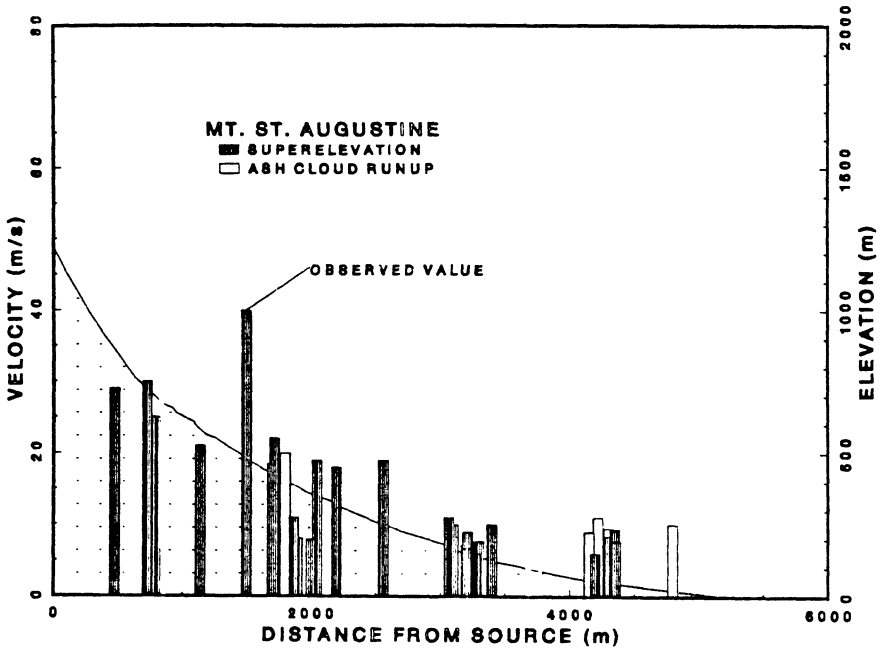


**Fig. 3.7** Compilation plot of all field-reconstructed velocities.

Pyroclastic flow velocity reconstructed from superelevation was discussed in Chapter 2; another method for velocity estimation is from the runup of an ash cloud deposit. It is assumed that the overriding ash cloud is a fully turbulent mixture of coarse and fine ash, magmatic gases, and hot air convecting from the basal underflow. It is also assumed that the mean velocity of the ash cloud in the $x$-direction is the same as that of the basal underflow,

and that the ash cloud is not subject to the frictional mechanisms opposing the continued motion of the block and ash flow. When a pyroclastic flow encounters an obstacle such as a debris avalanche hummock or a large accretionary levee complex, the basal underflow is deflected away, and the ash cloud decouples and runs up the obstruction. The kinetic energy of the ash cloud is quickly exhausted by the elevation gain during runup, resulting in deposition of layer 3 of Sparks et al. (1973). Ash cloud deposits often display plane beds and cross beds and are best preserved on the flanks of an obstruction.

The expression relating flow velocity to runup height is known as Torricelli's theorem and is derived from Bernoulli's equation for flow energy per unit weight along a streamline (Streeter and Wylie 1985). Torricelli's theorem states that the elevation head achieved by a fluid flowing up onto an obstruction is equal to the fluid's velocity head at the base of the obstruction,

$$H = \frac{v^2}{2g}, \tag{3.20}$$

where $H$ is the vertical height of runup (numerically equal to elevation head). Solving for velocity,

$$v = \sqrt{2gH}. \tag{3.21}$$

Table 3.1 contains the field data used in the runup velocity estimates.

Ash cloud velocities are included in fig. 3.7 as additional reference values for probable pyroclastic flow velocity at the indicated distances from vent. It should be kept in mind that the velocities plotted in fig. 3.7 are reconstructed from at least eleven separate pyroclastic flow units.

Output from the three models is plotted with the superelevation-derived velocities for the eleven studied flow units in figs. 3.8 to 3.13. Model parameters are listed in the figure captions and Table 3.2.

**Table 3.1. Ash Cloud Runup Field Data.**

| Station number | Distance from source (m) | $H$ (m) | $v$ (m/s) | obstacle |
|---|---|---|---|---|
| ac6 | 1700 | 6.7 | 11.5 | 1883 lava flow |
| ac5 | 1800 | 20 | 20 | " |
| ac3 | 4150 | 4.0 | 9 | levee complex |
| ac2 | 4220 | 6.1 | 11 | " |
| ac1 | 4300 | 4.6 | 9.5 | debris avalanche hummock |
| ac4 | 4830 | 5.2 | 10.1 | " |

Model 1 predicts the highest pyroclastic flow velocities of the three models. For all of the flow units, the frictional coefficient $\mu$ is defined as the tangent of the fahrböschung $\epsilon$ and is interpreted as a constant rate of total energy loss. Where the slope is steep, the braking force given by $\mu \cos\theta$ is relatively ineffective, resulting in rapid acceleration. The high velocities are sustained and uniformly dissipated until $v = 0$ at the terminus of the deposit. All of the velocity-distance profiles have the same general shape except for the smaller, late-stage block and ash flows (units 17, 18, 5, and 7). The smaller flows have lower velocities and momentum according to Model 1, so the effect of irregular topography is greater on them. For units 18, 5, and 7, the flows decelerate greatly at runout = 770 m because of a decrease in slope from 31° to 14°. Larger flows such as unit 19 have higher volume, mass, and runout, and have a lower fahrböschung and frictional coefficient. These characteristics working together tend to damp out topography-induced momentum loss in the larger flows. The path traversed by unit 19 is nearly identical to that for units 18, 5, and 7, and at runout = 770 m (fig. 3.13), only a slight deceleration results from the the slope reduction. The maximum velocities near 80 m/s predicted for the larger pyroclastic flows (figs. 3.8 to 3.10) greatly exceed Kienle's observed value, as well as the values reconstructed from superelevation and ash cloud runup and velocities observed by Stith et al. (1977) for a pyroclastic flow generated during the 1976 eruption of Mt. St. Augustine. Stith et al.

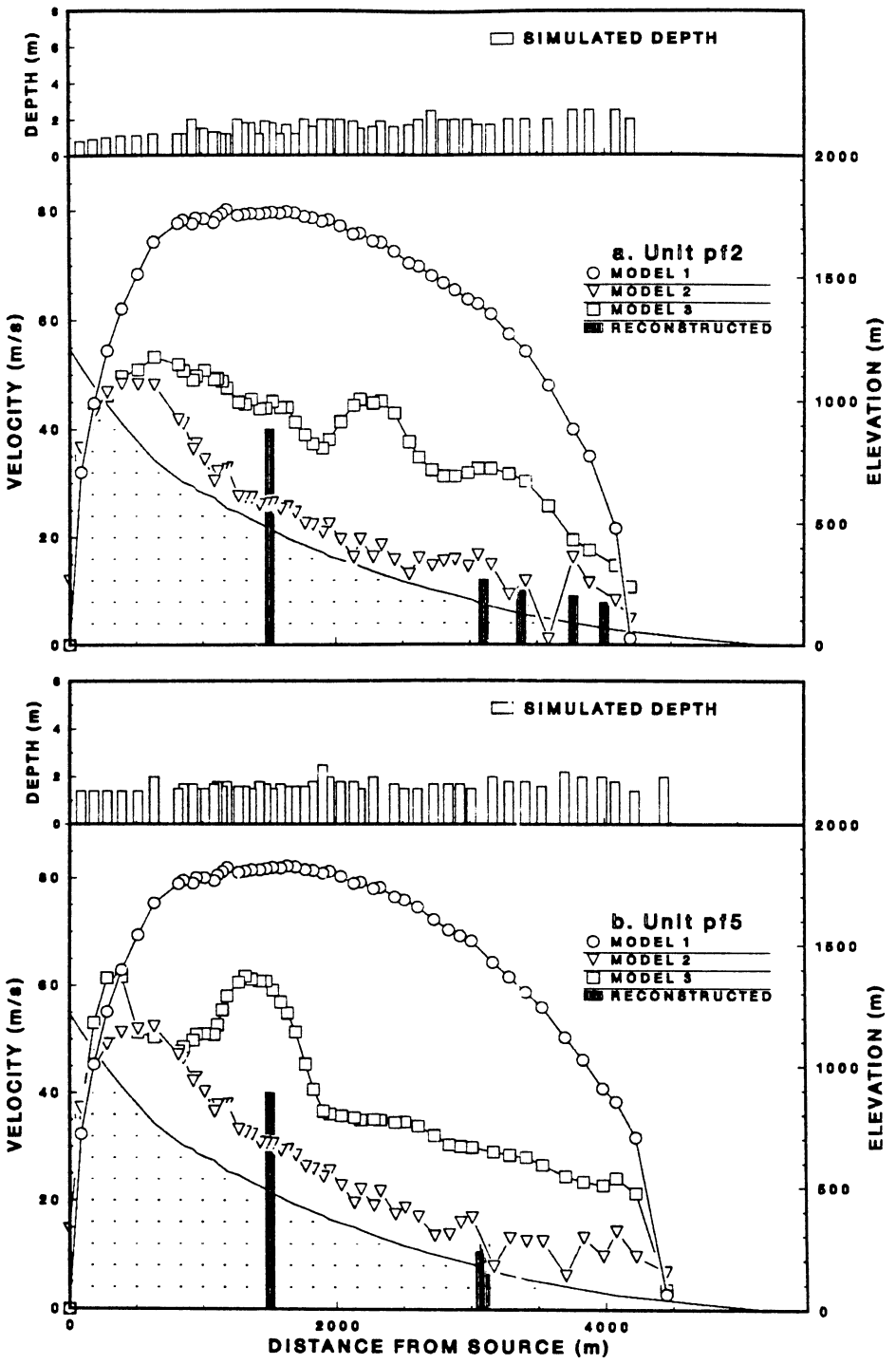


**Fig. 3.8** Modeling results for units pf2 and pf5; 1986 block and ash flow deposits at Mt. St. Augustine. (a.) Unit pf2. Model 1: $\mu = 0.278$. Model 2: $R' = 0.11$. Model 3: $K = 1400$ Pa, $\eta_b = 64$ Pa s, $T_c = 0.7$ m, $\overline{y} = 1.6$ m. Total runout: 4190 m. (b.) Unit pf5. Model 1: $\mu = 0.265$. Model 2: $R' = 0.10$. Model 3: $K = 1700$ Pa, $\eta_b = 33$ Pa s, $T_c = 1.3$ m, $\overline{y} = 1.6$ m. Total runout: 4450 m.

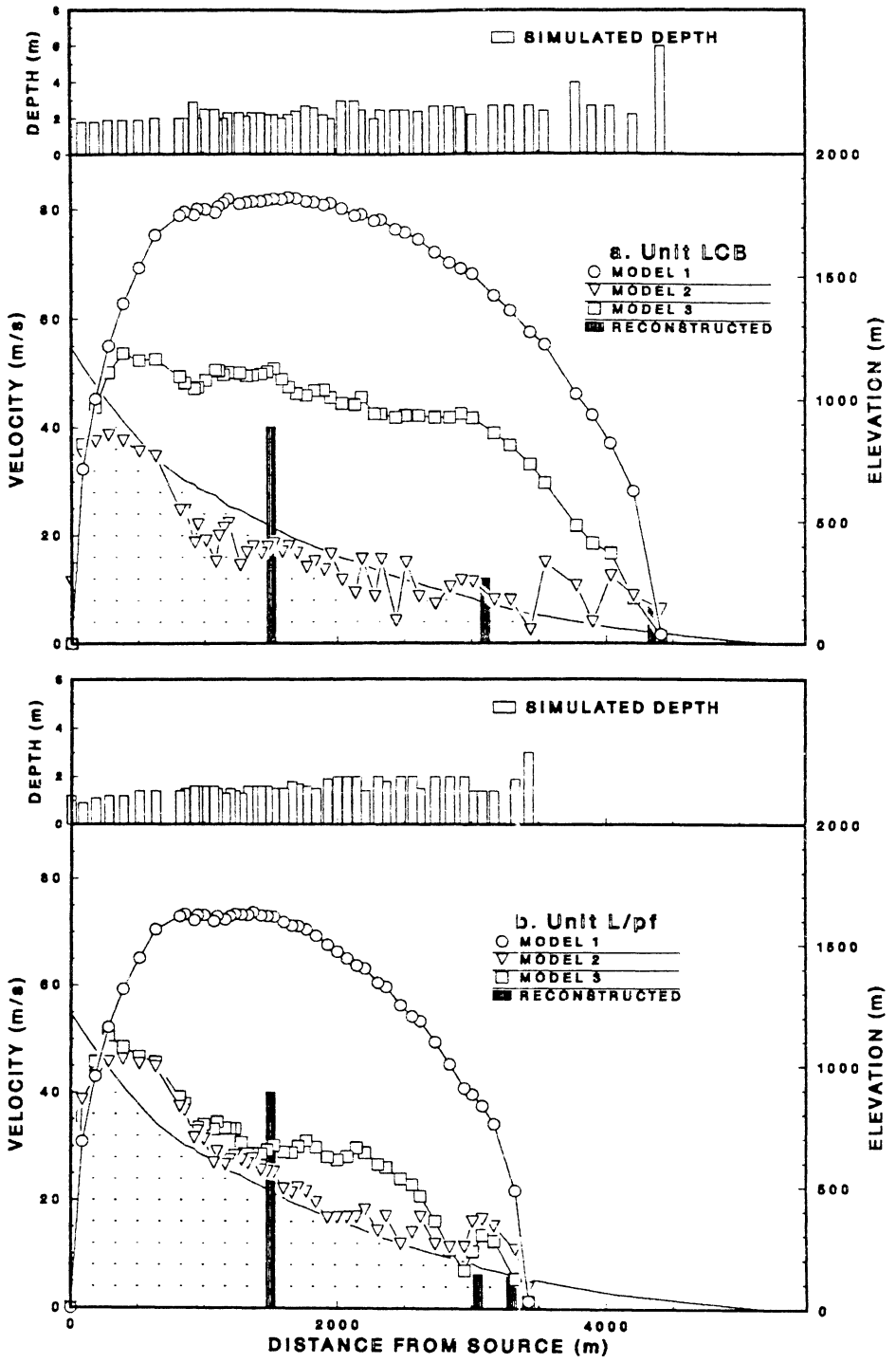


**Fig. 3.9** Modeling results for units LCB and L/pf; 1986 block and ash flow and pumice flow deposits, respectively, at Mt. St. Augustine. (a.) Unit LCB. Model 1: $\mu = 0.266$. Model 2: $R' = 0.15$. Model 3: $K = 1700$ Pa, $\eta_b = 76$ Pa s, $T_c = 1.7$ m, $\overline{y} = 2.4$ m. Total runout: 4410 m. (b.) Unit L/pf (pumice flow). Model 1: $\mu = 0.323$. Model 2: $R' = 0.12$. Model 3: $K = 1200$ Pa, $\eta_b = 79$ Pa s, $T_c = 0.8$ m, $\overline{y} = 1.6$ m. Total runout: 3430 m.

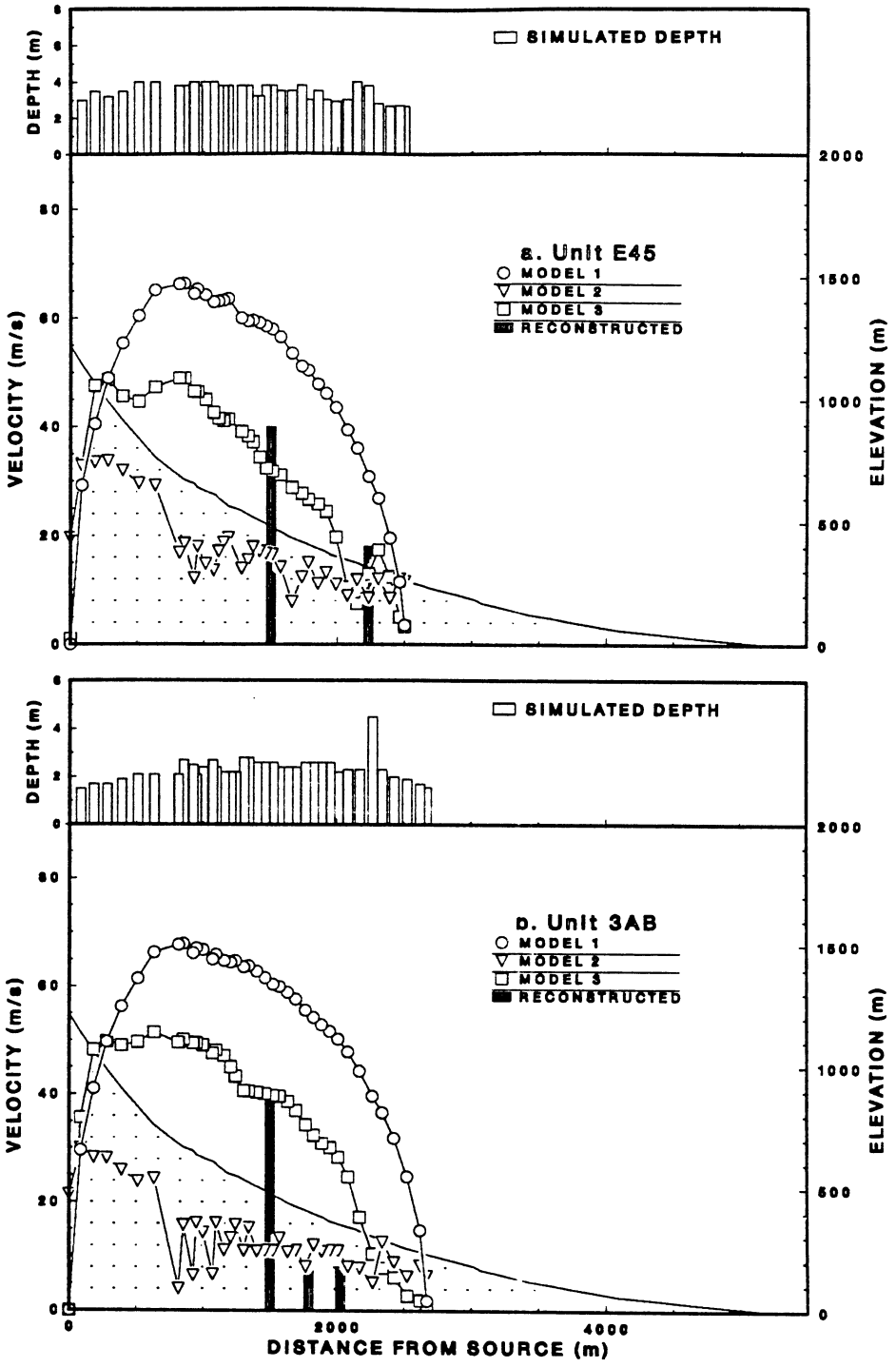


**Fig. 3.10** Modeling results for units E45 and 3AB; 1986 block and ash flow deposits at Mt. St. Augustine. (a.) Unit E45. Model 1: $\mu = 0.381$. Model 2: $R' = 0.18$. Model 3: $K = 5900$ Pa, $\eta_b = 310$ Pa s, $T_c = 2.0$ m, $\overline{y} = 3.4$ m. Total runout: 2500 m. (b.) Unit 3AB. Model 1: $\mu = 0.368$. Model 2: $R' = 0.21$. Model 3: $K = 2300$ Pa, $\eta_b = 190$ Pa s, $T_c = 1.3$ m, $\overline{y} = 2.3$ m. Total runout: 2670 m.

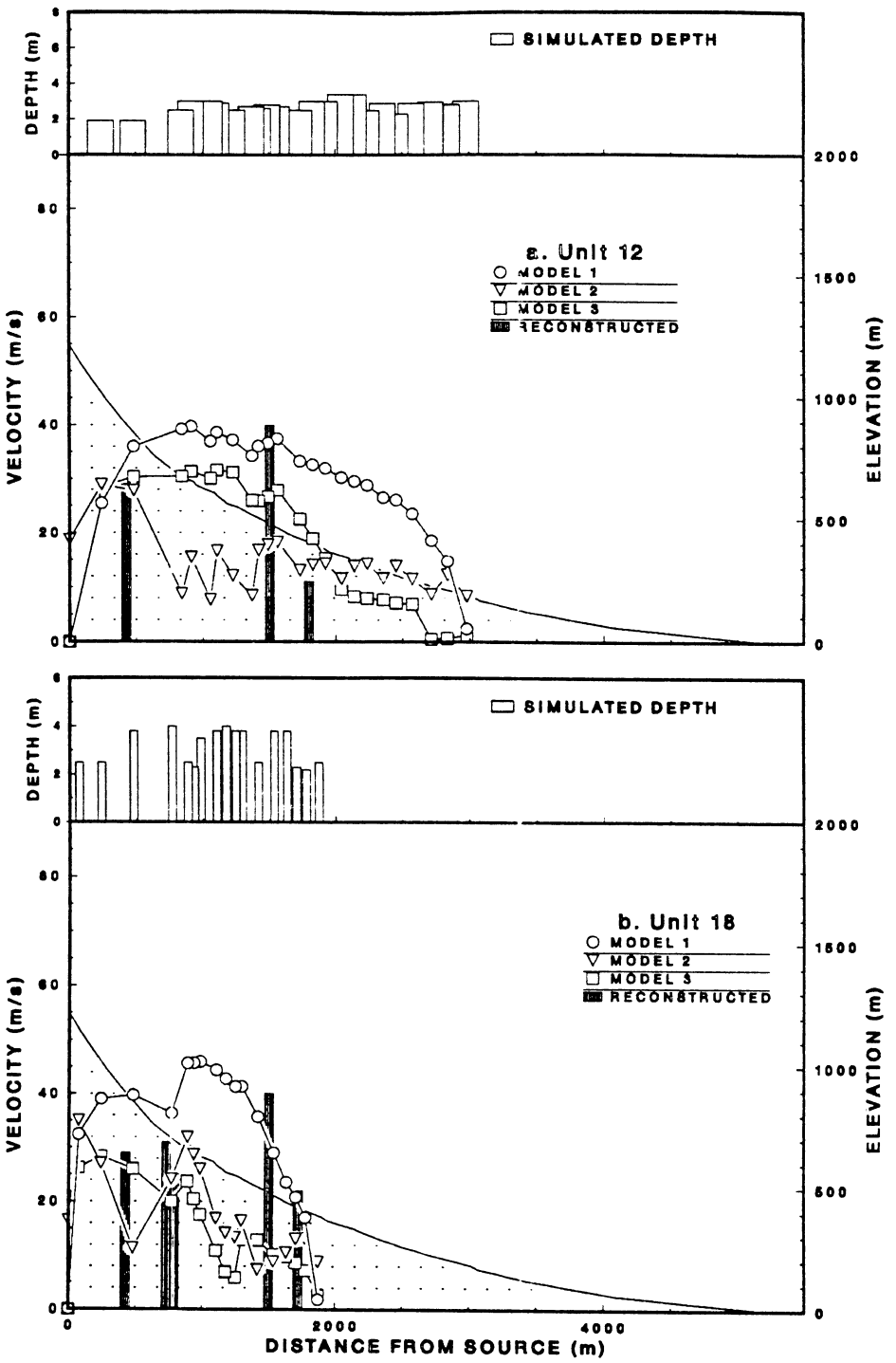


**Fig. 3.11** Modeling results for units 12 and 18; 1986 late-stage block and ash flow deposits at Mt. St. Augustine. (a.) Unit 12. Model 1: $\mu = 0.179$. Model 2: $R' = 0.11$. Model 3: $K = 4000$ Pa, $\eta_b = 130$ Pa s, $T_c = 1.5$ m, $\overline{y} = 2.6$ m. Total runout: 2980 m. (b.) Unit 18. Model 1: $\mu = 0.309$. Model 2: $R' = 0.15$. Model 3: $K = 2900$ Pa, $\eta_b = 400$ Pa s, $T_c = 0.8$ m, $\overline{y} = 3.0$ m. Total runout: 1870 m.

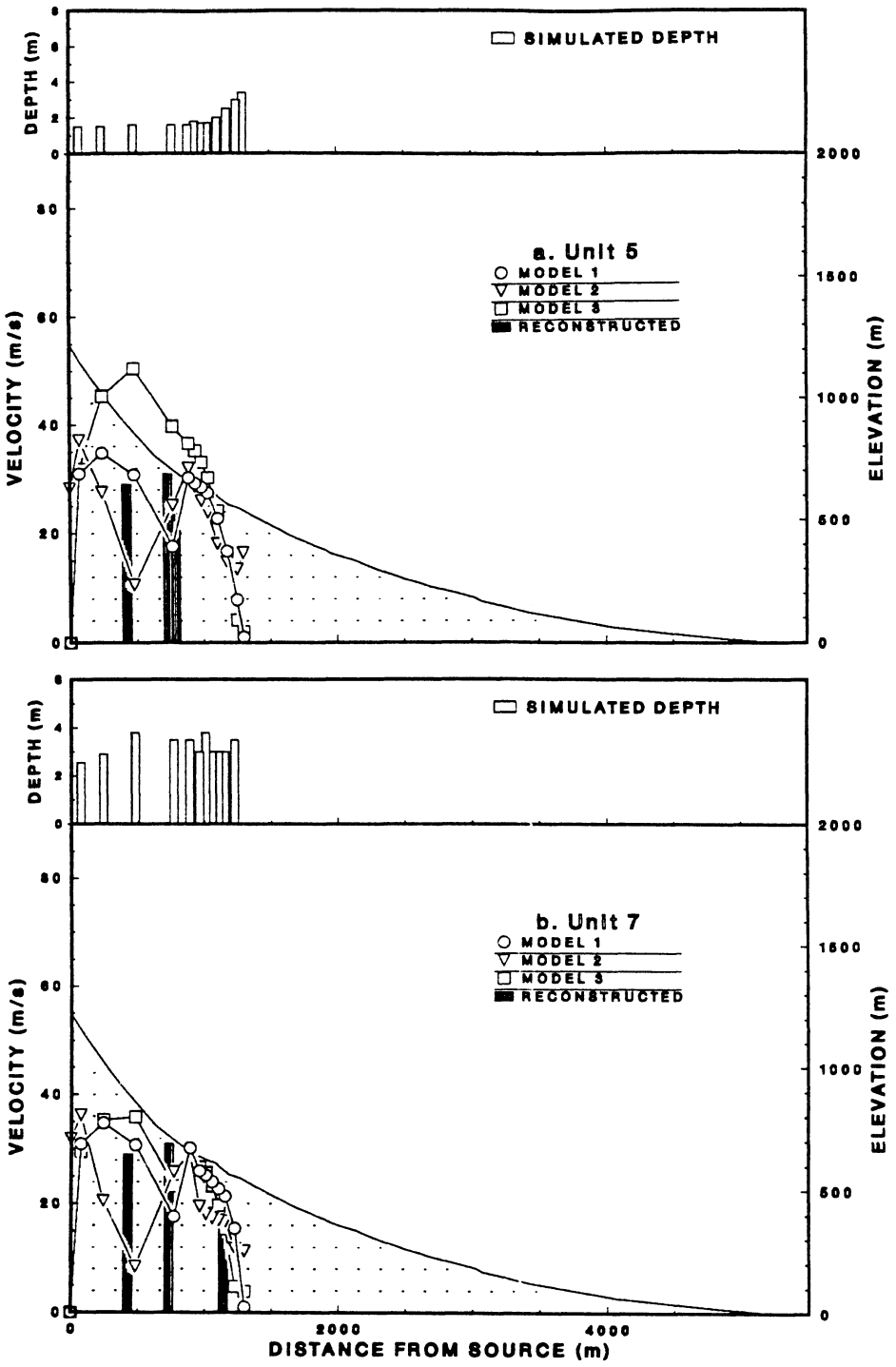


**Fig. 3.12** Modeling results for units 5 and 7; 1986 late-stage block and ash flow deposits at Mt. St. Augustine. (a.) Unit 5. Model 1: $\mu = 0.377$. Model 2: $R' = 0.19$. Model 3: $K = 5800$ Pa, $\eta_b = 30$ Pa s, $T_c = 1.4$ m, $\overline{y} = 1.8$ m. Total runout: 1300 m. (b.) Unit 7. Model 1: $\mu = 0.377$. Model 2: $R' = 0.18$. Model 3: $K = 6300$ Pa, $\eta_b = 230$ Pa s, $T_c = 1.5$ m, $\overline{y} = 2.7$ m. Total runout: 1300 m.

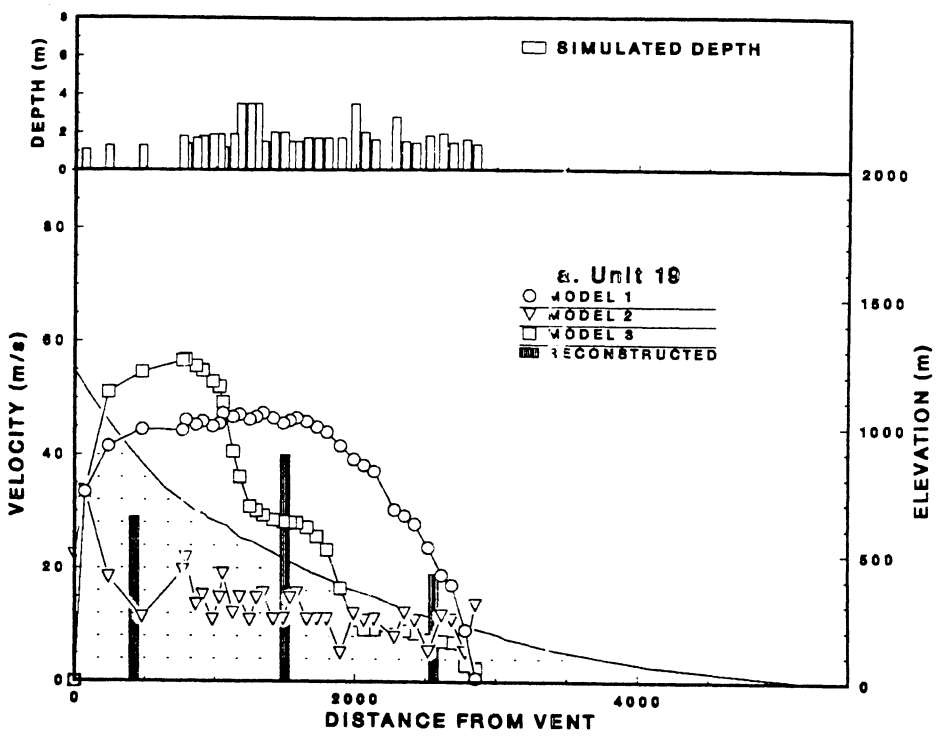


**Fig. 3.13** Modeling results for unit 19; 1986 late-stage block and ash flow deposit at Mt. St. Augustine. Model 1: $\mu = 0.267$. Model 2: $R' = 0.18$. Model 3: $K = 3300$ Pa, $\eta_b = 55$ Pa s, $T_c = 1.0$ m, $\overline{y} = 1.8$ m. Total runout: 2860 m.

## Table 3.2. Modeling Parameters.

| Station number | Total Runout (m) | Model 1: $\mu$ | Model 2: $R'$ ($s^{-1}$) | Model 3: $K$ ($\times 10^3$ Pa) | $\eta_b$ ($\times 10^1$ Pa s) | $T_c$ (m) | $\overline{y}$ (m) |
|---|---|---|---|---|---|---|---|
| pf2 | 4190 | 0.278 | 0.11 | 1.4 | 6.4 | 0.7 | 1.6 |
| pf5 | 4450 | 0.265 | 0.10 | 1.7 | 3.3 | 1.3 | 1.6 |
| LCB | 4410 | 0.266 | 0.15 | 1.7 | 7.6 | 1.7 | 2.4 |
| L/pf | 3430 | 0.323 | 0.12 | 1.2 | 7.9 | 0.8 | 1.6 |
| E45 | 2500 | 0.381 | 0.18 | 5.9 | 31 | 2.0 | 3.4 |
| 3AB | 2670 | 0.368 | 0.21 | 2.3 | 19 | 1.3 | 2.3 |
| 12 | 2980 | 0.179 | 0.11 | 4.0 | 13 | 1.5 | 2.6 |
| 18 | 1870 | 0.309 | 0.15 | 2.9 | 40 | 0.8 | 3.0 |
| 5 | 1300 | 0.377 | 0.19 | 5.8 | 3.0 | 1.4 | 1.8 |
| 7 | 1300 | 0.377 | 0.18 | 6.3 | 23 | 1.5 | 2.7 |
| 19 | 2860 | 0.267 | 0.18 | 3.3 | 5.5 | 1.0 | 1.8 |

(1977) report a maximum velocity of 50 m/s for the pyroclastic flow which reached the sea on the east side of Burr Point.

The sawtooth velocity profile predicted by Model 2 is a result of the dependence of the braking mechanism on the initial velocity. For example, a high $v_0$ produces a high braking force resulting in a lower $v_i$ calculated for the point. The low $v_i$ becomes the low $v_0$ for the next point producing a low braking force and therefore a high $v_i$. This mimics the pulsating nature of pyroclastic flow velocity observed by Kienle (personal communication 1986) for a small-scale block and ash flow at Mt. St. Augustine. Vallance and Rose (1989) document velocity pulsations for experimental pyroclastic flows. They heated volcanic ash from Mt. St. Helens to 600° C and poured it down an inclined plane moistened with water. Velocity pulsations of the flow head resulted from unsteady, non-uniform flow of the fluidized ash. The range of velocity variation predicted by Model 2 overlaps the field-reconstructed values at Mt. St. Augustine better than Model 1.

For Model 3, when flow depth is close to the critical thickness $T_c$ of the material, shear stresses within the flow are close to the yield strength and flow cessation is imminent. When flow depth significantly exceeds critical thickness, the driving force (supplied by the weight of material having depth $y$ on a slope of $\theta$) is counteracted only by Bingham viscosity. Slight depth modulations have a great effect on flow velocity. For unit pf2 (fig. 3.8) at a distance of 2000–2500 m, a depth increase of 0.2 m is enough to increase flow velocity by about 10 m/s. For unit pf5 at a distance of 1100 m a 0.3-m depth increase causes a 15 m/s velocity increase. Model 3 reproduces the effect that an increase in mass, i.e., a depth increase, has on the flow: momentum is increased, which counteracts the velocity-reducing frictional forces. When low depths are input at the steep initial section of runout, accelerations are low, and when high depths are input at the distal end, the flows maintain motion until the location of the observed terminus is reached (see units LCB, L/pf, and 5).

There is no field evidence for the high flow depths at these deposit termini, sugggesting an alternate flow mechanism operating on low slopes.

## CHAPTER 4:

# GRAIN SIZE DISTRIBUTION

### 4.1 Introduction.

At Mt. St. Augustine, the entire 1986 pyroclastic sediment population constitutes a multivariate stratigraphic package. Fig. 1.2 lists the three types of genetically and compositionally distinct deposits: pumice flow deposits, lithic-rich pumice flow deposits, and lithic block and ash flow deposits. In addition, the lithic block and ash flow deposits are composed of at least two and sometimes four separate sublayers (figs. 1.4a and 1.4b); these are the layers 1 through 3 of Sparks et al. (1973). In order to narrow the scope of the granulometry to a more manageable size, the focus of this analysis is only upon layer 2b of the lithic block and ash flow deposits. Layer 2b is interpreted to represent the material which was transported as a plug above the basal shearing zone in a moving flow, and it is the most important sublayer, by volume, of the lithic block and ash flow deposits. It is also representative of the bulk composition of the pyroclastic material.

Reconnaissance surveys of the surface of the lithic block and ash flow deposits at Mt. St. Augustine revealed a tremendous range in grain sizes, spanning six orders of magnitude. Fine ash is $< 10^{-2}$ mm in diameter and the largest blocks can be 10–20 m in diameter. This situation presents the problem of adequate and meaningful sampling of the deposit. Mellors et al. (1988) in their study of small pyroclastic deposits flanking the dome of Mt. St. Helens avoided this problem simply by ignoring clasts larger than some arbitrarily-set size class. However, these clasts probably should not be neglected in sedimentological studies because they are observed in great concentrations, and they have

undoubtedly played a significant role in defining the apparent rheological properties of the moving flows.

Qualitative observations made during field reconnaissance suggested that high concentrations of the largest clasts were found on the proximal reaches of the pyroclastic fan, and that lower concentrations of the largest clasts were found on the distal reaches. One might expect that distal deposits would be better sorted than proximal deposits in the 1986 pyroclastic fan due to the flow evolving with time and distance from its source and the resulting changes in sorting occurring downslope.

### 4.2 Sampling and Analytical Protocol.

Locations of the grain size sampling stations are shown in figs. 1.5 and 1.6. Two sampling techniques were combined to characterize the layer 2b deposits at Mt. St. Augustine. The coarse clast population, arbitrarily defined as clasts greater than or equal to 2 mm intermediate diameter, was sampled using the "grid by number" technique of Kellerhals and Bray (1971). In this method, a 50-m surveying chain is stretched out on the surface of the deposit perpendicular to the flow direction, and at 1-m intervals, the intermediate diameter of the clast underneath the interval is measured. Precision of the chain is 2 mm (hence the population size boundary), and if a clast's diameter exceeds 2 m, it is counted twice. Two traverses are taken so as to keep the number of measurements per sampling station equal to 100. Clast size data from a vertical beach cut (station g28) were collected by suspending a fishnet over the cut and measuring clasts under 100 nodal points.

The matrix population (particles smaller than 2 mm) was sampled for sieve analysis from channel deposits along the line of the grid by number transects. Shallow pits 5–15 cm deep were dug into the channel to expose the top of layer 2b underneath any ash cloud or airfall ash deposits. Roughly one liter of sample was collected from layer 2b per pit. Individual samples were oven-dried at 60° C for one hour, then bulk density of the matrix

population was determined by measuring the static loose volume and mass of the sample. Matrix density values were then averaged for the block and ash flow deposits and used in the rheological and kinematic modeling in Chapters 2 and 3. The sample was poured into a stack of Tyler standard testing sieves having mesh sizes (in mm) of 2.36, 1.18, 0.6, 0.3, 0.15, 0.08, and pan. The stack was agitated on a Rotap machine for only five minutes to reduce the possibility of pulverising fragile vesiculated grains. The retained fractions, exclusive of particles of diameter greater than or equal to 2.36 mm, were weighed for determination of weight per size class on a Mettler triple-beam balance having precision of 0.1 g. Sieves were thoroughly cleaned between samples.

Size classes for both the clast and matrix populations were recorded in mm, then converted into the $\phi$ scale of Krumbein (1938) according to

$$\phi = -\log_2 D, \tag{4.1}$$

where $D$ is the intermediate grain diameter in mm. When the data set is transformed in this way, the populations approach a normal distribution.

Granulometric data for the clast population are in percent frequency by number per size class; data for the matrix population are in percent by weight per size class. In order to characterize the entire range of sediment sizes observed in layer 2b of the pyroclastic flow deposits at Mt. St. Augustine, the number frequency data for the clast population were converted into weight percent form and the two data sets were combined.

Kellerhals and Bray (1971) have demonstrated one-to-one equivalence between percent frequency by number and weight percent data based on geometric and dimensional arguments. The sampling techniques differ by the number of predetermined dimensions of the sample volume. For bulk sampling (matrix population), the volume of the sample is predetermined and independent of the size of the individual grains. For grid sampling (clast population) the volume of the sample is dependent in all three dimensions upon individual

clast sizes, and only the dimensionless grid nodes are predetermined. The weighting factor to equate the raw data from the grid sampling with that of the bulk sampling is proportional to $1/D^3$. To convert the frequency by number data into frequency by weight, the content of each size fraction is multiplied by a weighting factor proportional to $D^3$. Taken together, the weighting factors are equal to one, and the two methods are equivalent.

Kellerhals and Bray also derive conversion factors to equate other types of granulometric sampling techniques, thereby providing a way of meaningfully comparing data sets collected using nonequivalent methods. Appending the converted clast data set to the matrix data set is a valid means of characterising the entire grain size population at Mt. St. Augustine (R. Kellerhals, personal communication, 1991).

Quantitative descriptions of the grain size population were obtained using standard moment statistics (McCammon 1962). The measure of the central tendency of the population/sample distribution curve is the mean $\overline{M}_\phi$, calculated from

$$\overline{M}_\phi = \frac{\sum fm}{n}, \tag{4.2}$$

where $f$ is the weight percent in each size class present, $m$ is the midpoint of each size class, and $n$ is equal to 100 when $f$ is in percent. The measure of the spread around the mean is the standard deviation $\sigma$; in granulometric studies this statistic is referred to as the sorting coefficient $\sigma_\phi$ and is calculated from

$$\sigma_\phi = \sqrt{\frac{\sum f(m - \overline{M}_\phi)^2}{n}}. \tag{4.3}$$

The measure of symmetry of the distribution around the mean is the skewness $Sk_\phi$, given by

$$Sk_\phi = \frac{\sum f(m - \overline{M}_\phi)^3}{n{\sigma_\phi}^3}. \tag{4.4}$$

These techniques are called moment statistics because the calculations involve multiplying a weight in percent by a distance (from the origin of the abscissa to the midpoint of

the size class), analogous to the concept of moments from mechanics. An assumption in use with moment statistics is that the particles within a given size class have diameters with a normal distribution around the midpoint $m$. An advantage of using moment statistics is that, unlike graphically-determined statistics, the entire size class distribution is used in the computations, rather than only a few selected parts (McCammon 1962).

Grain size sampling stations coincide with the flow units from which morphometric data were collected (figs. 1.4, 1.5). The sampling stations were grouped according to their distance from the vent and the field season during which they were collected. The samples collected during the 1986 field season were deposited during the March–April 1986 eruptive period. The samples collected during the 1987 field season were deposited from late-stage block and ash flow activity which occurred sometime after August 1986. All of the samples fall into four groups: 1986 distal, 1986 proximal, late-stage distal, and late-stage proximal. The distance criterion dividing distal groups from proximal ones is selected to be 2200 m from the vent.

### 4.3 Grain Size Distribution of the 1986 Pyroclastic Flow Deposits.

Fig. 4.1a–t contains histograms of all grain size distributions from samples collected from the 1986 Mt. St. Augustine block and ash flow deposits. The average grain size distribution for all samples is shown in fig. 4.1u, and each of the four group average distributions are presented in fig. 4.2a–d. Descriptive statistics for all samples and groups are presented in Table 4.1.

In general, all of the samples display a normal size distibution except for gE3, g28, and g27. Half of the samples display bimodal distribution: gN3, (g)LCB, g3AB, g21, g20, g22, g17, g16, gE45, and gE5. The average distributions of both the 1986 and late-stage proximal groups display bimodal distributions (figs. 4.2b and d). Eight of the sample localities at Mt. St. Augustine show significant lack of grains in the 0 to $-1\,\phi$ size class:

gN3, gN1, gN2, (g)LCB, g3b, g3AB, gE45, and gE5. This list contains the entire 1986 proximal group and none of the late-stage sampling stations.

The greatest intrasample variability in the distribution occurs within the clast fraction. Half of the secondary modes occur in $-8\,\phi$ size class, and the remainder occur in the $-4\,\phi$ to $-7\,\phi$ range. Unimodal distributions tend to be enriched also in the $-8\,\phi$ size class. Size distributions within the matrix fraction are remarkably uniform, in that all samples display decreasing proportions of finer particles from the high around $1\,\phi$. Many of the deposits, from disparate locations on the pyroclastic fan, show enrichment in the tail fraction of the population. The average of all distributions at Mt. St. Augustine (fig. 4.1u) displays three modes ($-7\,\phi$, $-3\,\phi$, and $-1\,\phi$), a relative depletion in the $0\,\phi$ to $-1\,\phi$ size class, enrichment in the matrix fraction, and a uniform recession in the proportion of matrix from a peak at $1\,\phi$.

The histograms show a crude trend of decreasing clast size with distance from the vent, and the largest clasts were observed in the proximal groups. The sample means and sorting coefficients are plotted against distance from vent in fig. 4.3; a slight decrease in grain size and a slight improvement in sorting are apparent from these plots. First-order regressions run for both mean grain size and sorting coefficient on distance from vent are significant at $\alpha = 0.10$, but show poor correlation ($R^2 = 0.38$ and 0.55 respectively). Table 4.1 shows that the distributions are all skewed negatively, i.e., towards the matrix fraction, except for g26. The magnitude of the negative skew is greater for the distal samples than for the proximal samples.

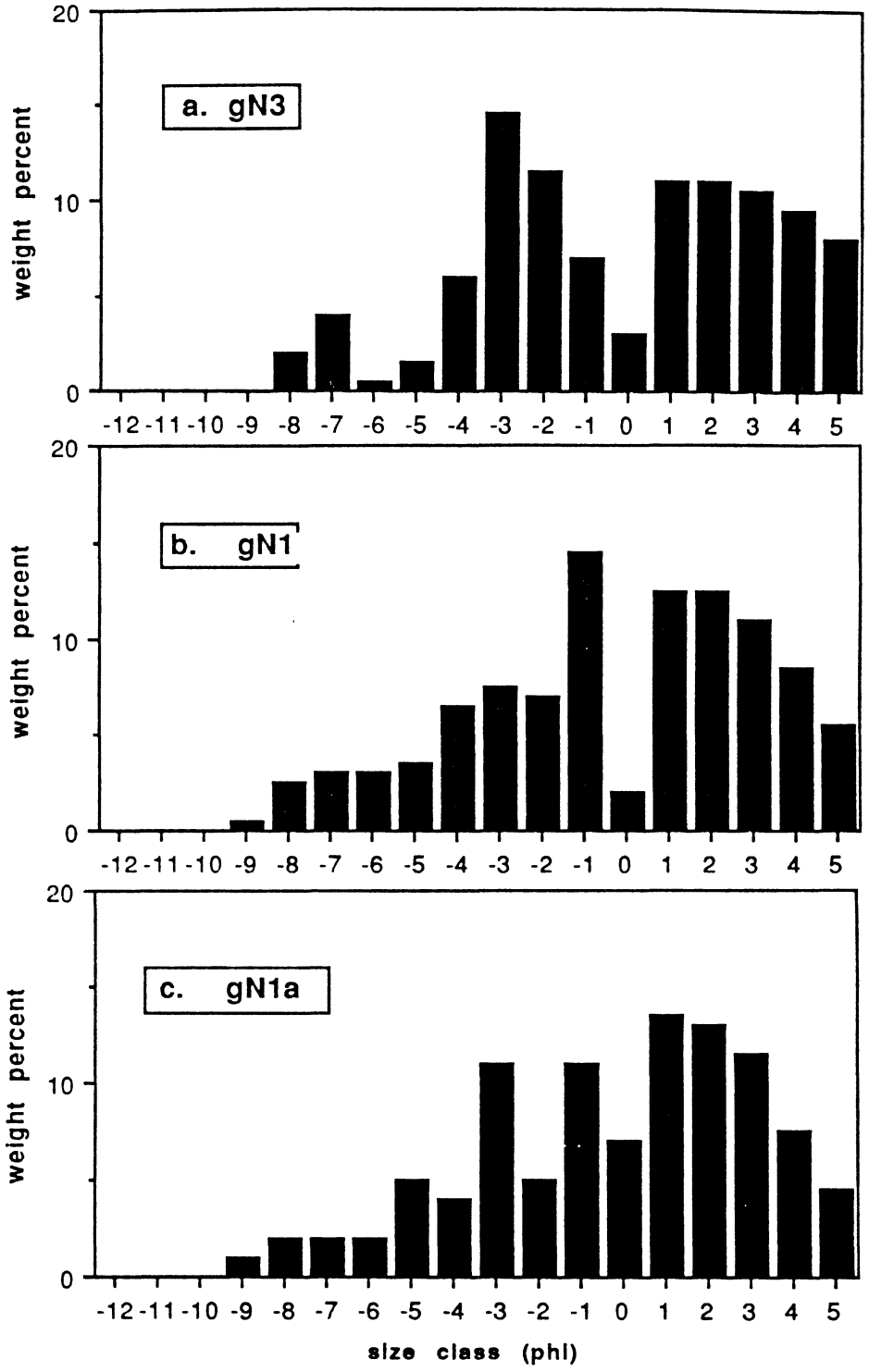


**Fig. 4.1a–c** Grain size distribution histograms for deposits gN3, gN1, and gN1a.

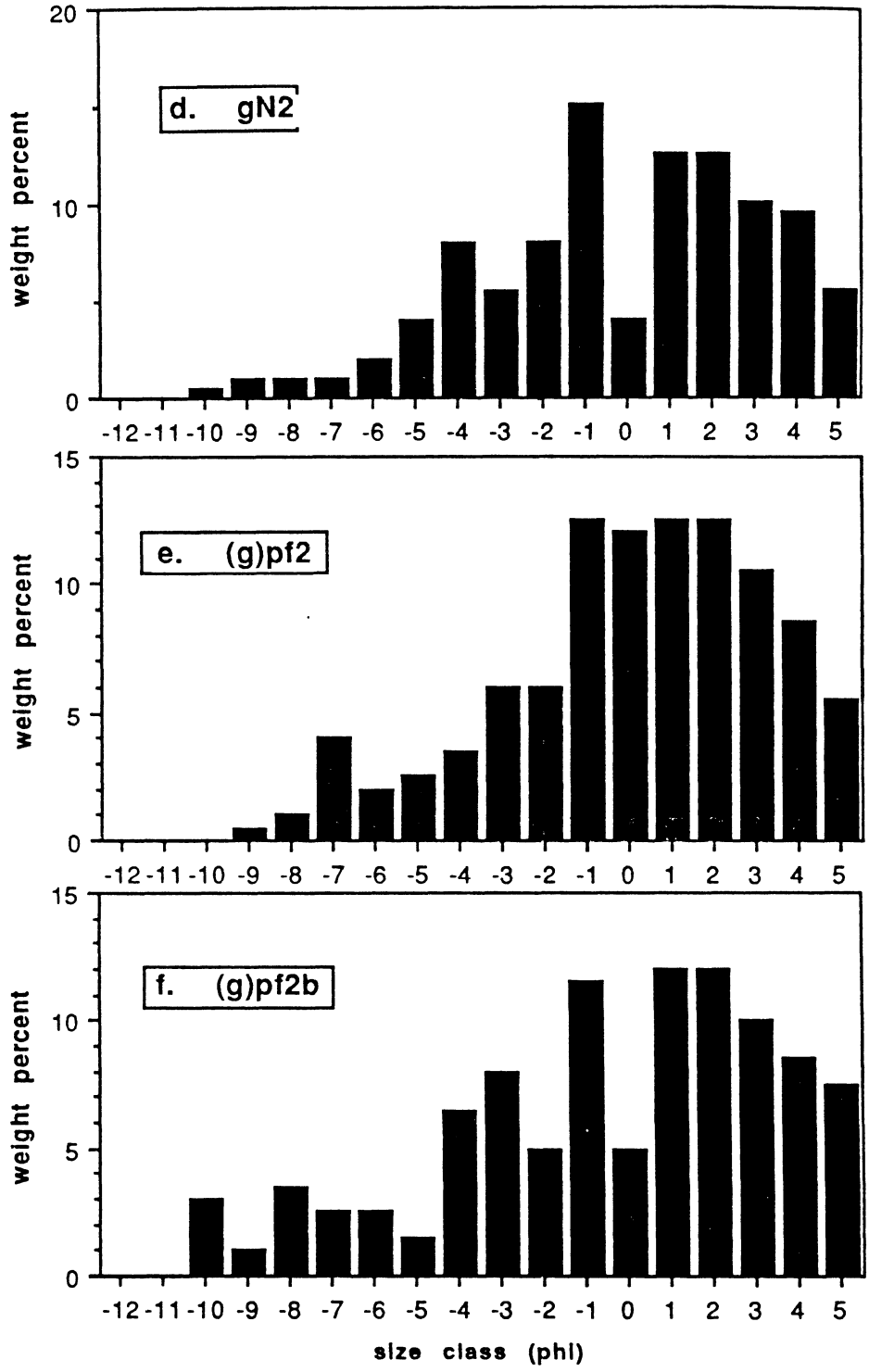


**Fig. 4.1d–f** Grain size distribution histograms for deposits gN2, (g)pf2, and (g)pf2b.

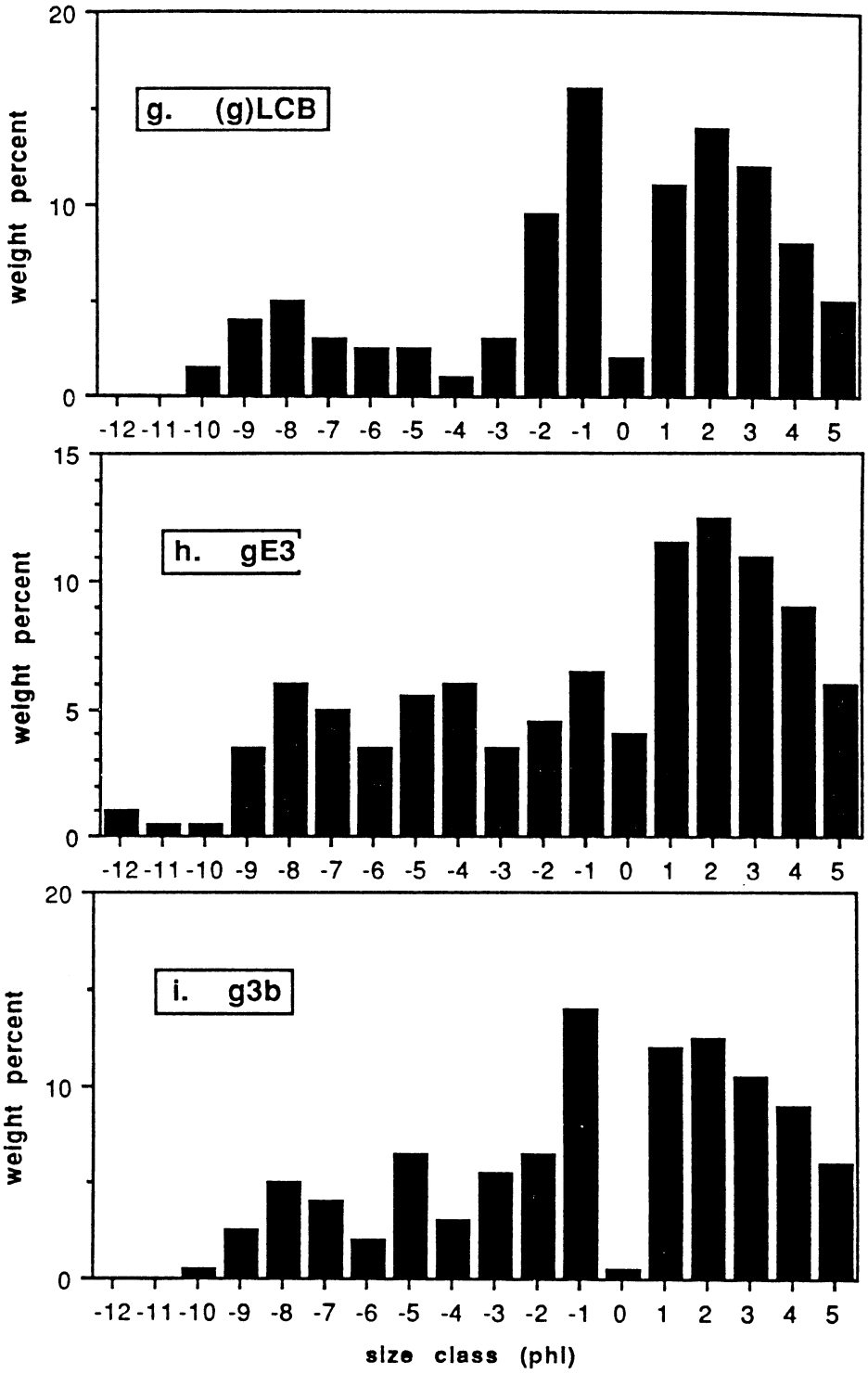


**Fig. 4.1g–i** Grain size distribution histograms for deposits (g)LCB, gE3, and g3b.

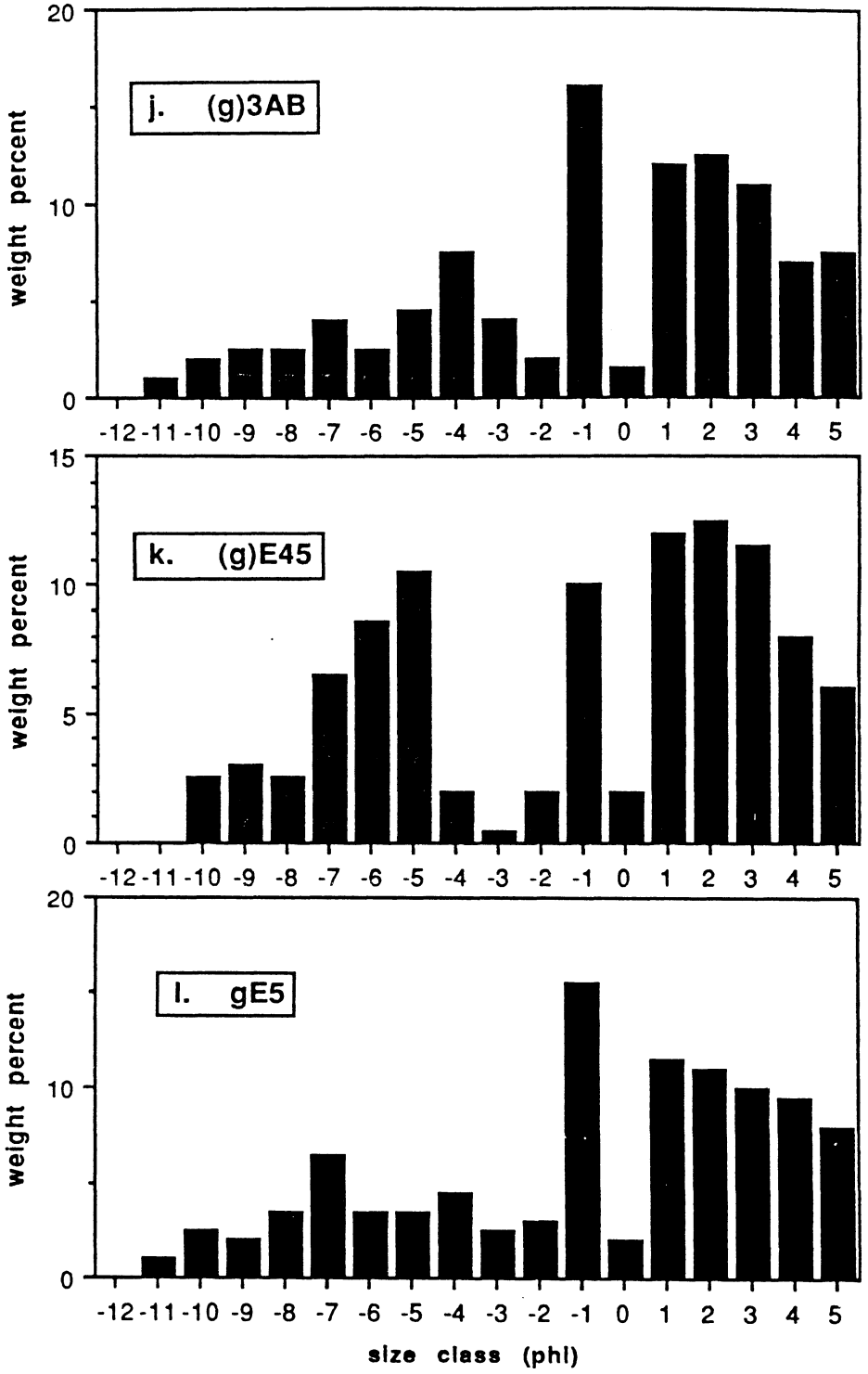


**Fig. 4.1j–l** Grain size distribution histograms for deposits (g)3AB, (g)E45, and gE5.

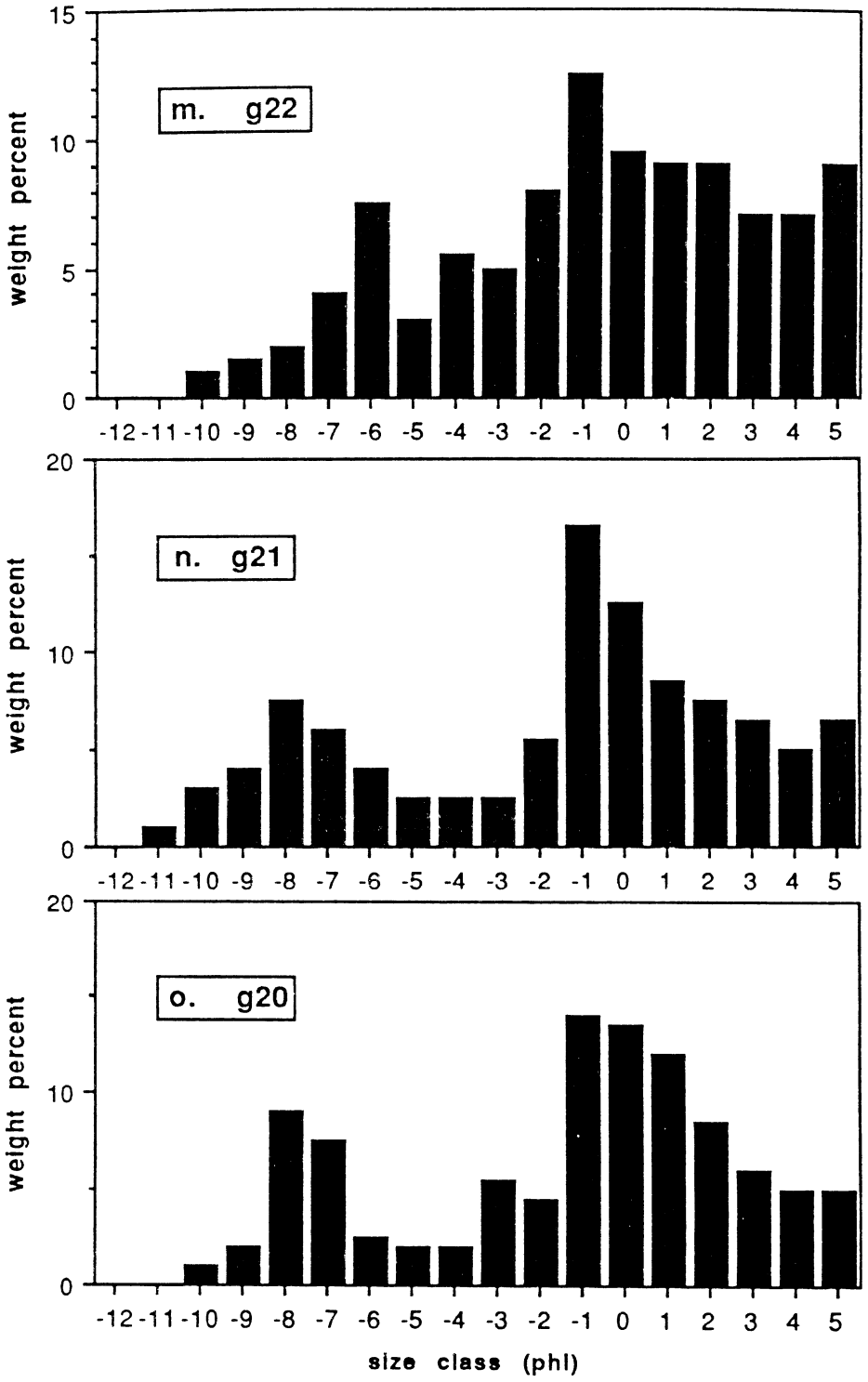


**Fig. 4.1m–o** Grain size distribution histograms for deposits g22, g21, and g20.

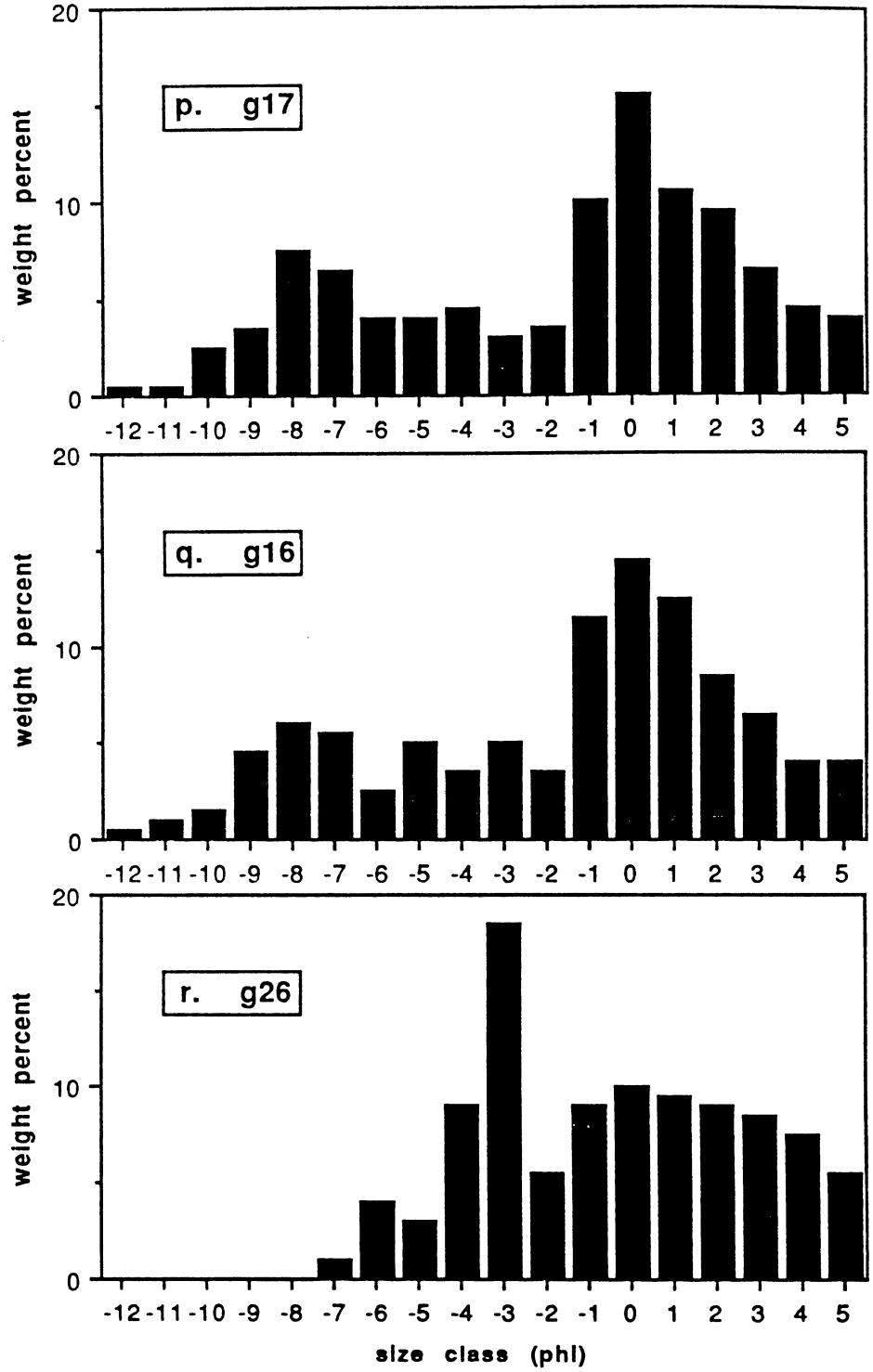


**Fig. 4.1p–r** Grain size distribution histograms for deposits g17, g16, and g26.

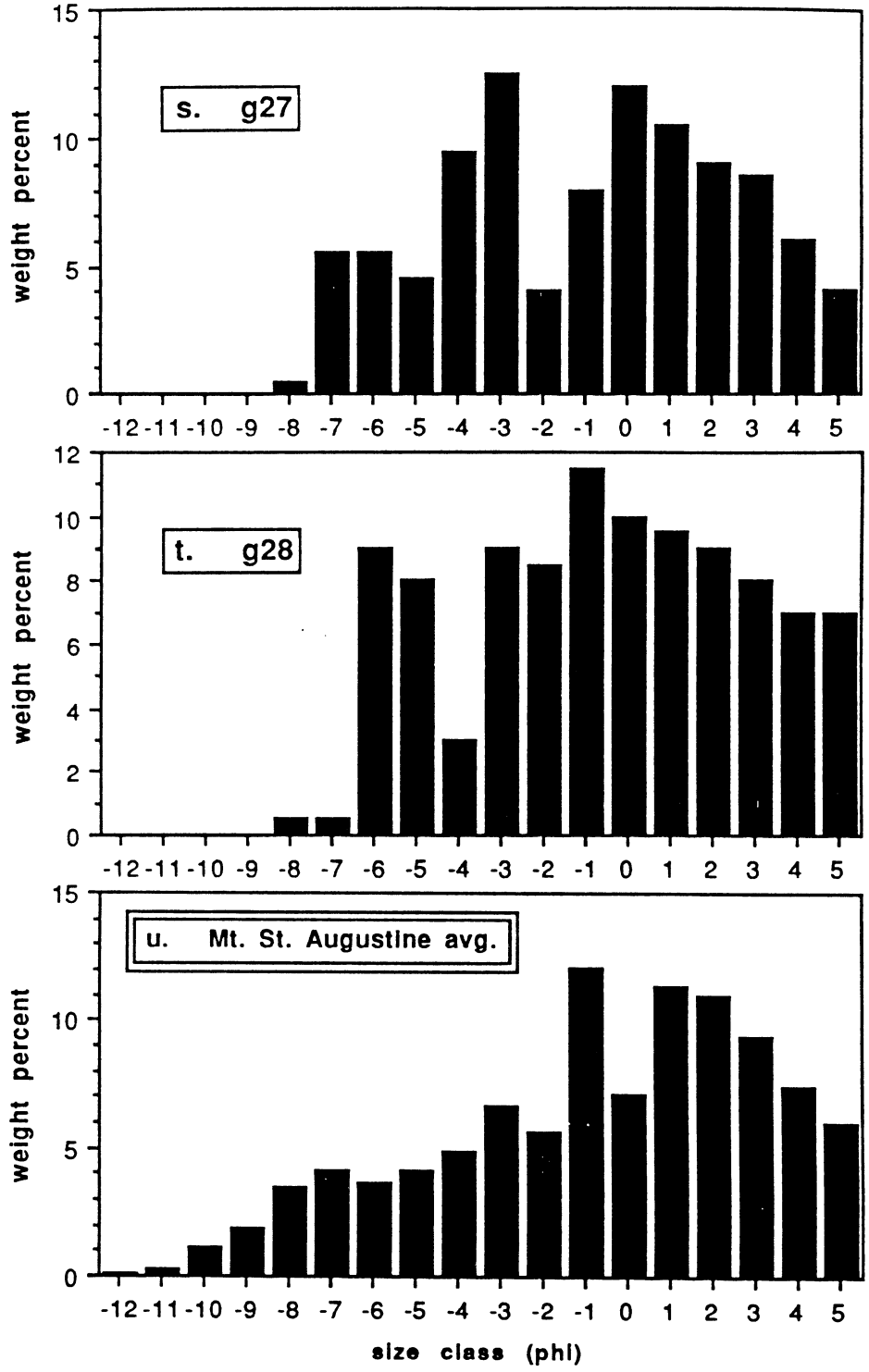


**Fig. 4.1s–u** Grain size distribution histograms for deposits g27 and g28, and Mt. St. Augustine average.

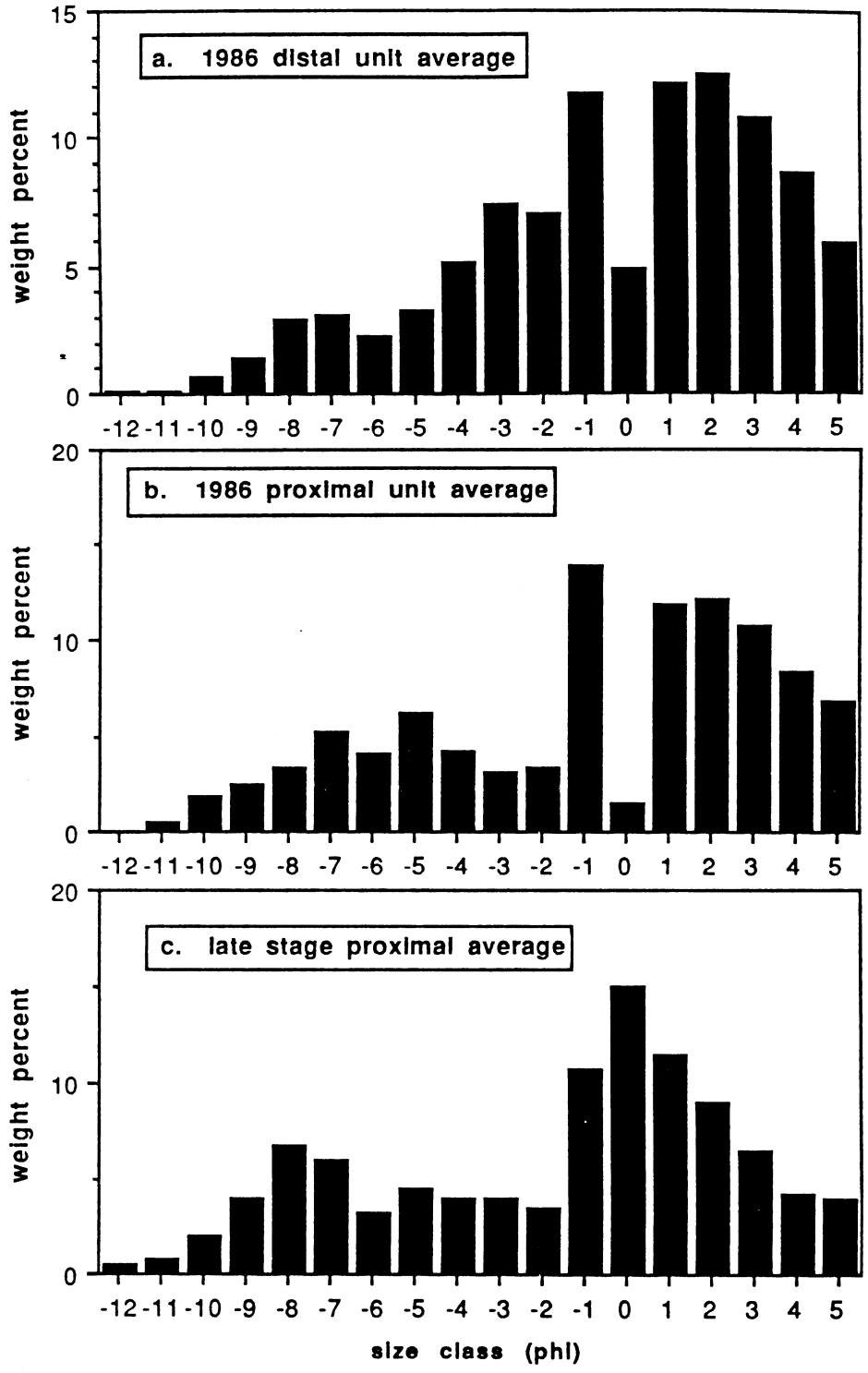


**Fig. 4.2a–c** Grain size distribution histograms for 1986 distal average, 1986 proximal average, and late-stage distal average.

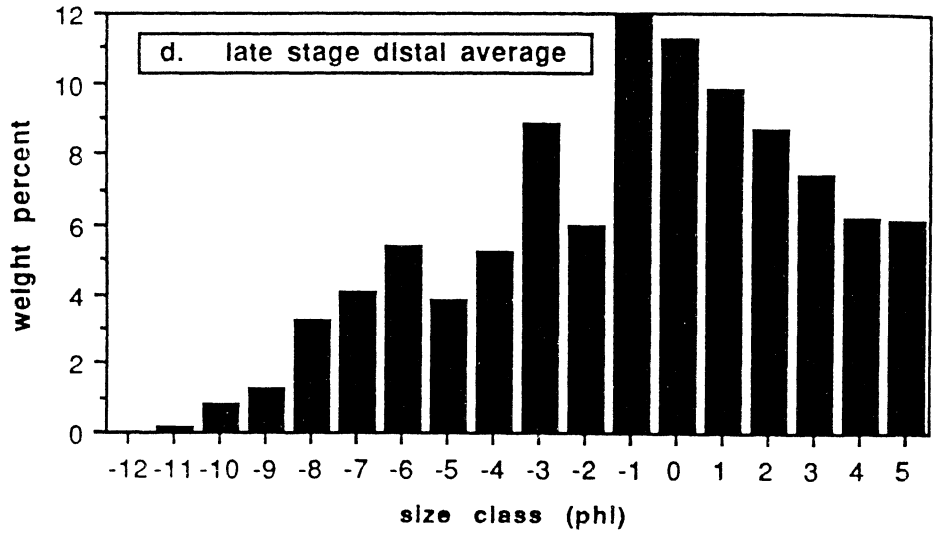


**Fig. 4.2d** Grain size distribution histogram for late-stage distal average.

**Table 4.1. Granulometric Summary of the 1986 Deposits.**

| Station number | Histogram number | Distance from source (m) | Mean (phi) | Sorting (phi) | Skewness |
|---|---|---|---|---|---|
| **MSA average** | - | - | -1.23 | 3.86 | -0.54 |
| **1986 distal** | | | | | |
| gN3 | 4.1 a | 4200 | -0.60 | 3.41 | -0.32 |
| gN1 | 4.1 b | 4010 | -0.76 | 3.44 | -0.46 |
| gN1a | 4.1 c | 3800 | -0.70 | 3.31 | -0.55 |
| gN2 | 4.1 d | 4930 | -0.58 | 3.29 | -0.52 |
| (g)pf2 | 4.1 e | 3400 | -0.41 | 3.18 | -0.65 |
| (g)pf2b | 4.1 f | 3210 | -0.91 | 3.90 | -0.68 |
| (g)LCB | 4.1 g | 4360 | -1.06 | 3.98 | -0.77 |
| gE3 | 4.1 h | 3250 | -1.50 | 4.40 | -0.53 |
| *average* | 4.2 a | - | -0.81 | 3.65 | -0.64 |
| **1986 proximal** | | | | | |
| g3b | 4.1 i | 2000 | -1.11 | 3.94 | -0.54 |
| (g)3AB | 4.1 j | 1900 | -1.16 | 4.10 | -0.64 |
| (g)E45 | 4.1 k | 2050 | -1.61 | 4.38 | -0.40 |
| gE5 | 4.1 l | 2200 | -1.22 | 4.31 | -0.61 |
| *average* | 4.2 b | - | -1.27 | 4.19 | -0.55 |
| **late stage distal** | | | | | |
| g22 | 4.1 m | 3490 | -1.22 | 3.82 | -0.36 |
| g21 | 4.1 n | 2930 | -2.16 | 4.36 | -0.41 |
| g20 | 4.1 o | 2860 | -1.83 | 3.98 | -0.47 |
| g26 | 4.1 p | 5160 | -0.97 | 3.11 | 0.05 |
| g27 | 4.1 q | 5160 | -1.42 | 3.37 | -0.13 |
| g28 | 4.1 r | 5160 | -1.05 | 3.36 | -0.10 |
| *average* | 4.2 c | - | -1.44 | 3.72 | -0.37 |
| **late stage proximal** | | | | | |
| g17 | 4.1 s | 800 | -2.25 | 4.25 | -0.44 |
| g16 | 4.1 t | 500 | -2.12 | 4.14 | -0.53 |
| *average* | 4.2 d | - | -2.18 | 4.19 | -0.49 |

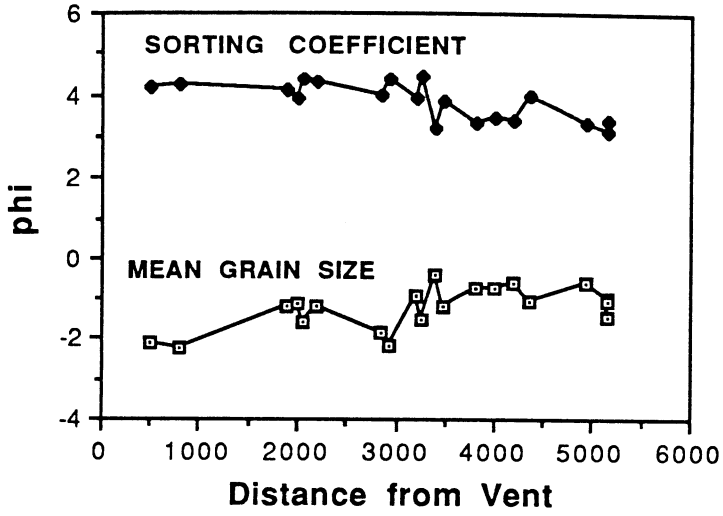


**Fig. 4.3** Plots of mean grain size and sorting coefficient vs. distance from vent. Data suggest decreasing grain size and improved sorting with vent distance.

### 4.4 Discussion.

An assumption in use with grid by number and bulk sampling on the surface of a deposit is that the surface displays an unbiased representation of the entire thickness of the layer 2b. Layer 2b is interpreted as the deposit of the non-turbulent plug riding on top of a basal shearing zone. As such, little or no shearing would take place during its deposition except for right at the base of the layer whose coarser clasts must necessarily be excluded from layer 2a below. The plug flow interpretation for layer 2b would therefore dictate there is no significant difference between the surface and any random cut through the deposit.

Vertical sections through the 1986 pyroclastic flow deposits were extremely rare at the time of field work, making significantly meaningful corroboration of this interpretation impossible. However, a qualitative assessment can be attempted by comparing the distribution

from g27 and g26, both sampled on the surface, and g28, sampled from a vertical cut at the beach (fig. 4.1r–t and Table 4.1). The relative enrichment in the clast fraction and the mean grain size of the vertical section sample fall between the parameter magnitudes for the two surface samples. No significant difference based on flow position or the sampling techniques can be concluded from these data. The upper zone of stream-cut section S2 (fig. 1.3b) displays apparent reverse grading. The clast-supported nature of the upper zone and the morphology of the surface indicates levee deposition.

Davies et al. (1978) observe bimodal distributions for thirteen sampling stations on a fresh block and ash flow deposit in a ravine known as Quebrada el Pajal, flanking Volcano Fuego in southern Guatemala. Bimodal distributions also occur in size data of Moore (1934) and Murai (1961) which, along with the El Pajal deposits, exhibit an intermodal low at $-1.0\,\phi$. It should be noted that the intermodal low at $-1.0\,\phi$ observed in eight of the Mt. St. Augustine samples may have some basis in the sampling techniques employed in this study; the low occurs at the breakpoint between the percent frequency by number and the weight percent data sets for each samples.

The El Pajal block and ash flow deposit is similar in genesis and scale to the block and ash flow deposits at Mt. St. Augustine. The cumulative grain size distribution curves from the two studies are also very similar, except that the El Pajal deposits are slightly coarser than the Mt. St. Augustine group averages (fig. 4.4). The Mt. St. Augustine deposits plot on the coarser side of the field of Japanese "intermediate nuée ardentes" of Murai (1961) in the $< -4\,\phi$ range, but overlap almost exactly in the remainder of the distribution.

Sheridan (1979) has plotted cumulative grain size distributions for all published analyses contained in Sparks (1976). The Mt. St. Augustine group distributions all plot at least one and quite often two size classes (less than one standard deviation) coarser than the median of all known analyses (fig. 4.5). The median grain size for the Mt. St. Augustine

deposits falls into the lapilli range and the median for all known deposits falls into the ash range.

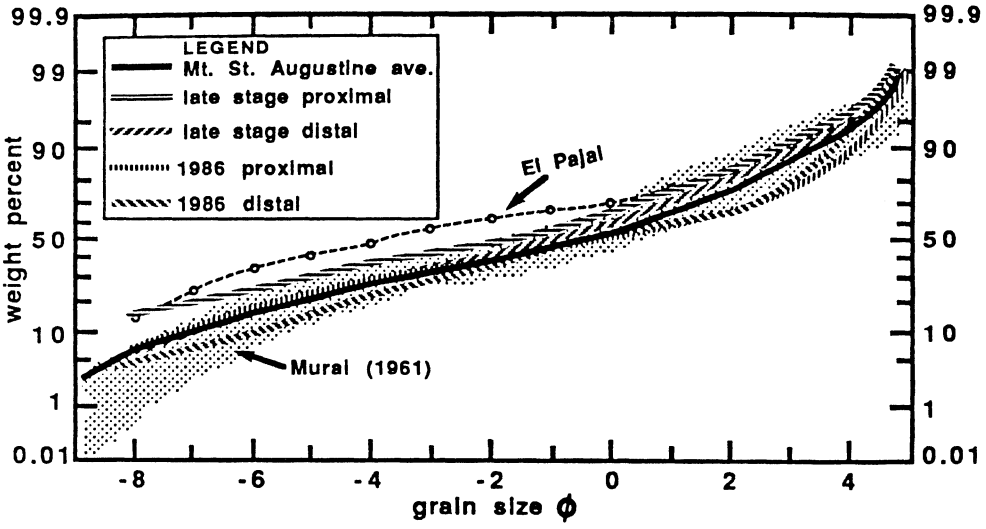


**Fig. 4.4** Comparison plot of cumulative curves with those from similar Guatemalan and Japanese deposits (after Davies et al. 1978).

Value of median grain size versus sorting coefficient for the Mt. St. Augustine flow units plot on the coarse end of the pyroclastic flow field (fig. 4.6) on Walker's (1971) compilation plot. Walker states that the closure of the 1% contour line near $-2.5\,\phi$ is an artifact of the scarcity of grain size analyses performed for coarser grained nuée ardente deposits. Most of the three hundred analyses used for his compilation plot were collected from larger pumice-rich ignimbrites having different modes of emplacement, bulk compositions, and sedimentological features.

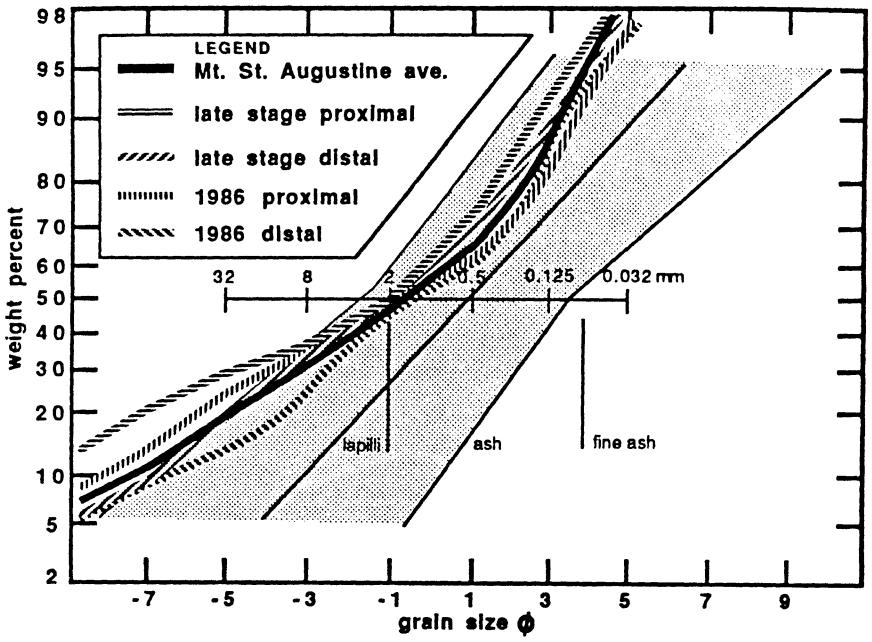


**Fig. 4.5** Comparison plot of cumulative curves with those of all published analyses of pyroclastic flow deposits. Stippled field represents two standard deviations from the plotted average, at center (after Sheridan 1979).

Qualitative observations made during field reconnaissance concerning apparent decrease in clast size and improvement in sorting with increasing vent distance are substantiated by the collected grain size data. At first, this conclusion may appear contradictory to the plug flow transport model interpreted for layer 2b. However, grain dispersive pressures operating at the turbulent flow head preferentially exclude the largest clasts due to their proportionally greater surface area. These clasts eventually migrate to regions of lower pressure, i.e., to the levees. Behind the flow head, where no turbulence is inferred for true plug flow, the largest clasts, by virtue of their proportionally greater size and mass, are more likely to be subjected to dispersive pressures generated by the shearing base of the flow, especially if the effective clast diameter is nearly equal to the thickness of the plug.

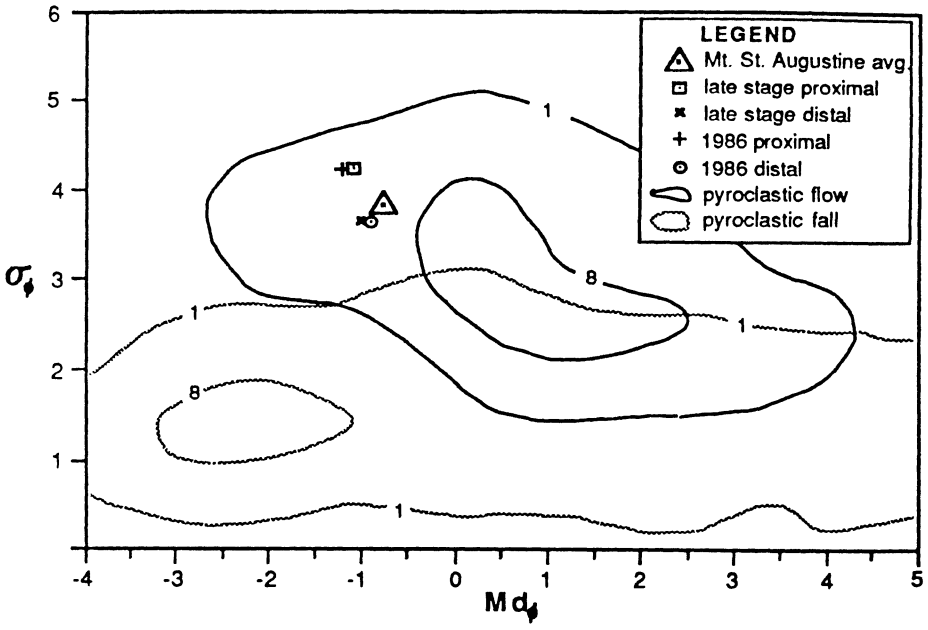


**Fig. 4.6** Plot of median grain size vs. sorting coefficient. Fields of all published pyroclastic fall and flow data are contoured showing the outer 1% and 8% of data points. Mt. St. Augustine data plot on coarse end of pyroclastic flow field (after Walker, 1971).

## CHAPTER 5:

## SUMMARY AND CONCLUSIONS

### 5.1 General Project Summary.

Pyroclastic flows represent the most general case of grain flow wherein particle collisions between grains having a wide size distribution are responsible for the transfer of flow momentum. Grain flow mechanisms have been explained by Bagnoldian dispersive pressure generated by shearing at the base of flow (Bagnold 1954; Lowe 1976). Flow unit stratigraphy observed in the 1986 Mt. St. Augustine deposits is suggestive of basal shear operating during emplacement; the layer 2a (Sparks et al. 1973) seen in all vertical sections is interpreted to represent a basal shear zone.

The flow deposits display well-developed levees, channels, and lobate termini which indicate non-Newtonian rheological properties characterizing the active flows. The flows are therefore modeled as Bingham materials having plastic strength and fluid viscosity. These materials behave as elastic substances up to a critical stress condition called the yield strength. When the yield strength is exceeded, they behave as viscous fluids whose steady-state velocity distribution is proportional to the coefficient of Bingham viscosity. Expressions developed by Johnson and Rodine (1984) estimating yield strength and Bingham viscosity from deposit morphometry were used to characterize the rheology of the 1986 Mt. St. Augustine pyroclastic flows.

Some knowledge of the flow density is required for the calculation of the Bingham parameters. Density of the modeled block and ash flows was taken to be the average of densities determined from matrix samples collected for grain size analysis. Density was also

calculated for a lithic-rich pumice flow deposit from an accidentally-entrained "hydrometer," although this particular deposit was not part of the modeling studies.

Yield strength was calculated from the deposit unit weight (derived from average density and assumed to be constant for all modeled flow units), the deposit critical thickness as defined by the height of the lateral levees, and the basal slope on which the deposit rests. Calculated yield strengths were shown to significantly decrease with increasing distance from the vent. Also, the results are of the same order of magnitude with results published for other types of sediment gravity flows.

Coefficients of Bingham viscosity were calculated from the yield strength parameters, active flow depths, and flow velocities at selected reaches on the deposits. Flow depths were assumed to be proportional to the critical thicknesses due to a lack of direct observational data of the moving flows. Flow velocities were reconstructed from the superelevation of levee deposits on curved reaches. Bingham viscosity values show no significant trend with increasing vent distance at Mt. St. Augustine, and are of similar magnitude as those published for a large ignimbrite, debris flows, pumiceous pyroclastic flows, and mudflows.

Flow regimes for the studied pyroclastic flows were evaluated from the rheological parameters. Values calculated for the dimensionless Bingham number (Middleton and Southard 1984) and the modified Froude number (Valentine and Fisher 1986) show that all studied flow units were emplaced under non-turbulent, subcritical flow conditions.

Three kinematic models were developed to characterize pyroclastic flow velocity. The models predict the change in momentum of a pyroclastic flow that results from the difference between the driving force and the braking forces acting on it. The models are one-dimensional and algebraic. The basic modeling control utilizes Coulomb's law of sliding friction for non-equilibrium conditions to evalute flow acceleration/deceleration at the calculation points (in $x, y$ space) defining the travel path of a particular deposit. The choice of braking mechanisms distinguishes the three models.

The braking force in Model 1 is proportional to a constant coefficient of total friction. This coefficient is analogous to the coefficient of sliding friction in Coulomb's law, but it is assumed to also include the energy losses from turbulence at the flow head, particle collisions, and shear at the base of flow. The coefficient of total friction is estimated from the fahrböschung (Hsü 1978) which represents an "energy line," or gradient of fluid potential, for the flowing material.

The performance of Model 1 was tested for the well- constrained flow velocities observed for a pumiceous pyroclastic flow at Mt. St. Helens (Hoblitt 1986). The modeled flow velocities were consistently greater than the observed, but the general flow behavior was reproduced. In particular, the model flow accelerates where the slope is steeper than the fahrböschung and decelerates where it is shallower, just as the actual flow was observed to do.

Model 2 attempts to more precisely specify the source of friction within pyroclastic flows by incorporating a velocity-dependent fluid resistance term in its controlling equation. This term is constructed from the initial velocity at each calculation point multiplied by a coefficient called the kinetic energy flux which describes a pyroclastic flow's energy dissipation properties. A dimensional analysis was used to derive the kinetic energy flux coefficient from the functional relationship existing between a flow's yield strength, Bingham viscosity, and velocity using the Buckingham Π theorem (Streeter and Wylie 1985). The resulting coefficient was calibrated using the Mt. St. Helens data set, then input into the model.

Model 2's predicted velocities at Mt. St. Helens were more accurate than Model 1's. Resistance to flow in Model 2 is proportional to velocity—a characteristic of viscous fluids. Bingham rheology is implicitly accounted for in the kinetic energy flux coefficient, but the model is insensitive to the yield criterion as evidenced by the non-zero velocity predicted at the flow terminus.

Model 3 redefines the coefficient of total friction of Model 1 to be a coefficient of total *Bingham* friction, thus specifically linking flow resistance to a flow's rheology. This new coefficient is derived by combining Coulomb's law with the equation for Bingham viscosity. The use of Model 3 requires the interactive input of flow depth at each calculation point. For the test run at Mt. St. Helens, flow depths had to be modulated only by about 1 m in order to duplicate exactly the velocities observed by Hoblitt. However, extreme flow depths were needed in order to maintain flow on the gently sloping pumice plain. The sensitivity of Model 3 to slight changes in flow depth relates to the role that flow weight (i.e., the weight of material having the input flow depth) plays as the driving force.

Output of the three models run for ten lithic block and ash flow units and one pumice flow unit at Mt. St. Augustine was compared to the following: (1) reconstructions of flow velocities based on superelevation of the levee deposits; (2) reconstructions of flow velocities based on the runup of ash cloud deposits; and (3) an observed velocity of 40 m/s at a distance of 1500 m from the vent.

Model 1 predicts the highest pyroclastic flow velocity of the three models. The dependence of the total friction coefficient on the fahrböschung dictates that larger flows, with longer runout, will have smaller friction coefficients. The result is that the modeled flows achieve very high velocities on the steeper reaches. The velocities calculated using Model 2 are in all cases closer to the field-derived velocity reconstructions. Also, the sawtooth velocity profile mimics the pulsating nature of pyroclastic flow advancement observed by Kienle (personal communication 1986) for a small-scale block and ash flow at Mt. St. Augustine. Model 3 reproduces the effect that an increase in mass (i.e., a depth increase) has on flow velocity; it is very sensitive to slight modulations of the depth parameter. Interactively input flow depths are constrained by channel depths where possible; however, field data for each studied flow unit are sparse due to onlapping of subsequent pyroclastic flow deposits.

Two sampling techniques were combined in order to characterize the tremendous range in grain sizes ($> 4$ m to $< 0.03$ mm) observed for the 1986 deposits. The data set was transformed and shows a near log-normal size distribution. The twenty sampled flow units were grouped according to distance from vent and relative age. Descriptive statistics calculated by the method of moments reveal significant decrease in mean grain size and improvement in deposit sorting with increasing vent distance for individual deposits and for group averages. The cumulative curves for the group averages plot within the fields of published data for like deposits.

### 5.2 Conclusions and Evaluation of Modeling.

Interactions between flowing pyroclastic particles are viewed as analogous to molecular cohesion in ideal Bingham substances. The assumption of Bingham behavior is only a first approximation of flow mechanisms for pyroclastic flows. Deposit morphology requires effective strength and effective viscous properties.

The statistically significant decrease in calculated yield strength values is related to decreasing mean grain size with distance. Deposits near the vent contain a greater proportion of coarser clasts; this fact is verified by the granulometry. The bulk density of the flows depositing on the proximal reaches will therefore also be greater. Because flow density is proportional to unit weight, yield strength must also be greater according to equation (2.8). Yield strength values listed in Table 2.1 were calculated using constant unit weight, so for the proximal flow units, these values represent lower limits to the flows' true effective yield strengths.

The one-dimensional nature of the models employed in this study is an obvious simplification of the complexities of pyroclastic flow. Also, two admittedly untrue assumptions are in use: constant unit weight and constant rheological properties. Lack of data prevents

quantifying the variability (with time and distance) of these parameters for the individual flow units.

Model output accuracy in this exercise was checked using reconstructed flow velocities. Velocity from superelevation (equation 2.13) is derived for fluids, and the expression has been shown to accurately reproduce observed mean velocities of mud-mediated debris flows (Johnson and Rodine 1984). Because pyroclastic flows and debris flows exhibit similar rheological properties (Table 2.2), the application of (2.13) to pyroclastic flow deposits is thought to accurately reconstruct their emplacement velocities.

The utility of any numerical model should be judged on its ability to reproduce an observable phenomenon within acceptable limits of accuracy from readily quantifiable parameters. For the purposes of this exercise, Model 2 outperforms the other models in this context. Model 1 is the easiest to use in that the single controlling parameter (the fahrböschung-derived coefficient of total friction) can be rapidly determined. However, the resulting output velocities are unacceptably high. Model 3 most explicitly uses a flow's rheological properties to define the coefficient of Bingham friction. However, its use requires the knowledge of flow depth throughout the length of the travel path, and such data cannot readily be collected on the pyroclastic fan at Mt. St. Augustine. Model 2's controlling parameter, the kinetic energy flux coefficient, implicitly accounts for Bingham rheology, and is readily evaluated from deposit morphometry. Calculated output velocities reproduce the field-derived velocity reconstructions with acceptable accuracy.

## REFERENCES CITED


Bagnold, R.A. (1954) Experiments on a gravity-free dispersion of large solid spheres in a Newtonian fluid under shear; *Proc. Roy. Soc. London*, A **225**:49–63.

Begét, J.E., Limke, A.J. (1989) Density and void ratio of a small pyroclastic flow on emplacement, Mt. St. Augustine, Alaska; *Jour. Volc. Geotherm. Res.*, **39**:349–353.

Begét, J.E., Limke, A.J. (1988) Two dimensional kinematic and rheological modeling of the 1912 pyroclastic flow, Katmai, Alaska; *Bull. Volc.*, **50**:148–160.

Cannon, S.H., Savage, W.Z. (1988) A mass change model for the estimation of debris flow runout; *Jour. Geology*, **96**:221–227.

Chen, C. (1987) Comrehensive review of debris flow modeling concepts in Japan; in Costa, J.E., and Wieczorek, G.F. (eds), Debris Flows/Avalanches: Process, Recognition, and Control; Geol. Soc. Amer., Reviews in Eng. Geol., Vol. VII, 13–29.

Daley, E.E. (1986) Petrology, geochemistry, and evolution of lavas at Augustine Volcano, Alaska; M.S. Thesis, Univ. Alaska, Fairbanks, 106 p.

Davies, D.K., Quearry, M.W., Bonis, S.B. (1978) Glowing avalanches from the 1974 eruption of the volcano Fuego, Guatemala; *Geol. Soc. Amer. Bull.*, **89**:369–384.

Davies, J.N., Kienle, J. (1986) The 1986 eruption of Mt. St. Augustine, Alaska: a case study in the successes and failures of scientific advice during a volcanic crisis, (abs); *EOS Trans. Amer. Geophys. Union*, **67**(44):1259.

Davis, J.C. (1986) Statistics and Data Analysis in Geology; John Wiley and Sons, New York, 646 p.

Eppler, D.B., Fink, J., Fletcher, R. (1987) Rheologic properties and kinematics of emplacement of the Chaos Jumbles rockfall avalanche, Lassen Volcanic National Park, California; *Jour. Geophys. Res.*, **92**: 3623–3633.

Erismann, T.H. (1979) Mechanisms of large landslides; *Rock Mechanics*, **12**:15–46.

Fink, J.H., Malin, M.C., D'Alli, R.E., Greeley, R. (1981) Rheological properties of mudflows associated with the spring 1980 eruptions of Mt. St. Helens volcano, Washington; *Geophys. Res. Letters*, **8**(1):43–46.

Fisher, R.V., Schmincke, H.-U. (1984) Pyroclastic Rocks; Springer-Verlag, Berlin, 472 p.

Freundt, A., Schmincke, H.-U. (1986) Emplacement of small-volume pyroclastic flows at Laacher See (East Eifel, Germany); *Bull. Volc.*, **48**:39–60.

Gallino, G.L., Pierson, T.C. (1985) Polallie Creek debris flow and subsequent dam-break flood of 1980, East Fork Hood River basin, Oregon; U.S. Geol. Surv. *Water-Supply Paper* 2273, 22 p.

Harris, G.W. (1991) Petrology and geochemistry of the 1986 eruption of Augustine Volcano; M.S. Thesis (in progress), Univ. Alaska, Fairbanks.

Harris, G.W., Swanson, S.E., Nye, C.J. (1987) Composition, petrology and petrography of the 1976 and 1986 ejecta of Augustine Volcano, Alaska; *Geol. Soc. Amer. Abstracts with Programs*, **19**:387.

Henderson, F.M. (1966) Open Channel Flow; Macmillan, New York, 563 p.

Hoblitt, R.P. (1986) Observations of the eruptions of July 22 and August 7, 1980, at Mt. St. Helens, Washington; U.S. Geol. Surv. *Prof. Paper* 1335, 44 p.

Hsü, K. (1978) Albert Heim: Observations on landslides and relevance to modern interpretations; in Voight, B. (ed), Rockslides and Avalanches 1, Natural Phenomena; Elsevier, Amsterdam, 69–93.

Hsü, K. (1975) Catastrophic debris streams (Sturtzstroms) generated by rockfalls;*Geol. Soc. Amer. Bull.*, **86**:129–140.

Inman, D.L. (1952) Measures for describing the size distribution of sediments; *Jour. Sediment. Petrol.*, **22**:125–145.

Johnson, A.M. (1984) Physical Processes in Geology (Reissue with emandations); Freeman, Cooper, San Francisco, 571 p.

Johnson, A.M. (1970) Physical Processes in Geology; Freeman, Cooper and Co., San Francisco, 571 p.

Johnson, A.M., Rodine, J.R. (1984) Debris flow; in Brunsden, D. and Prior, D.B. (eds), Slope Instability, John Wiley and Sons, New York, 257–361.

Johnston, D.A. (1978) Volatiles, magma mixing, and the mechanism of eruption of Augustine Volcano, Alaska; Ph D. dissertation, Univ. Washington, Seattle, 177 p.

Jones, B.C., Chinn, S.S.W., Brice, J.C. (1984) Olokele rock avalanche, island of Kauai, Hawaii; *Geology*, **12**:209–211.

Kellerhals, R., Bray, D.I. (1971) Sampling procedures for coarse fluvial sediments; *ASCE Jour. Hyd. Div.*, **97**:1165–1180.

Kienle, J. (1986) Volcanic events—Augustine volcano; *EOS Trans. Amer. Geophys. Union*, **67**(39):804.

Kienle, J., Davies, J.N., Miller, T.P., Yount, M.E. (1986) 1986 Eruption of Augustine Volcano: public safety response by Alaskan volcanologists; *EOS Trans. Amer. Geophys. Union*, **67**(29):580–582.

Kienle, J., Swanson, S.E. (1985) Volcanic hazards from future eruptions of Augustine Volcano; Report UAG R-275, 2nd ed., Geophys. Inst., Univ. Alaska, Fairbanks, 126 p.

Kienle, J., Forbes, R.B. (1976) Augustine-evolution of a volcano; Ann. Report 1975/76, Geophys. Inst., Univ. Alaska, Fairbanks, 26–48.

Krumbein, W.C. (1938) Size frequency distribution of sediments and the normal phi curve; *Jour. Sediment. Petrol.*, **8**:84–90.

Limke, A.J., Begét, J.E. (1989) Rheological and kinematic characteristics of the 1986 pyroclastic flows at Mt. St. Augustine, Alaska; (abs), Continental Magmatism Abstracts, IAVCEI, New Mexico Bur. Mines and Min. Resources., Bull. 131, p 163.

Limke, A.J., Begét, J.E. (1986) Emplacement velocities and rheological properties of pyroclastic flows during the March 27–April 8 eruption of Mt. St. Augustine, Alaska, (abs); *EOS Trans. Amer. Geophys. Union*, **67**(44):1259.

Lowe, D.R. (1976) Grain flow and grain flow deposits; *Jour. Sediment. Petrol.*, **46**(1):188–199.

MacDonald, G.A. (1972) Volcanoes; Prentice-Hall, Englewood Cliffs, New Jersey, 426 p.

Malin, M.C., Sheridan, M.F. (1982) Computer assisted mapping of pyroclastic surges; *Science*, **217**:637–639.

McCammon, R.B. (1962) Moment measures and the shape of size frequency distributions; *Jour. Geology*, **70**:89–92.

McSaveney, M.J. (1978) Sherman Glacier rock avalanche, Alaska, USA; in Voight, B. (ed), Rockslides and Avalanches 1, Natural Phenomena; Elsevier, Amsterdam, 197–258.

McTigue, D.F. (1982) A nonlinear constitutive model for granular materials, application to gravity flow; *Jour. Applied Mech.*, ASME, **49**:291–296.

Mellors, R.A., Waitt, R.B., Swanson, D.A. (1988) Generation of pyroclastic flows and surges by hot-rock avalanches from the dome of Mt. St. Helens volcano, U.S.A.; *Bull. Volc.*, **50**:14–25.

Middleton, G.V., Southard, J.B. (1984) Mechanics of Sediment Movement; Soc. Economic Paleontologists and Mineralogists, Houston, 299 p.

Miller, T.P., Yount, M.E., Nelson, S.W. (1987) Pyroclastic flow characteristics during the initial phase of the 1986 eruption of Augustine Volcano, Alaska, (abs); Hawaii Symposium on How Volcanoes Work, U.S. Geol. Surv. Hawaii Volc. Obs., p 175.

Moore, B.N. (1934) Deposits of possible nuée ardente origin in the Crater Lake region, Oregon; *Jour. Geology*, **42**:358–375.

Moore, J.G., Melson, W.G. (1969) Nuées ardentes of the 1968 eruption of Mayon volcano, Philippines; *Bull. Volc.*, **33**:600–620.

Murai, I. (1961) A study of the textural characteristics of pyroclastic flow deposits in Japan; *Earthquake Res. Inst. Bull.*, **39**:133-248.

Nairn, I.A., Self, S. (1978) Explosive eruptions and pyroclastic avalanches from Ngauruhoe in February, 1975; *Jour. Volc. Geotherm. Res.*, **3**:39–60.

Reiner, M. (1960) Deformation, Strain, and Flow; H.K. Lewis and Co., London, 347 p.

Rodine, J.R., Johnson, A.M. (1976) The ability of debris, heavily freighted with coarse clastic materials, to flow on gentle slopes; *Sedimentology*, **23**:213–241.

Rose, W.I., Jr. (1973) Nuée ardente from Santaguito Volcano, April 1973; *Bull. Volc.*, **38**(3):365–371.

Sahu, B.K. (1964) Transformation of weight frequency and number frequency data in distribution studies of clastic sediments; *Jour. Sediment. Petrol.*, **34**:768–773.

Savage, S.B. (1979) Gravity flow of cohesionless granular materials in chutes and channels; *Jour. Fluid Mech.*, **92**:53–66.

Sears, F.W., Zemanski, M.W., Young, H.D. (1982) University Physics; Addison-Wesley, Reading, MA, 929 p.

Sheridan, M.F. (1979) Emplacement of pyroclastic flows: A review; *Geol. Soc. Amer. Special Paper* 180, 125–136.

Sheridan, M.F. (1980) Pyroclastic block flow from the September 1976 eruption of La Soufriére volcano, Guadaloupe; *Bull. Volc.*, **43**(2): 397–402.

Shreve, R.L. (1968) The Blackhawk landslide; *Geol. Soc. Amer. Special Paper* 108, 47 p.

Smith, R.L. (1960) Ash flows; *Geol. Soc. Amer. Bull.*, **71**: 795–842.

Sparks, R.S.J. (1976) Grain size variations in ignimbrites and implications for the transport of pyroclastic flows; *Sedimentology*, **23**:147–188.

Sparks, R.S.J., Self, S., Walker, G.P.L. (1973) Products of ignimbrite eruptions; *Geology*, **1**:115–118.

Sparks, R.S.J., Wilson, L., Hulme, G. (1978) Theroretical modeling of the generation, movement, and emplacement of pyroclastic flows by column collapse; *Jour. Geophys. Res.*, **83**(B4):1727–1739.

Stith, J.L., Hobbs, P.V., Radke, L.F. (1977) Observations of a nuée ardente from the St. Augustine volcano; *Geophysical Res. Letters*, **5**:259–62.

Streeter, V.L., Wylie, E.B. (1985) Fluid Mechanics; McGraw-Hill, New York, 586 p.

Swanson, S.E., Kienle, J. (1988) The 1986 eruption of Mt. St. Augustine field test of a hazard evaluation; *Jour. Geophys. Res.*, **93**(B5):4500–4520.

Swanson, S.E., Kienle, J. (1987) Volcanic hazard assessment of the 1986 eruption of Mt. St. Augustine, Alaska, (abs); Hawaii Symposium on How Volcanoes Work, U.S. Geol. Surv. Hawaii Volc. Obs., p. 246.

Ui, T., Yamamoto, H., Suzuki-Kamata, K. (1986) Characterization of debris avalanche deposits in Japan; *Jour. Geophys. Res.*, **93**(B5):4500–4520.

Valentine, G.A., Fisher, R.V. (1986) Origin of layer 1 deposits in ignimbrites; *Geology*, **14**:146–148.

Valentine, G.A., Wohletz, K.H. (1989) Environmental hazards of pyroclastic flows determined by numerical models; *Geology*, **17**:641–644.

Vallance, J.W., Rose, W.I. (1989) Experimental pyroclastic density currents; (abs), Continental Magmatism Abstracts, IAVCEI, New Mexico Bur. Mines and Min. Resources, Bull. 131, p. 276.

Voight, B., Janda, R.J., Glicken, H.X., Douglass, P.M. (1983) Nature and mechanics of the Mt. St. Helens rockslide-avalanche of 18 May 1980; *Geotech*, **33**:243–273.

Walker, G.P.L. (1971) Grain size characteristics of pyroclastic deposits; *Jour. Geology*, **91**:696–714

Wilson, L., Head, J.W. (1981) Morphology and rheology of pyroclastic flows and their deposits, and guidelines for future observations; in Lipman, P.W. and Mullineaux, D.R. (eds), The 1980 eruptions of Mt. St. Helens, Washington, U.S. Geol. Surv. *Prof. Paper* 1250, 513–524.

## APPENDIX A

### Derivation of Velocity From Superelevation Equation (2.13).

The element of fluid in fig. A.1 is shown undergoing uniform rotation about an arc having radius $r_c$. The forces acting on its center of mass are its weight $w$, and the normal force $N$ exerted by the container on it. The normal force $N$ acts in a direction perpendicular to the fluid's free surface; the fluid surface is shown here to be tilting at an angle $\beta$ from the horizontal. $N$ is resolved into the vertical component $N\cos\beta$, and the horizontal component $N\sin\beta$. The center of mass has no vertical acceleration, so the vertical forces $N\cos\beta$ and $w$ are equal in magnitude. The centripetal force on the body is equal to the horizontal component $N\sin\beta$, which is equal to the mass $m$ times the centripetal acceleration $v^2/r$ (Sears et al. 1982);

$$N\sin\beta = m\frac{v^2}{r} \qquad (a.1)$$

$$N\cos\beta = w = mg. \qquad (a.2)$$

Dividing (a.1) by (a.2) results in

$$\tan\beta = \frac{v^2}{rg}$$

$$v = (rg\tan\beta)^{0.5} \qquad (a.3)$$

which is equation (2.13).

Table A.1 provides the channel parameters used in the calculation of flow velocities for the 1986 Mt. St. Augustine pyroclastic flows.

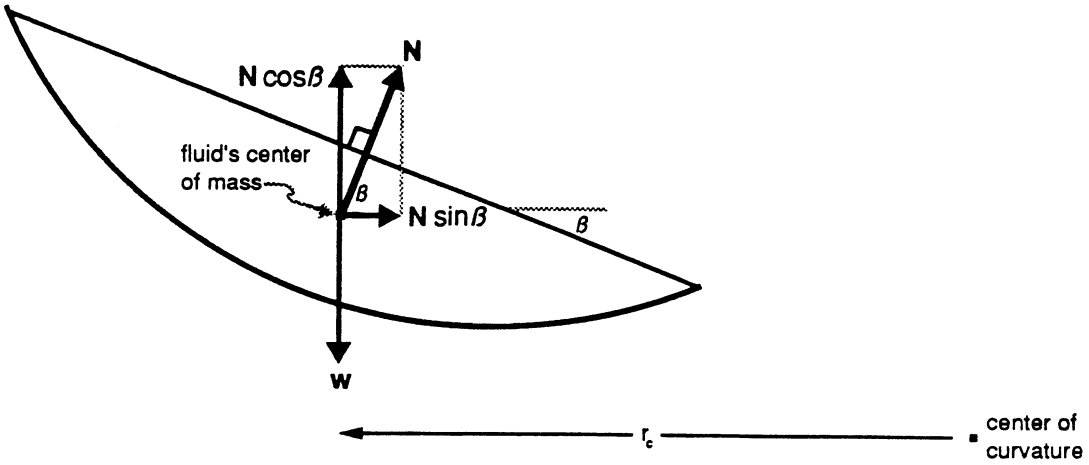


**Fig. A.1** Force diagram for a rotating fluid.

## Table A.1. Superelevation Field Data.

| Station number | Distance from source (m) | $r_c$ ($\times 10^2$ m) | $\beta$ (°) | $\overline{v}$ (m/s) |
|---|---|---|---|---|
| 14 | 480 | 3.8 | 13 | 29 |
| 6 | 730 | 3.7 | 14.5 | 30 |
| 5 | 790 | 3.7 | 9.7 | 25 |
| 7 | 1140 | 3.1 | 8.3 | 21 |
| 18 | 1720 | 4.6 | 6 | 22 |
| 12 | 1870 | 2.9 | 2.3 | 11 |
| 3ABa | 1900 | 1.6 | 2.5 | 8.1 |
| 3ABb | 2000 | 2.8 | 1.3 | 8.0 |
| E45a | 2050 | 3.3 | 6.3 | 19 |
| E45b | 2200 | 3.4 | 5.2 | 18 |
| 19 | 2560 | 4.0 | 5.0 | 19 |
| pf5 | 3070 | 1.5 | 4.3 | 11 |
| L/pfa | 3200 | 0.6 | 4.5 | 6.7 |
| L/pfb | 3280 | 0.4 | 5.0 | 5.9 |
| pf2 | 3400 | 0.9 | 6.5 | 10 |
| pf2a | 3300 | 1.4 | 2.5 | 7.7 |
| pf2b | 3210 | 1.4 | 3.5 | 9.0 |
| pf2c | 3100 | 1.8 | 3.3 | 10 |
| LCB | 4360 | 1.4 | 2.5 | 7.7 |
| LCBa | 4350 | 1.3 | 4.2 | 9.4 |
| LCBb | 4300 | 1.4 | 3.0 | 8.4 |
| LCBc | 4200 | 0.5 | 4.0 | 6.0 |

Several of the flow units listed in figs. 1.5 and 1.6 contain multiple curved reaches. In this table, velocities calculated at these additional reaches are indicated by "a", "b", or "c" following the station number.

## APPENDIX B

### FORTRAN Code for Model 1.

```
      PROGRAM M1
C
C       MODEL 1
C
C       THIS PROGRAM COMPUTES THE INCREMENTAL SLOPES
C       ON A TOPOGRAPHIC PROFILE, AND THEN COMPUTES
C       THE INCREMENTAL ACCELERATIONS AND VELOCITIES
C       BASED ON COEFFICIENT OF TOTAL FRICTION.
C
C
      INTEGER ELEV2
      INTEGER RUN2
      CHARACTER*8 IN1,IN2
      PRINT*,'ENTER INPUT FILENAME: ("_8 characters")'
      READ(*,01)IN1
      PRINT*,'ENTER OUTPUT FILENAME: ("_8 characters")'
      READ(*,01)IN2
 01   FORMAT(1X,A8)
C
      OPEN(UNIT=19,FILE=IN1,STATUS='OLD')
      OPEN(UNIT=21,FILE=IN2,STATUS ='NEW')
C
      PRINT*,'ENTER ZERO TO QUIT:'
      READ*,ANS
       IF(ANS.EQ.0)THEN
       GO TO 71
       ENDIF
  02  PRINT*,'PLEASE ENTER FOUNTAIN HEIGHT:'
      READ*, COLM
      PRINT*,'PLEASE ENTER FRICTIONAL COEFFICIENT: '
      READ*,FRIC
      PRINT*,'PLEASE ENTER INITIAL VELOCITY:'
      READ*,VELI
      ELEV1=0
      RUN1=0
      K=0
      TIMET=0
      REWIND(UNIT=19)
      REWIND(UNIT=21)
C
```

```
C          Activity loop.
C
 10    READ(19,*,END=70)ELEV2,RUN2
       FALL=(ELEV1-ELEV2)
            IF(FALL.EQ.(-ELEV2))THEN
            FALL=0
            DIST=0
            SLOPED=0
            ACCEL=1
            VVELT=VELI
            VVELO=VELI
            TIME=0
            GO TO 40
            ENDIF
       DIST=(RUN2-RUN1)
       SLOPE=(FALL/DIST)
       SLOPER=ATAN(SLOPE)
       SLOPED=(57.296*SLOPER)
       ACCEL=(9.80*((SIN(SLOPER))-(FRIC*(COS(SLOPER)))))
       HYPN=(FALL/(SIN(SLOPER)))
       VVELTSQ=((VVELO**2)+((2*ACCEL)*HYPN))
          IF(VVELTSQ.LT.0)THEN
          PRINT*,
     +'                                                    '
          PRINT*,
     +'           FRIC. COEFF. TOO HIGH......TRY AGAIN  '
          PRINT*,
     +'                                                    '
          GO TO 02
          ENDIF
       VVELT=(SQRT(VVELTSQ))
       IF(ACCEL.EQ.0)THEN
         TIME=(HYPN/VVELT)
         GO TO 40
         ENDIF
       TIME=((VVELT-VVELO)/(ACCEL))
 40    WRITE(21,*)ELEV2,RUN2,ACCEL,VVELT,SLOPER
       PRINT*,ELEV2,RUN2,ACCEL,VVELT,SLOPER
       ELEV1=ELEV2
       RUN1=RUN2
       VVELO=VVELT
         IF(K.EQ.0)THEN
         ELEV0=(ELEV2+COLM)
         RUN0=RUN2
         ENDIF
       K=(K+1)
       TIMET=(TIMET+TIME)
       GO TO 10
C
```

```
C          Output section.
C
 70    FARB=(ELEV0-ELEV2)/(RUN2-RUN0)
       PRINT*,' '
       PRINT*,'FAHRBOESCHUNG:'
       PRINT*,FARB
 71    PRINT*,'  '
       PRINT*,'FRIC. COEFF. USED:'
       PRINT*,FRIC
       PRINT*,' '
       PRINT*,'ELAPSED TIME (SEC):'
       PRINT*,TIMET
       PRINT*, '  '
       PRINT*,'NUMBER OF DATA LINES:', K
       PRINT*,' '
       PRINT*,'ENTER ZERO TO QUIT:'
       READ*, AN2
        IF(AN2.EQ.0)THEN
        GO TO 80
        ENDIF
       GO TO 02
  80   WRITE(21,*)FRIC,FARB,TIMET,COLM,K
       STOP
       END
```

## APPENDIX C

### Dimensional Analysis of $R'$.

A functional relationship is known to exist between the physical quantities yield strength $K$, Bingham viscosity $\eta_b$, flow velocity $v$, and "kinetic energy flux" $R'$. The Buckingham $\Pi$ theorem proves that in a problem involving $n$ physical quantities in which there are $m$ fundamental dimensions, $(n - m)$ independent dimensionless $\Pi$ parameters can be formed (Streeter and Wylie 1985). For the flow resistance problem, $(4 - 3) = 1$ $\Pi$ parameter will result.

The procedure for determining $\Pi$ begins with selecting $m$ of the quantities to be repeating variables. The quantities selected must collectively contain the three fundamental dimensions $M, L$, and $T$, and none of the repeating variables can be derivable from the other repeating variables. $K$, $\eta_b$, and $v$ are selected as the repeating variables, so the $\Pi$ parameter takes the form

$$\Pi = K^x \eta_b{}^y v^z R'. \tag{C.1}$$

In terms of the fundamental dimensions,

$$\Pi = \left[\frac{M}{LT^2}\right]^x \left[\frac{M}{LT}\right]^y \left[\frac{L}{T}\right]^z \left[\frac{1}{T}\right] = M^0 L^0 T^0. \tag{C.2}$$

The exponents of each dimension must be the same on both sides of the equation in order for $\Pi$ to be dimensionless. Setting the exponents of $M$, $L$, and $T$ equal to zero respectively results in three equations (one each for $M$, $L$, and $T$) in three unknowns ($x, y$, and $z$). The

equation for $M$ is

$$M : 1x + 1y + 0z + 0 = 0. \tag{C.3}$$

$M$ is to the $+1$ power in $K$ and $\eta_b$, and not present in $v$ or $R'$. Similarly for $L$ and $T$,

$$L : -1x - 1y + 1z + 0 = 0, \tag{C.4}$$

$$T : -2x - 1y - 1z - 1 = 0. \tag{C.5}$$

Equations (C.3) through (C.5) are then solved algebraically giving the values of the exponents

$$x = -1$$

$$y = 1$$

$$z = 0.$$

Substituting into equation (C.1) gives the final result of the dimensional analysis

$$\Pi = \frac{\eta_b R' v^0}{K} = \frac{\eta_b R'}{K}. \tag{C.6}$$

Checking the units of this arrangement proves that (C.6) is indeed dimensionless:

$$\frac{\left(\frac{\mathrm{kg}}{\mathrm{m\,s}}\right)\left(\frac{1}{\mathrm{s}}\right)}{\left(\frac{\mathrm{kg}}{\mathrm{m\,s^2}}\right)}.$$

## APPENDIX D

### FORTRAN Code for Model 2.

```
      PROGRAM M2
C
C       MODEL 2.
C
C       THIS PROGRAM COMPUTES THE INCREMENTAL SLOPES ON A
C       TOPOGRAPHIC PROFILE, AND THEN COMPUTES
C       THE INCREMENTAL ACCELERATIONS AND VELOCITIES.
C       VISCOUS RESISTANCE ONLY, VIA KINETIC ENERGY
C       FLUX TERM.
C
      CHARACTER* 8 IN1,IN2,PAR,PLTR
      REAL INCMASS
      PRINT*,'********* PROGRAM M2.FOR ************'
      PRINT*,' '
      PRINT*,
     +'ENTER PLOTTING OUTPUT FILENAME: ("_8 characters")'
      READ(*,08)PLTR
      OPEN(UNIT=16,FILE=PLTR,STATUS='NEW')
 01   PRINT*,
     +'ENTER 1 FOR PAR. FILEREAD OR 2 FOR PAR. INPUT:'
      READ*,AN0
       IF(AN0.EQ.1)THEN
       PRINT*,'ENTER PARAMETER FILENAME: ("_8 characters")'
       READ(*,08)PAR
       OPEN(UNIT=17,FILE=PAR,STATUS='OLD')
       READ(17,09,END=04)IN1,IN2,RHO,ETA,H0,XK,XL,VELO,C
       CO=C
 04    OPEN(UNIT=19,FILE=IN1,STATUS='OLD')
       OPEN(UNIT=21,FILE=IN2,STATUS ='NEW')
       GO TO 10
       ENDIF
C
       IF(AN0.EQ.2)THEN
 05    PRINT*,'ENTER INPUT FILENAME: ("_8 characters")'
       READ(*,08)IN1
       PRINT*,'ENTER OUTPUT FILENAME: ("_8 characters")'
       READ(*,08)IN2
       PRINT*,
     + 'ENTER PARAMETER-SAVE FILENAME: ("_8 characters")'
       READ(*,08)PAR
```

```
      OPEN(UNIT=19,FILE=IN1,STATUS='OLD')
      OPEN(UNIT=21,FILE=IN2,STATUS ='NEW')
      OPEN(UNIT=17,FILE=PAR,STATUS='NEW')
C
 06   REWIND(UNIT=17)
      PRINT*,'ENTER RHO:'
      READ*,RHO
      PRINT*,'ENTER ETA:'
      READ*,ETA
      PRINT*,'ENTER H0:'
      READ*,H0
      PRINT*,'ENTER K:'
      READ*, XK
      PRINT*,'ENTER XL:'
      READ*,XL
      PRINT*,'ENTER VELO:'
      READ*,VELO
      PRINT*,'ENTER C:'
      READ*,C
      C0=C
      FARB=H0/XL
      WRITE(17,09)IN1,IN2,RHO,ETA,H0,XK,XL,VELO,C
      GO TO 10
      ENDIF
      GO TO 01
 08    FORMAT(1X,A8)
 09    FORMAT(1X,A8,1X,A8,1X,F5.0,1X,F5.0,1X,F5.0,1X,
     + F6.0,1X,F6.0,1X,F5.1,1X,F6.2)
C
 10   C0=C
C
C
```

```
C       Activity Loop.
C
C
 100  REWIND (UNIT=19)
      REWIND (UNIT=21)
      REWIND (UNIT=16)
      TIMET=0
      ELEV1=0
      K=0
 110  READ(19,*,END=700)ELEV2,RUN2
      IF(ELEV1.EQ.0)THEN
          RUNO=RUN2
          SLOPER=0
          SLOPED=0
          ACCEL=0
          VVELT=VELO
          INCMASS=OMASS
          TIME=0
          GO TO 400
          ENDIF
      FALL=(ELEV1-ELEV2)
      DIST=(RUN2-RUN1)
      SLOPE=(FALL/DIST)
      SLOPER=ATAN(SLOPE)
      SLOPED=(57.296*SLOPER)
C
```

```
C       Model controlling statements:
C
 200  R=((C*ETA)/XK)
      ACCEL=(9.80*(SIN(SLOPER)))-(R*VVELT)
C
      HYPN=(FALL/(SIN(SLOPER)))
      VVELTSQ=((VELO**2)+((2*ACCEL)*HYPN))
         IF(VVELTSQ.LT.0)THEN
 210     PRINT*,' '
         PRINT*,'   FRICTIONAL FORCES TOO HIGH.....   '
 220     PRINT*,' '
C
         PRINT*,'TO END THIS RUN, TYPE 0 (ZERO).'
         PRINT*,'TYPE  1 TO RE-ENTER PARAMETERS:'
         PRINT*,'TYPE  2 TO RE-ENTER C ONLY:'
         PRINT*,
     +   'TYPE ANY TO DO ITERATIVE FIT, SAVING C RESIDS:'
         READ*,T0
          IF(T0.EQ.0)THEN
          GO TO 700
          ENDIF
          IF(T0.EQ.1)THEN
          GO TO 06
          ENDIF
          IF(T0.EQ.2)THEN
          PRINT*,'ENTER NEW C NOW:'
          READ*,C
          C0=C
          REWIND(UNIT=17)
          WRITE(17,09)IN1,IN2,RHO,ETA,H0,XK,XL,VELO,C
          GO TO 100
         ENDIF
C
  230    C=(C-0.01)
         PRINT*,C
         R=((C*ETA)/XK)
         ACCEL=(9.80*(SIN(SLOPER)))-(R*VVELT)
         HYPN=(FALL/(SIN(SLOPER)))
         VVELTSQ=((VELO**2)+((2*ACCEL)*HYPN))
           IF(VVELTSQ.LT.VCON)THEN
           GO TO 230
           ENDIF
C
        ENDIF
      VVELT=(SQRT(VVELTSQ))
        IF(ACCEL.EQ.0)THEN
        TIME=(HYPN/VVELT)
        GO TO 400
        ENDIF
      TIME=((VVELT-VELO)/(ACCEL))
C
```

```
C         Output section.
C
 400  WRITE(21,*)ELEV2,RUN2,ACCEL,VVELT,C,C0
      WRITE(16,*)ELEV2,RUN2,ACCEL,VVELT,TIME
      PRINT*,RUN2,ACCEL,SLOPED,VVELT,C
      VCON=(0.2*VVELTSQ)
      C=C0
      ELEV1=ELEV2
      RUN1=RUN2
      VELO=VVELT
      TIMET=(TIMET+TIME)
      K=(K+1)
      GO TO 110
C
C
C
 700  PRINT*,'*************STOP JOB*************'
      PRINT*,'FAHRBOESCHUNG:',FARB
      PRINT*,'ETA:          ',ETA
      PRINT*,'K:            ',XK
 800  PRINT*,'ELAPSED TIME; ',TIMET
      PRINT*,'NUMBER OF DATA LINES:',K
      WRITE(21,*)RHO,ETA,H0,XK,XL,FARB,VELO,TIMET,K,C0
      STOP
      END
```

## APPENDIX E

### FORTRAN Code for Model 3.

```
          PROGRAM M3
C
C       MODEL 3
C
C       THIS PROGRAM COMPUTES THE INCREMENTAL SLOPES ON A
C       TOPOGRAPHIC PROFILE, AND THEN COMPUTES
C       THE KINETIC FRICTION COEFFICIENT
C       FROM THE VISCOSITY RELATIONSHIP OF REINER/VOIGHT
C       AND THE INCREMENTAL ACCELERATIONS AND VELOCITIES
C       USING THIS VALUE OF MU.
C
C
      CHARACTER* 8 IN1,IN2,PAR,PLTR
      REAL K
      REAL MUK
      PRINT*,'********* PROGRAM M3.FOR *************'
      PRINT*,' '
      PRINT*,
     +'ENTER PLOTTING OUTPUT FILENAME: ("_8 characters")'
      READ(*,08)PLTR
      OPEN(UNIT=16,FILE=PLTR,STATUS='NEW')
 01   PRINT*,
     +'ENTER 1 FOR PAR. FILE READ, OR 2 FOR PAR.INPUT:'
      READ*,A
        IF(A.EQ.1)THEN
        GO TO 03
        ENDIF
        IF(A.EQ.2)THEN
        GO TO 05
        ENDIF
      GO TO 01
 03   PRINT*,'ENTER PARAMETER FILENAME:  ("_8 characters")'
      READ(*,08)PAR
      OPEN(UNIT=22,FILE=PAR,STATUS='OLD')
      READ(22,09,END=04)IN1,IN2,VELOO,ACCELO,RHO,ETA,K,TK,
     +ELEV0,RUN0
 04   OPEN(UNIT=19,FILE=IN1,STATUS='OLD')
      OPEN(UNIT=21,FILE=IN2,STATUS ='NEW')
      GO TO 115
C
```

```
 05    PRINT*,'ENTER INPUT FILENAME: ("_8 characters")'
       READ(*,08)IN1
       PRINT*,'ENTER OUTPUT FILENAME: ("_8 characters")'
       READ(*,08)IN2
       PRINT*,
      +'ENTER PARAMETER-SAVE FILENAME: ("_8 characters")'
       READ(*,08)PAR
 08    FORMAT(1X,A8)
 09    FORMAT(1X,A8,1X,A8,1X,F3.0,1X,F3.0,1X,F5.0,1X,
      +F5.0,1X,F6.0,1X,F4.1,1X,F5.0,1X,F5.0)
C
C
       OPEN(UNIT=19,FILE=IN1,STATUS='OLD')
       OPEN(UNIT=21,FILE=IN2,STATUS ='NEW')
C
C
C
       OPEN(UNIT=23,FILE=PAR,STATUS='NEW')
C
 110   REWIND(UNIT=19)
       REWIND(UNIT=21)
       PRINT*,'Please enter VELO:'
       READ*,VELOO
       PRINT*, 'Please enter ACCELO:'
       READ*,ACCELO
       PRINT*,'Please enter RHO:'
       READ*,RHO
       PRINT*,'Please enter ETA:'
       READ*,ETA
       PRINT*, 'Please enter K:'
       READ*, K
       PRINT*, 'Please enter TK:'
       READ*, TK
       PRINT*,'Please enter ELEV0:'
       READ*,ELEV0
       PRINT*,'Please enter RUN0:'
       READ*,RUN0
       WRITE(23,09)IN1,IN2,VELOO,ACCELO,RHO,ETA,K,TK,
      +ELEV0,RUN0
C
C
```

```
C       Activity Loop.
C
C
 115  TIMET=0
      ELEV1=ELEV0
      RUN1=RUN0
      GAMMA=(9.806*RHO)
      KOUNT=0
 120  READ(19,*,END=700)ELEV2,RUN2
      KOUNT=KOUNT+1
      IF(ELEV1.EQ.ELEV2)THEN
          SLOPER=0
          SLOPED=0
          ACCEL=ACCELO
          VELO=VELOO
          VVELT=VELO
          TIME=0
          VVSQ0=0
          GO TO 400
          ENDIF
      FALL=(ELEV1-ELEV2)
      DIST=(RUN2-RUN1)
      SLOPE=(FALL/DIST)
      SLOPER=ATAN(SLOPE)
      SLOPED=(57.296*SLOPER)
C
```

```
C       Model controlling statements:
C
C      DF=7.41-(0.00409*RUN2)+(0.000000777*(RUN2**2))
       IF(SLOPED.GT.40)THEN
       DF=3.0
       GO TO 129
       ENDIF
       IF(SLOPED.GT.30)THEN
       DF=3.5
       GO TO 129
       ENDIF
       IF(SLOPED.GT.20)THEN
       DF=3.8
       GO TO 129
       ENDIF
       IF (SLOPED.GT.10)THEN
       DF=3.8
       GO TO 129
       ENDIF
       IF (SLOPED.LT.10)THEN
       DF=3.8
       ENDIF
C
        IF(TK.LT.1)THEN
         TK=1
         ENDIF
       DF=TK+1
 129   DF1=DF
        IF(DF.LT.TK)THEN
        DF=TK+0.2
        ENDIF
 130   ACCEL1=ACCELO
C
C       * * * *
C       COMMENTS ON VARIABLE VALUES APPEAR
C       AT END OF THIS LISTING
C       * * * *
C
C
      MUK=(1/COS(SLOPER))*(((2/(GAMMA*(DF**2-TK**2)))*
     +((ETA*VELO)+(K*(DF-TK))))-(ACCEL1/9.806))
      IF(MUK.LT.0)THEN
      MUK=0
      ENDIF
```

```
C
      PRINT*,'------------test results-------------'
      PRINT*,'ACCEL1:',ACCEL1,'  VELO;',VELO,'RUN2:',RUN2,
     +'  SLOPED:',SLOPED,'  MUK:',MUK,'  DF:',DF,
     +'  DFC:',DF1
      ACCEL=(9.80*((SIN(SLOPER))-(MUK*(COS(SLOPER)))))
      HYPN=(FALL/(SIN(SLOPER)))
      VVELTSQ=((VELO**2)+((2*ACCEL)*HYPN))
      PRINT*,'Accel:' ,ACCEL,'Vveltsq:',VVELTSQ,' K:',K,
     +' ETA:',ETA
          IF(VVELTSQ.GT.0)THEN
          VVELT=(SQRT(VVELTSQ))
          PRINT*,'Vvelt:',VVELT
          ENDIF
          PRINT*,'---------------------------------------'
 210      PRINT*,' '
 220      PRINT*,'  '
C
C           Debug choices
C
          PRINT*,'TO END THIS RUN, TYPE 0 (ZERO).'
          PRINT*,'TO CHANGE FLOW DEPTH HERE TYPE 1:'
          PRINT*,'FOR AUTOMATIC DEPTH CALC TYPE 2:'
          PRINT*,'TO CONTINUE, TYPE 3:'
          PRINT*,'TYPE ANY OTHER NUMBER TO CHANGE PARAMETERS
     +AND REWIND JOB:'
          READ*,T0
           IF(T0.EQ.0)THEN
           GO TO 700
           ENDIF
           IF(T0.EQ.1)THEN
           PRINT*,'ENTER NEW FLOW DEPTH FOR THIS POSITION:'
           READ*,DF
           GO TO 130
           ENDIF
           IF(T0.EQ.2)THEN
           GO TO 380
           ENDIF
           IF(T0.EQ.3)THEN
           GO TO 390
           ENDIF
          PRINT*,'ENTER A NEW PARAMETER SET NOW.'
          GO TO 110
C
```

```
C       Automatic depth loop.
C
 380  ACCEL1=ACCELO
 382  MUK=(1/COS(SLOPER))*(((2/(GAMMA*(DF**2-TK**2)))*
     X((ETA*VELO)+(K*(DF-TK))))-(ACCEL1/9.806))
      ACCEL=(9.80*((SIN(SLOPER))-(MUK*(COS(SLOPER)))))
      HYPN=(FALL/(SIN(SLOPER)))
      VVELTSQ=((VELO**2)+((2*ACCEL)*HYPN))
      VCON=(0.5*VVSQ0)
C
         IF(VVELTSQ.LT.VCON)THEN
         DF=DF+0.01
         PRINT*,DF
         GO TO 382
         ENDIF
      VVELT=(SQRT(VVELTSQ))
C
C
C
 390  PRINT*,
     +'************************************************'
      PRINT*,'RESULTS:'
      PRINT*,'   MUK:',MUK,'   DF:',DF,'   DFcalc:',DF1
      PRINT*,'   ZZ:',ZZ,'  VEL T:',VVELT,'  RUN:',RUN2
      PRINT*,'   SLOPED:',SLOPED,'  ACCEL:',ACCEL,' K:',K,
     +' ETA:',ETA
      PRINT*,
     +'************************************************ '
      VVSQ0=VVELTSQ
        IF(ACCEL.EQ.0)THEN
        TIME=(HYPN/VVELT)
        GO TO 400
        ENDIF
      TIME=((VVELT-VELO)/(ACCEL))
C
```

```
C         Output section.
C
 400   WRITE(21,900)ELEV2,RUN2,SLOPER,SLOPED,DF,MUK,ACCEL,
      +VVELT,TIME,DF1
       WRITE(16,*)ELEV2,RUN2,ACCEL,VVELT,DF
       PRINT*,' '
       ELEV1=ELEV2
       RUN1=RUN2
       VELO=VVELT
       ACCELO=ACCEL
       TIMET=(TIMET+TIME)
       GO TO 120
C
 700   PRINT*,' *************STOPJOB*******************'
       WRITE(21,900)ELEV2,RUN2,SLOPER,SLOPED,DF,MUK,ACCEL,
      +VVELT,TIME,DF1
       PRINT *,ELEV2,RUN2,SLOPER,SLOPED,DF,MUK,ACCEL,VVELT,
      +TIME
       WRITE(21,*)ACCELO,VELOO,TK,K,ETA,RHO,TIMET,KOUNT
       PRINT*,'    '
       PRINT*,'ACCELO:        ',ACCELO
       PRINT*,'VELO:          ',VELOO
       PRINT*,'TK:            ',TK
       PRINT*,'K:             ',K
       PRINT*,'RHO:           ',RHO
       PRINT*,'ETA:           ',ETA
 800   PRINT*,'ELAPSED TIME; ',TIMET
 900   FORMAT(1X,2(1X,F6.0),1X,F5.4,1X,F5.2,2X,F5.2,1X,
      +F7.4,1X,F7.3,1X,F7.3,1X,F5.1,1X,F5.2)
       STOP
       END
C
C       TK=2.229437-(0.3035799E-3*RUN2)
C       r-squared=0.37
C
C       K=(12123.3+(.00076492*(RUN2**2))-(5.72294*(RUN2)))
C       ETA=(705.618+(.66808E-4*(RUN2**2))-(.408932*(RUN2)))
C       K=(9.2143021E+3-(2.2245439*RUN2))
C       r-squared=0.76
C       IF(K.LT.1200)THEN
C       K=1200
C       ENDIF
C       ETA=(4.51374134E+2-(0.10317226*RUN2))
C       r-squared=0.50
C       IF(ETA.LT.79)THEN
C       ETA=79
C       ENDIF
```